

ELECTRON CHANNELING PATTERNS FROM
ELASTICALLY AND PLASTICALLY DEFORMED CRYSTALS

BY

MICHAEL CHARLES MADDEN

A DISSERTATION PRESENTED TO THE GRADUATE COUNCIL
OF THE UNIVERSITY OF FLORIDA IN
PARTIAL FULFILLMENT OF THE REQUIREMENTS
FOR THE DEGREE OF DOCTOR OF PHILOSOPHY

UNIVERSITY OF FLORIDA

1982

ACKNOWLEDGEMENTS

First and foremost, I would like to thank my parents, who instilled the values and advantages of higher education and provided the greatest single motivation for my pursuit of a graduate degree.

Many thanks to my committee chairman, Dr. John Hren, who endured many late night meetings and tolerated the many difficulties finishing a degree with a student 1800 miles from the University.

Thanks to Bob Owen, who kept the computer and SEM going, wrote the computer programs, and designed the electronics for the interface between the computer and the SEM that allowed the recording of intensity profiles.

Thanks to E. J. Jenkins and Wayne Acree, whose insight in preparing specimens is acknowledged and to Dick Tomlinson, for providing rapid fabrication of small parts on short notice.

Thanks also to Sandia Laboratories who not only hired me before the completion of my degree, thus averting a major financial crisis, but also made their facilities available for the completion of my graduate work.

All topographic micrographs are actually at 1.33 times the magnification indicated by the bright letters along their lower edge. The micron bars in these micrographs should also be multiplied by 1.33. This is a result of the shorter working distance used in channeling operation.

Micron bars appearing on electron channeling patterns have absolutely no significance. They are an electronic artifact from the normal use of the scanning electron microscope.

TABLE OF CONTENTS

ACKNOWLEDGEMENTS.....		ii
ABSTRACT.....		vi
CHAPTER		
1	INTRODUCTION.....	1
	1.1 Development of Electron Channeling in the SEM.....	1
	1.2 Effects of Dislocations on Electron Channeling Patterns.....	14
	1.3 Scope of the Present Research.....	21
2	OPTICS OF ELECTRON CHANNELING.....	24
	2.1 Basic Optics of Magnetic Lenses.....	24
	2.2 Conventional Operation of the Scanning Electron Microscope.....	26
	2.3 Optics of Electron Channeling.....	34
	2.3.1 Introduction.....	34
	2.3.2 The Three Lens Scanning Electron Microscope.....	45
	2.3.3 The Image Mode.....	47
	2.3.4 The Selected Area Channeling Pattern (SACP) Mode.....	47
	2.3.5 The Selected Area Image (SAI) Mode.....	47
	2.3.6 Large Area Channeling Patterns.....	53
	2.4 Procedures for Machine Adjustment and Alignment.....	55
	2.4.1 Electron Gun and Condenser Lens Alignment.....	55
	2.4.2 The Image and SAI Modes.....	59
	2.4.3 Correction of Spherical Abberation.....	59
	2.4.4 The SACP Mode.....	64
	2.5 Additional Electronics for Channeling.....	64
3	FINE STRUCTURES NEAR THE CENTER OF LOW INDEX POLES IN ELECTRON CHANNELING PATTERNS.....	70
	3.1 Origin of Fine Structure.....	70
	3.2 Application of the Reciprocal Lattice-Ewald Sphere Construction to the Fine Structure in Electron Channeling Patterns.....	77

CHAPTER	
3.3	Changes to the Fine Structure During Elastic Strain....99
3.4	Other Lines From the First Order Laue Zone.....111
3.5	Summary.....120
4	EXPERIMENTAL METHODS.....121
4.1	Introduction.....121
4.2	Preparation of Samples for Elastic Straining.....123
4.3	Plastically Strained Specimen Preparation.....124
5	RESULTS AND DISCUSSION.....139
5.1	Plastically Strained Samples.....139
5.1.1	Electron Channeling Patterns.....139
5.1.2	Transmission Electron Microscope Studies.....152
5.1.3	Discussion.....188
5.2	Elastically Strained Samples.....198
5.3	Summary.....203
6	CONCLUSIONS AND RECOMMENDATIONS FOR FURTHER STUDY.....204
6.1	Conclusions.....204
6.2	Recommendations for Further Study.....208
	REFERENCES.....210
	BIOGRAPHICAL SKETCH.....214

Abstract of Dissertation Presented to the Graduate Council
of the University of Florida in Partial Fulfillment of the
Requirements for the Degree of Doctor of Philosophy

ELECTRON CHANNELING PATTERNS FROM
ELASTICALLY AND PLASTICALLY DEFORMED CRYSTALS

by

Michael Charles Madden

May, 1982

Chairman: Dr. J. J. Hren

Major Department: Materials Science and Engineering

Electron channeling patterns are obtained in a scanning electron microscope by photographically recording backscattered electron intensity while rocking an electron beam around a single point on a specimen surface. Variations in intensity occur with angle of incidence relative to atomic planes in crystalline materials. A typical channeling pattern consists of a combination of high contrast pairs of parallel lines resulting from low order planes and finer, lower contrast lines that occur singly.

Plastic strain is characterized by dislocations, and the multidirectional lattice strains caused by dislocations cause contrast loss in the channeling pattern. Silicon (111) single crystals were plastically deformed by bending and chemically thinned. Dislocations introduced by the bending were characterized by transmission electron microscopy at 200 kV. Electron channeling patterns were obtained at 15 kV, and intensity profiles across each of the three {220} planes were recorded. The changes in the channeling

patterns and intensity profiles are related to the concentration and type of dislocations present as determined by transmission electron microscopy.

The fine lines that occur singly in the channeling patterns from (111) silicon have three-fold symmetry (as opposed to the six-fold symmetry of the parallel line pairs). These lines have higher Miller indices and originate in the first order Laue zone in reciprocal space. The parallel pairs of lines forming most of the pattern come from the zero order Laue zone. The first order zone lines exist throughout the pattern but are most visible within 1° of the (111) pole.

The position of these lines is sensitive to elastic strain. A method for calculating the shifts in any selected line is derived along with experimental data from strained (111) silicon.

The origin and geometry of the fine lines are discussed using the Ewald sphere-reciprocal lattice construction and a method of determining the Miller indices of an unknown line arising from the first order zone presented.

CHAPTER 1 INTRODUCTION

1.1 Development of Electron Channeling on the SEM

Electron channeling patterns result from the variation in electron backscattering coefficient (η) with angle of incidence in a crystalline solid. They are obtained by systematically varying the angle at which an electron beam strikes a sample along two orthogonal axes and photographically recording the intensity of the backscattered electrons produced. Electron channeling patterns are usually obtained in a scanning electron microscope (SEM) and they are significant because they allow crystallographic information to be obtained on bulk specimens.

Electron channeling patterns were first obtained by Coates (1967) while examining single crystal semiconductors in an SEM at low magnifications. At low magnifications the area scanned by the electron beam is relatively large, and the beam goes through substantial angular changes during the course of a scan. The channeling pattern appears as a faint series of parallel lines superimposed on the topographic image. Figure 1.1 is a (100) single crystal of silicon obtained under conditions similar to those used by Coates. The two intersecting pairs of lines are {200} planes. The point of intersection is the (100) pole. Coates also observed that the lines did not shift when the sample translated, but did move when it was tilted, which is consistent with a crystallographic origin for the pattern, and that the width of the bands was proportional to the De Broglie wavelength of the incident electron beam.

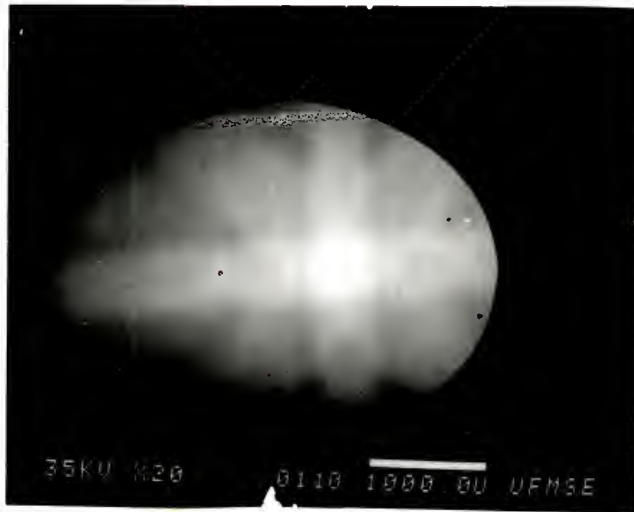


Figure 1.1 Topographic SEM of (100) silicon at 20X. Channeling contrast is visible as broad bands.

The origin and geometry of electron channeling patterns can be understood at several levels of sophistication. Perhaps the most straightforward is that of Newberry and Yakowitz (1975) illustrated in Figure 1.2. As the main beam strikes the lattice at the angle illustrated in 1.2(a), the beam does not penetrate deeply into the lattice, and relatively large numbers of backscattered electrons are produced. In 1.2(b) the beam is more nearly aligned with the crystallographic planes, the beam penetrates further into the lattice, and smaller numbers of backscattered electrons are produced.

A more quantitative explanation is provided by the Bloch wave model (Booker et al., 1967) based on earlier work on x-ray production by Hirsch et al. (1962). As shown in Figure 1.3, an electron beam striking a crystal at angle θ can be considered to be a series of Bloch waves. Near the Bragg angle, θ_B , only two waves are excited, one with maxima between the atomic positions (Type I) and the other with maxima at the atomic positions (Type II). At the exact Bragg condition, both waves are of equal intensity. For $\theta < \theta_B$, the Type II wave is of greater intensity, and since they have maxima at the atomic positions, they are strongly scattered and produce a large number of backscattered electrons. For $\theta > \theta_B$, Type I waves predominate and produce relatively few backscattered electrons. The transition from Type I to Type II waves occurs over a small range in θ , and this results in the bright/dark transition around θ_B that defines the lines seen in channeling patterns. This transition occurs at $-\theta_B$ as well, and it is this pair of lines that forms the bands of electron channeling patterns. It is this "anomalous transmission" or channeling, that occurs near θ_B and gives channeling patterns their name.

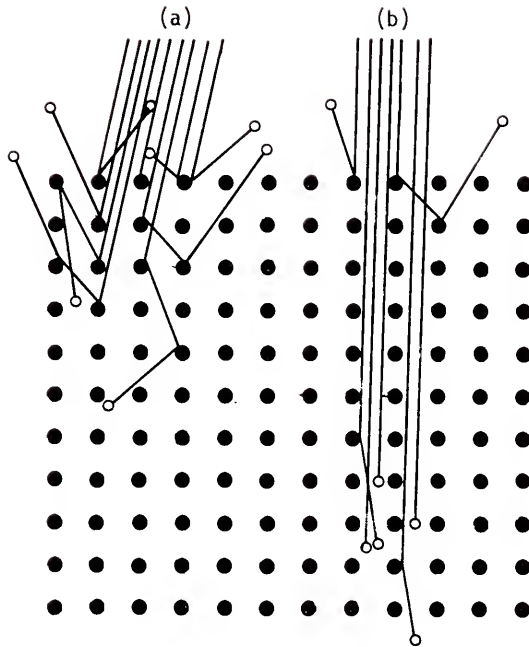


Figure 1.2 Simple model of channeling contrast. Interaction at (a) produces more backscattered electrons than (b) (Newberry and Yakowitz, 1975).

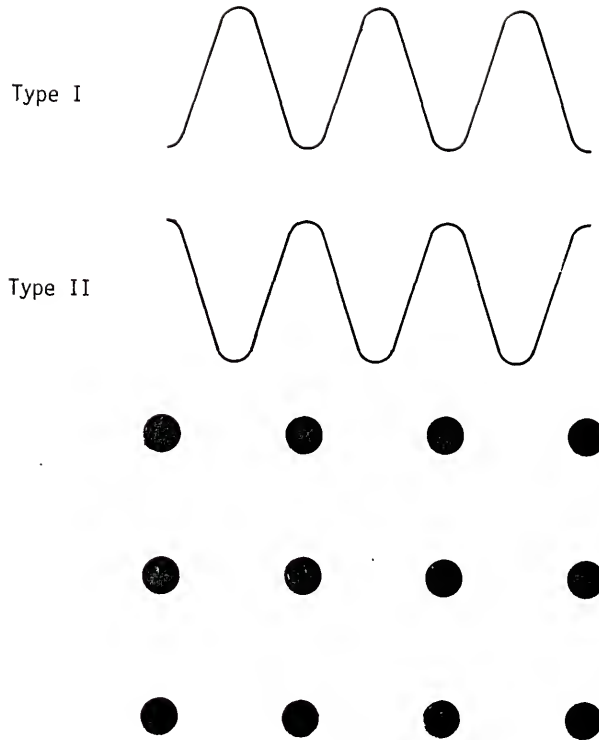


Figure 1.3 Bloch wave model of electron channeling. Type I wave has maxima between atomic positions, Type II at atomic positions (Newberry and Yakowitz, 1975).

The resolution of an SEM operated in the normal (topographic) mode is dependent on a small beam size at the specimen surface while maintaining sufficient beam current to operate the detector. Since the channeling pattern uses the angle of incidence as the variable parameter, one might expect pattern resolution to improve by minimizing beam divergence, and this is the case (Coates, 1968). This can be accomplished by changing the settings on the lenses in the optical column. In particular cases, this may also involve turning off the objective lens (Schulson and Van Essen, 1969), or adding a lens between the condenser and objective lenses (JEOL, 1971). Beam current must still be maintained at a sufficient level to operate the backscattered detector, and thus experimental beam conditions are a compromise.

Examining specimens at low magnifications results in a large scanned area and is limited to very large crystals. Methods for reducing the area from which the channeling pattern is obtained are discussed by Schulson (1969). There are basically three methods: keeping the beam stationary and tilting the specimen; tilting the beam around a stationary point on the specimen; or combinations of the two, as shown in Figure 1.4.

A stationary beam and tilting specimen requires a carefully constructed specimen stage capable of being tilted about two orthogonal axes in coordination with the cathode ray tube (CRT) raster (Coates, 1969). Such a stage is difficult to construct but a large angular range can be obtained and no distortions from electron optics are introduced. Generation of a complete pattern can require relatively long times. Although this method is not commonly used, it was used by Brunner et al. (1978) to generate large ($150^{\circ} \times 110^{\circ}$) channeling patterns for epitaxial films.

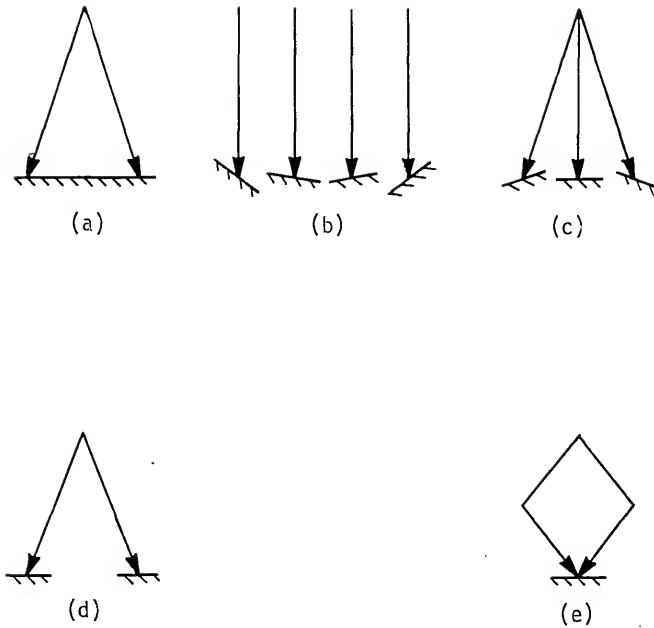


Figure 1.4 Methods of eliminating beam travel across surface during channeling operation. (a) normal operation, (b) specimen tilting under stationary beam, (c) specimen tilting with conventional beam scanning, (d) specimen translation and (e) electron beam rocking (Schulson, 1969).

By far, the most common method used to generate channeling patterns is electronically tilting the beam around a point on the specimen surface. This can be achieved in two ways: reducing the strength of the lower scan coil or using the upper scan coil and the objective lens (Van Essen et al., 1970). Using these methods channeling patterns can be obtained from areas as small as $10\ \mu\text{m}$ in diameter. Even $1\ \mu\text{m}$ can be obtained using a substantially altered scan system (Joy and Newberry, 1972). Patterns obtained by tilting the beam around a point are called selected area channeling patterns (SACP).

Figure 1.5 shows a SACP from (100) single crystal of silicon. This compares with the ECP shown in Figure 1.1. The topographic contrast has been eliminated, since the beam is no longer dimensionally scanning the surface. Regular topographic images can still be obtained by changing currents in the objective lens and scan coils.

Details of the electron optics involved in minimizing beam divergence and obtaining beam scanning for SACPs are described in more detail in Chapter 2.

The geometry of electron channeling patterns is similar to Kikuchi patterns, although their origin is quite different. In Figure 1.5, the center of the intersection is the (100) pole and the two pairs of narrow parallel lines are {200} type planes. Structure factor calculations that apply to x-ray diffraction patterns also apply to channeling patterns, although electron scattering coefficients can enhance or decrease the contrast of some planes (Joy, 1974). Thus, the pairs of lines are {200} planes rather than {100}, which are not allowed in the diamond cubic structure. Parallel to the {200} planes are higher order planes ({400}, {600}) with lower contrast.

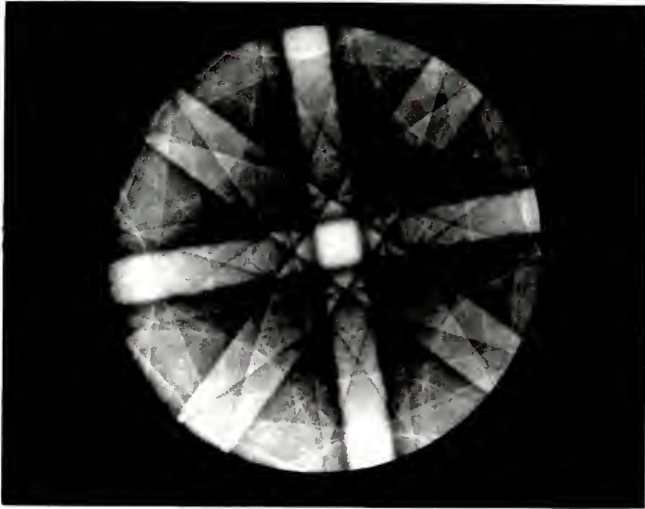


Figure 1.5 Selected area channeling pattern for (100) silicon at 35 kV.

By tilting the specimen, channeling patterns for other crystallographic orientations can be obtained. For cubic systems, a single stereographic triangle will cover all possible orientations. For crystal systems with lower symmetry, larger regions will be required. Figures 1.6 and 1.7 show the (110) and (111) poles for silicon.

An obvious use of electron channeling is crystallographic orientation. Channeling has the advantages over x-ray orientation in that smaller areas (1-10 μm versus 1-2 mm) can be examined, and thus individual grains in a polycrystalline surface can be oriented. Although in theory unknown samples could be oriented by measuring the band widths of planes and angles between planes and calculating which planes appear on the channeling patterns, in practice such calculations are cumbersome and orientations are more easily accomplished by comparison with channeling maps prepared from specimens of similar crystal structure, Kikuchi patterns, or with patterns generated by computer (Payne and Ralph, 1980).

In a comparison between x-ray Kossel patterns and electron channeling patterns for determination of the orientation of individual grains into polycrystalline samples, both techniques achieved an accuracy within one degree (Joy et al., 1971).

Electron channeling contrast exists not only in backscattered electrons, but also in x-rays, emitted photons, secondary electrons and specimen current. Of these, backscattered electrons and specimen current are most commonly used due to their ease of detection at the small working distances required to minimize electron optical aberrations (Van Essen et al., 1970). However, the specimen current amplifier can introduce a

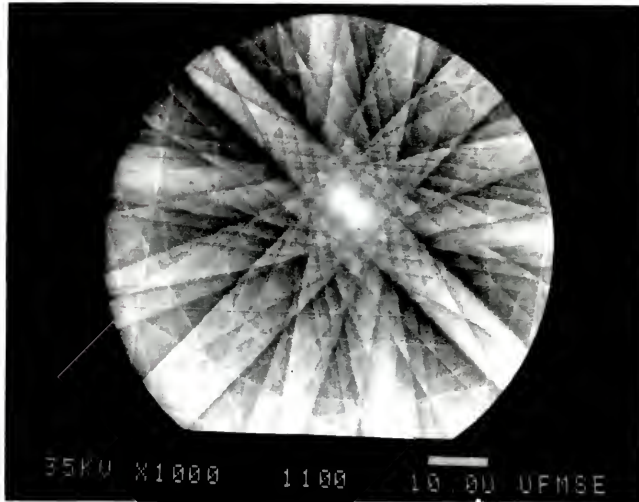


Figure 1.6 Selected area channeling pattern of (110) silicon at 35 kV.

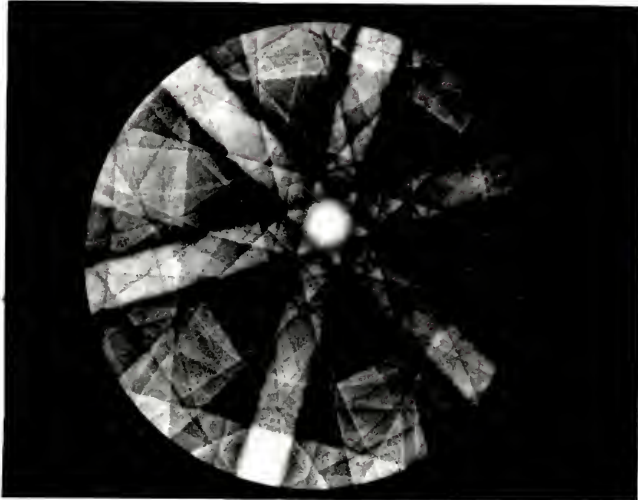


Figure 1.7 Selected area channeling pattern of (111) silicon at 35 kV.

derivative of the signal and contrast inversion (Shaw et al., 1969). Backscattered electrons are most conveniently collected with a split ring annular semiconductor detector located above the sample (Newberry and Yakowitz, 1975).

Since channeling contrast is quite small, on the order of 5% (Joy, 1974), collected signals must be enhanced, either by subtraction of a D.C. component before amplification, use of an A.C. amplifier, or by signal differentiation. Signal differentiation was used in early work by Coates (1969) to enhance fine lines in the patterns. Quantitative measurements of signal level of a differentiated signal have relatively little significance, however.

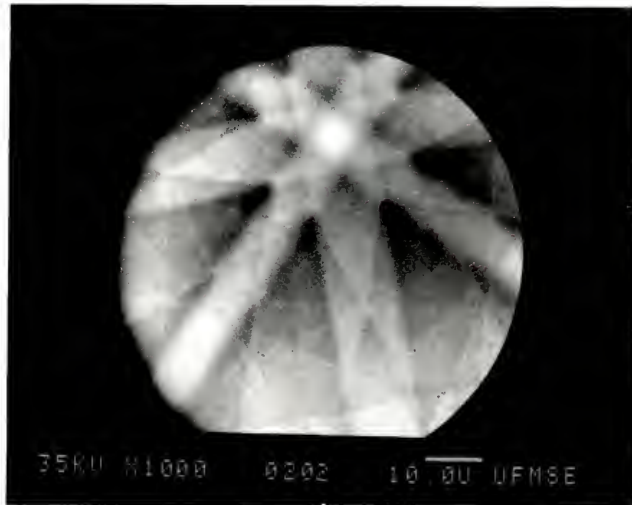
Despite the fact that a 20-35 kV electron beam penetrates a specimen to a depth of several microns, electron channeling contrast arises only near the specimen surface. Wolf et al. (1969) showed that an amorphous layer of silicon 300 Å thick eliminated channeling contrast from silicon single crystals. Schulson et al. (1969) found that 900 Å of carbon had the same results. The contrast loss from amorphous films may be due to decollimation of the incident beam (Davidson and Barker, 1970). Theoretical calculations by Gregory et al. (1977) revealed that the depth from which electron channeling contrast is obtained depends on beam energy and sample atomic number and varies from 25,000 Å for silicon and 1200 Å for gold, both at 30 kV. Farrow and Joy (1981) experimentally measured the depth of channeling contrast at ~ 11 kV at 1000 Å in tungsten.

Thus, surfaces of specimens for electron channeling must be clean from contaminants. This is usually accomplished by chemical etching or electropolishing.

1.2 Effects of Dislocations on Electron Channeling Patterns

In addition to being sensitive to surface films, electron channeling patterns are sensitive to the degree of perfection of the lattice in the volume being channeled (Holt et al., 1968). Crystalline defects that strain the lattice, such as interstitials, vacancies and dislocations, also change the channeling pattern. Since the strain field of an individual defect is limited ($< 200 \text{ \AA}$) and the area being channeled is relatively large ($\sim 10 \text{ }\mu\text{m}$), there must be a substantial number of defects to produce a measurable change in the channeling patterns. Changes in the patterns with increasing numbers of defects include loss of contrast, loss of sharpness; i.e., higher order lines disappear and lower order lines become less defined, and an increase in the width of individual lines. In addition, bands may bend with or without the other effects. An illustration of the effects of plastic strain on channeling patterns for stainless steel is shown in Figure 1.8. The difficulty has been to get quantitative information from these effects.

In the absence of a simple, quantitative theory of electron channeling contrast in either perfect or imperfect crystals, early efforts on the effects of dislocations on channeling patterns tended to be almost all experimental or almost all theoretical. From the experimental approach Davidson (1974) strained a tapered specimen of Fe-3% Si and compared channeling patterns of selected grains before and after straining. The use of a tapered sample allowed a range of strains to be obtained from a single specimen. Local strain was determined by measuring the change in spacing of scratches placed on the surface of the specimen before loading, and varied from .4% to 8.3%. Grains selected for measurement had random orientations.



(a)



(b)

Figure 1.8 Effect of strain on electron channeling patterns.
(a) unstrained. (b) 8% tensile strain.

Strains of unknown grains were determined by visual comparison with the known standards. The human eye is "rather sensitive in comparisons of overall pattern contrast and distortion, widths of both high and low index diffraction lines, and determination of whether higher order lines appear in the ECP" (Davidson, 1974, p. 924). Strains can be determined to an accuracy of approximately 1%. Thus, the accuracy lost by using a non-quantitative measurement technique is approximately compensated by using the entire channeling pattern for evaluation rather than a single line.

Plastic strain is characterized on the atomic level by the presence of dislocations. It is also highly inhomogeneous in that the concentration of dislocations in a uniformly strained sample varies widely from point to point within the sample. Thus, dislocation density is a more fundamental parameter than plastic strain on an atomic level.

Stickler et al. (1971) and Stickler and Booker (1972) prepared a series of polycrystalline materials strained by known amounts. The effects of strain on the channeling pattern were quantified by measuring the width of the finest line visible on the pattern, regardless of orientation. Specimens were also examined and dislocation densities determined by transmission electron microscopy. Metals examined were nickel, 316 stainless steel, Dicalloy, and Inconel 744. The width of lines for unstrained samples depended on the order of the line. Line width correlated with dislocation density better than it did with strain, as might be expected. No "universal curve" of line width versus dislocation density was obtained, necessitating calibration runs for determining dislocation densities of unknown specimens.

Joy and Newberry (1971) studied channeling patterns on several strained superplastic alloys. Specimens were deformed at high and low temperatures relative to their melting points. For low relative temperatures channeling pattern contrast decreased and line width increased with increasing strain, as has been previously observed. Lattice rotation sometimes occurred, but no bending of lines in the channeling patterns was observed. The same effects were observed on specimens deformed at high relative temperatures, but bands on the ECP were bent. It was proposed that this effect is due to lattice bending due to subgrain formation, each subgrain having a slight misalignment. Individual subgrains have a relatively dislocation-free lattice, with dislocations concentrated at the subgrain boundaries. Thus, if individual subgrains are dislocation-free, bending of the electron channeling pattern will occur with high contrast still present. If the subgrains have substantial dislocation concentrations, the contrast will also decrease.

A more quantitative technique for measuring the changes in pattern quality is the spectral distribution of the Fourier components of an intensity profile, first tried by Davidson (1974). The unstrained lattice, containing more higher order (fine) lines and greater contrast would be expected to have a greater amplitude in the higher frequencies. Conversely, a highly strained sample, with broad bands and low contrast, would shift amplitudes towards lower frequency. Unfortunately, spectral density plots can shift widely for different scan lines in a single channeling pattern. Thus, for accurate comparison, line scans on standard and unknown specimens would have to be made along the same crystallographic direction, a condition difficult to achieve experimentally. However, the development of computers

with storage capacities sufficiently large to record an entire image might eliminate this problem by determining the Fourier transforms from an area of the channeling pattern rather than a single line.

In an early effort to correlate theory and experiment, Schulson (1971a) derived a simple equation for the width of a channeling pattern line in a perfect crystal from two beam theory:

$$2 w_g = \frac{2}{\xi_g |g|}$$

where $2 w_g$ = line width from maximum to minimum of intensity profile

ξ_g = extinction distance for line being observed

$|g|$ = magnitude of the reciprocal lattice vector for line
being observed

Later (Schulson, 1971b) this equation was expanded to include the effects of dislocations and theoretical calculations compared to intensity profiles obtained by microdensitometer scans of photographs of electron channeling patterns obtained from silicon single crystals whose surface had been abraded with alumina or diamond powder in sizes from .05—1.0 μm . As would be expected, both the theory and experiment resulted in a decrease in contrast and an increase in line width with increasing lattice distortion. By measuring the experimental band widths, the relative lattice rotation caused by the subgrains resulting from abrasion can be calculated. No dislocation density or strain was determined on the abraded specimens.

As a sample is strained, the contrast of lines decreases until no pattern is discernible. As strain is increased, the higher order lines disappear first and lowest order lines last. This has led several investigators into measuring strain or dislocation density by observing which

lines were still present in the channeling pattern. In a review and reanalysis of data previously collected, Spencer et al. (1974) developed a theory for calculation of the dislocation density at which various orders of lines disappear. This occurs when the contrast is reduced to the level of background noise. This theory is then used to calculate line widths for previously gathered data. Once the theory had been corrected for beam divergence and line broadening, good agreement was obtained between theory and experiment except at very high dislocation densities. Random dislocation types were assumed.

In a similar study by Gregory et al. (1977) single crystals of copper stressed along $\langle 110 \rangle$ directions and sliced parallel to $\{111\}$ planes were examined. The same equations developed by Spencer (1974) were used to predict the disappearance of lines, and good agreement again was obtained when corrections for line broadening, probe size and probe divergence were incorporated. Dislocation densities required for line disappearance are presented in tabular form, allowing dislocation densities to be determined by observing which lines are present in the channeling pattern; e.g., if the $\{311\}$ lines are present, the dislocation density must be $< 8 \times 10^{10}$.

S. M. Davidson and Booker (1971) used an equation to calculate the strain field around a dislocation. By calculating the area on the surface of the specimen with a lattice strain greater than a given value for a single dislocation, the dislocation density required to reduce the pattern resolution to that value of strain is the reciprocal of this area. The agreement of this equation with theory is relatively poor at low dislocation densities.

D. L. Davidson (1980) used a more elaborate equation to calculate average strain and strained volume to re-evaluate the data gathered by Gregory et al. (1977) and achieve better matching to theory and experiment. Central to the development is the concept that the volume of material strained is more important than the level of the strain.

The studies cited above are aimed at experimental determination of plastic strain or dislocation density. There are other studies on the prediction of electron channeling contrast based on detailed examination of the interaction of Bloch waves with crystalline solids. Studies have been done by Hirsch and Humphries (1970a), Hirsch and Humphries (1970b), Howie et al. (1971), and Spencer and Humphries (1980). Although these studies are significant in that they provide insight into the channeling process, their agreement with experimental data, although steadily improving, is not yet perfect. The equations involved are complex and require a computer to solve. Vicario et al. (1970a) generated a computer simulation of a small area of a channeling pattern, similar to the dislocation simulations used in TEM.

Spencer et al. (1972) studied backscatter electron contrast from perfect and imperfect crystals, but their study was oriented toward defining beam conditions for imaging individual dislocations as opposed to evaluating changes in entire channeling patterns. Zackowitz and Pantell (1981) studied the effects of dislocations on the physics of electron channeling, but no experimental data were presented.

The gap between theory and experiment for channeling patterns on samples containing dislocations is still substantial.

1.3 Scope of the Present Research

Studies of the effects of dislocations on electron channeling patterns have assumed that the strains produced are random. Although this may be true in many cases, the strain field resulting from an individual dislocation has highly directional qualities and if a directionality existed in the dislocation field this should be reflected in different strains existing on different planes, and thus measurement of band width changes on a single plane could lead to errors in strain measurement. This effect was noticed by Joy and Newberry (1971). Measurements on several planes should allow some information about the Burgers vector on a field of dislocations and could be determined by the electron channeling pattern (Booker, 1971).

Any effects of uniform arrays of dislocations will be maximized by having parallel arrays of dislocations of the same Burgers vector. The type of dislocations present can most conveniently be determined by using thin specimens and examining the channeled area by transmission electron microscopy.

Thus, half of this dissertation will consist of a detailed examination of the effects of large arrays of parallel dislocations on electron channeling patterns.

Electron channeling has not been used to measure elastic strain from shifts in the Bragg angle as is done in x-ray techniques. This is for two reasons: The intensity profiles near the Bragg condition for electron channeling are not as easily mathematically modeled as the parabola used for x-rays and the incident electrons in channeling are not nearly as

monochromatic as the emission peaks used in x-rays. This makes the small changes in Bragg angle ($\sim 1\%$) caused by elastic strain difficult to measure.

On the other hand, x-rays only measure changes in planes that are approximately perpendicular to the beam. In the case of simple tensile loading, these planes diffracting are approximately parallel to the applied load, and thus have their spacing changes diminished by the Poisson effect. Also, only those crystals (in a polycrystalline sample) which are properly oriented towards the beam are being examined. Finally, the smallest beam commonly used is 1-2 mm in diameter. Electron channeling measures all planes approximately parallel to the electron beam, including those that would have a maximum amount of spacing change under stress. All grains can be measured in a polycrystalline sample, and the beam size is $\sim 10 \mu\text{m}$, allowing grain-by-grain strain determination in many cases.

Thus, if a way could be found to measure elastic strain, channeling has a broader range of application than x-ray measurement of a strain. Fortunately, there is a series of fine lines in electron channeling patterns that are from the first order Laue zone. The origin and geometry of these lines will be fully developed in Chapter 3, but their position is the result of a small difference between two large angles, the Bragg angle and the angle the plane makes with the pole near which they are being observed. The planes forming this fine structure are relatively high order planes, and thus are relatively sensitive to small changes in lattice spacing caused by elastic strain. Thus, a small percentage change in the d-spacing can cause a measureable change in the position of the lines comprising the fine structure.

The second goal of this research will be to show the feasibility of using electron channeling to measure elastic strain.

CHAPTER 2
OPTICS OF ELECTRON CHANNELING

2.1 Basic Optics of Magnetic Lenses

Magnetic lenses are used to focus electron beams just as optical lenses are used to focus light. The mathematics that describes optical lenses also describes magnetic lenses. If a parallel beam of electrons enters a lens, it will converge at a distance behind the lens defined as the focal length. If an object is located on one side of a lens, an image will be formed on the other and the Gaussian form of the thin lens equation applies:

$$\frac{1}{S_o} + \frac{1}{S_i} = \frac{1}{f}$$

where S_o = distance from the lens to the object

S_i = distance from the lens to the image

f = the focal length of the lens.

For the case of parallel rays, the object is at infinity, and the equation reduces to

$$\frac{1}{S_i} = \frac{1}{f}, \text{ or } S_i = f$$

i.e., an image is formed at the focal point of the lens.

The force of a magnetic field on an electron beam is

$$F = -e (v \times H)$$

where e = the charge on an electron

v = the velocity of the electron

H = the magnetic field strength.

The magnetic field strength, H , is proportional to NI , where N is the number of coils in the lens and I the current through them. Thus, in contrast to optical lenses, magnetic lenses may have their focal length varied by varying the current through the coil.

Since the velocity of an electron, v , is

$$v = \sqrt{\frac{2E}{m}}$$

where m = mass of an electron

E = beam energy.

At constant lens current, the focal length of a lens changes with the accelerating potential of the beam.

Magnetic lenses suffer from a variety of distortions that prevent the beam from being focused at a single point. Chromatic aberrations result from the beam having a small but finite range of energy, with the extremes of the range being focused at slightly different points, as described above. Electron diffraction occurs any time electrons pass through an orifice. Electrons travelling in a beam interact to produce transverse velocities. All of these are relatively insignificant when compared to astigmatism and spherical aberration.

Astigmatism results from small inhomogeneities in the mechanical construction of the lens and results in a beam of elliptical cross section rather than circular. Fortunately, this can be corrected by small additional coils located on the bottom of the lens.

Spherical aberration results from rays entering the lens near the periphery being more strongly focused than those entering near the center, as illustrated in Figure 2.1. The minimum obtainable beam diameter is

$$d_{\min} = C_s \alpha^3$$

where d_{\min} = minimum beam diameter

C_s = spherical aberration coefficient

α = angle between ray and lens axis.

The spherical aberration coefficient, C_s , is a function of the energy of the electrons and the focal length of the lens. Geometry gives

$$\tan \alpha = \frac{C_s \alpha^3}{\Delta f}$$

where Δf is the maximum change in focal length due to spherical aberration.

Rearranging, and assuming that for small angles, $\tan \alpha \approx \alpha$, gives

$$\Delta f = C_s \alpha^2$$

Spherical aberration cannot be corrected for normal lens use and serves as the most significant limit to lens performance. Fortunately, for the special case of electron channeling, spherical aberration can be corrected. This will be discussed in section 2.3.1.

2.2 Conventional Operation of the Scanning Electron Microscope

The components of a typical two-lens scanning electron microscope (SEM) are shown schematically in Figure 2.2. The purpose of the optical system is to produce a beam of minimum diameter on the specimen surface with sufficient current to produce a detectable signal. The basic elements

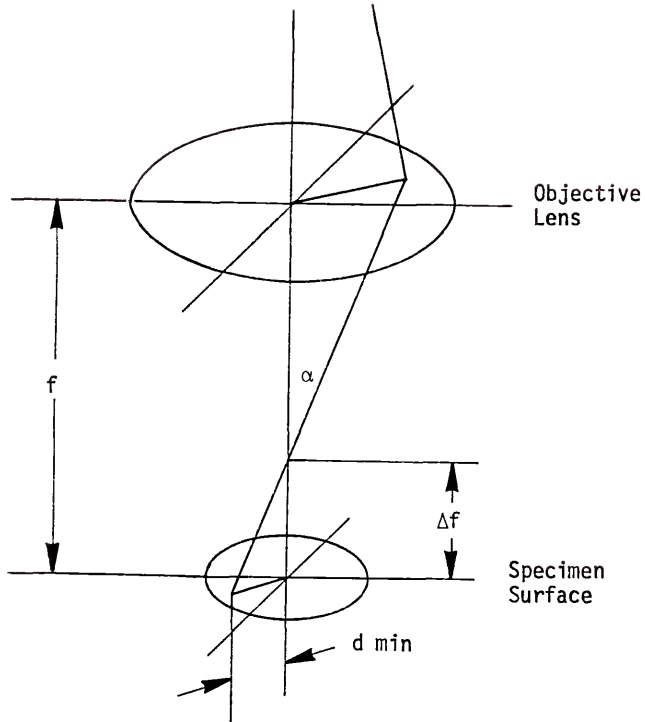


Figure 2.1 Spherical aberration in an electromagnetic lens.

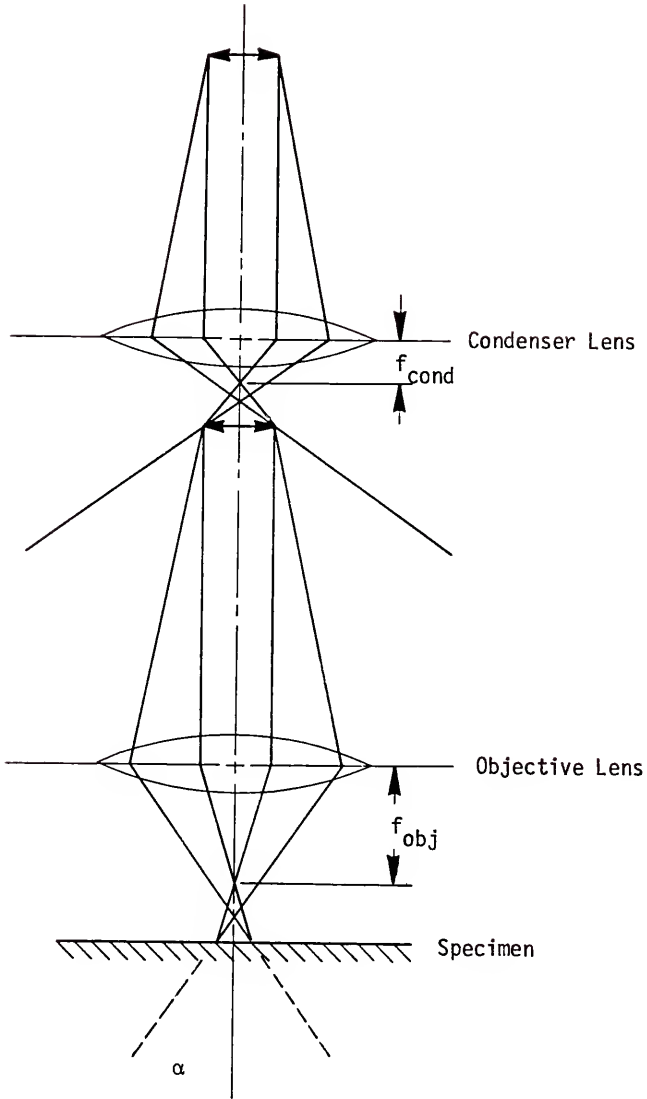


Figure 2.2 Ray diagram for a typical two-lens SEM.

are a source of electrons, a condenser lens, an objective lens, scan coils, and a detector.

The electron source is most commonly a heated tungsten filament producing electrons by thermionic emission. The Wehnelt cup surrounding the filament carries a negative bias of 0-500 V and serves to confine the emitted electrons to a beam of 25-100 μ in diameter.

The electrons leaving the Wehnelt are subjected to an accelerating potential of 10-50 kV. The condenser lens serves to focus, or demagnify, the beam. It controls the final beam current, as illustrated in Figure 2.3. In case (a), corresponding to a low condenser lens current, a much higher fraction of the total beam passes through the aperture, resulting in a higher beam current than in case (b), which is for a higher condenser lens current. A lower lens current also enhances spherical aberration, which results in a larger beam size at crossover and ultimately results in a large spot size at the specimen surface.

The objective lens performs the final focusing of the beam and determines the spot size on the specimen. An aperture is generally installed between the condenser and objective lenses and between the objective lens and the specimen. These serve to limit the beam divergence. Were it not for lens aberrations, production of a minimum size spot would be straightforward. The most severe distortion, spherical aberration, is a function of the cube of the beam divergence (d). Thus, limiting divergence becomes important in producing a minimum size spot. Typical spot sizes are 50 \AA to 1 μm .

The beam is scanned across the specimen surface by two sets of scan coils located in the objective lens as shown in Figure 2.4. The first

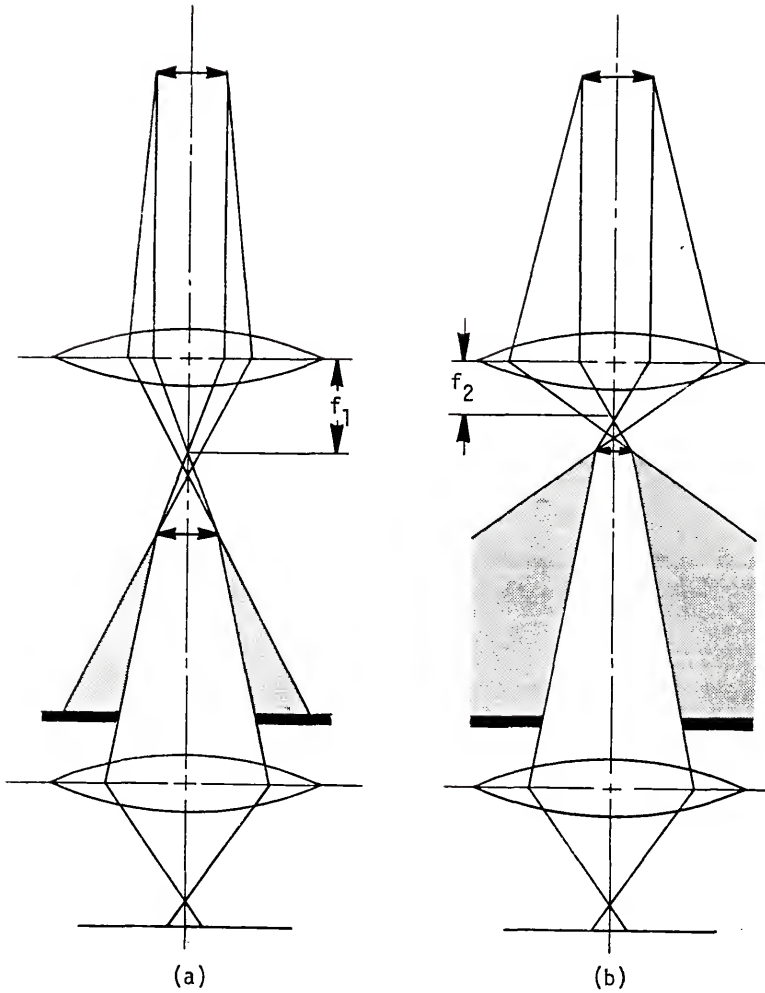


Figure 2.3 Effects of condenser lens strength on beam current. Case (a) has a longer focal length on the condenser lens than (b). Since a greater portion of the beam passes through the objective lens in (a), it has the higher beam current at the sample surface.

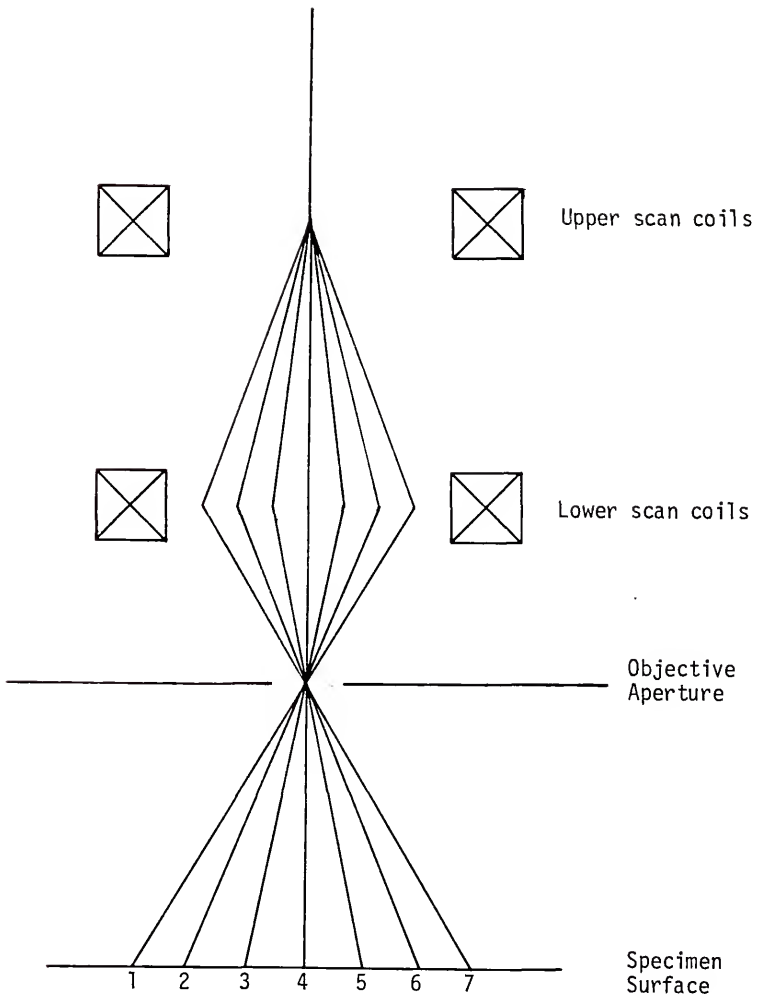


Figure 2.4 Operation of a scanning system using two sets of scan coils.

set deflects the beam axis, and the second deflects it through the objective aperture and on to the specimen surface. The magnitude and direction of the final deflection of the beam on the specimen surface varies linearly with time. The deflection of the beam is coordinated with the deflection of a beam in a cathode ray tube (CRT). The intensity of the CRT beam is proportional to the magnitude of the signal produced by the detector.

When a single scan is completed, the beam is moved an incremental amount in a direction perpendicular to the scan line and the process is repeated. The length of an individual scan line and the distance between successive scan lines is determined by the magnification, a smaller area being scanned for higher magnification.

The events that occur when an electron beam strikes a solid surface are illustrated in Figure 2.5(a). Usually backscattered electrons are detected in electron channeling, but secondary electrons or specimen current can also be used. Secondary electrons are produced in large numbers and have relatively low energies, as shown in Figure 2.5(b). Backscattered electrons have energies approximately equal to the beam energy. Backscattered electrons are usually detected by a solid state detector which measures the current produced when electrons strike a p-n junction. This type of detector is mounted immediately below the objective lens, allowing short working distances. Secondary electrons are sensitive to surface topography and are most commonly used to produce an image of the specimen surface. Electron channeling produces the most contrast in backscattered electrons.

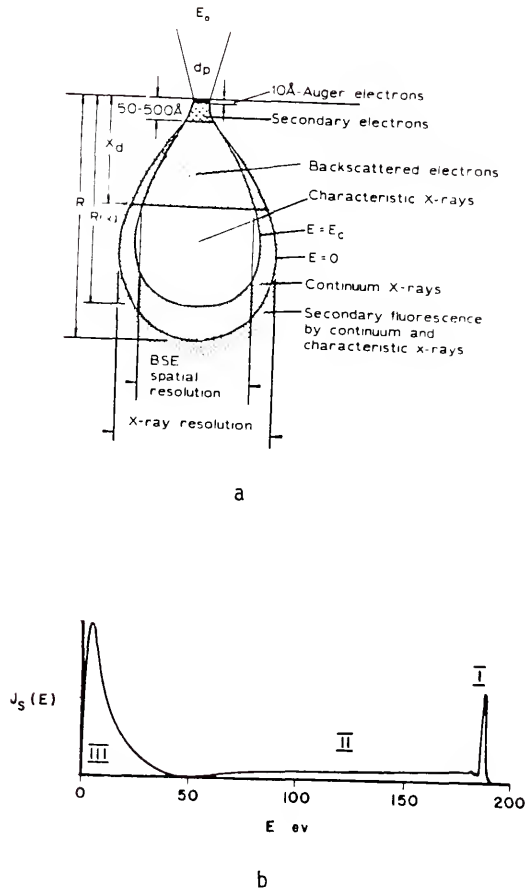


Figure 2.5 (a) Events occurring where an electron beam strikes a solid. Backscattered electrons and secondary electrons are commonly used for imaging in an SEM. (b) Intensity distribution ($J_S(E)$) of emitted electrons for a beam energy of 180 eV. Region III is secondary electrons, Region I backscattered electron.

2.3 Optics of Electron Channeling

2.3.1. Introduction

Electron channeling may be crudely observed with a conventionally operated SEM, although the contrast is very low, as shown in Figure 1.1. It was in this fashion that electron channeling was first observed by Coates (1967). Low magnifications are necessary to get a large angular change of the beam during scanning. Thus, specimens are limited to large single crystals, since polycrystalline materials would give overlapping patterns.

The resolution of such channeling patterns can be improved in two ways: 1) the beam divergence must be minimized (Coates, 1968), and 2) the beam must pivot about a single point on the specimen surface rather than be scanned across it (Coates, 1969).

The current in the beam is governed by the following relationship:

$$I_b = 2.5 d^2 \alpha^2 B$$

where I_b = beam current

d = beam diameter

α = beam divergence

B = a constant depending on the type of electron source.

The beam current is fixed by the detector sensitivity and is typically 10^{-8} to 10^{-9} amps. Thus d and α may not be independently varied. The value of d for $\alpha = 10^{-2}$ rad. is $1.0 \mu\text{m}$. For $\alpha = 2 \times 10^{-4}$ rad., $d = 50 \mu\text{m}$ (Joy, 1974).

There are several ways beam divergence can be minimized, as shown in Figure 2.6 (Schulson and Van Essen, 1969). The total divergence of the beam

is the sum of two contributions, one depending on the strength of the objective lens and the size of the final aperture, and the other on the finite size of the beam at crossover. In Figure 2.6, these are designated ϕ and ψ , respectively. Figure 2.6(a) shows conventional operation. Typical values for α are 10^{-2} rad. Case (b), the final lens is turned off. Beam divergence is lowered to approximately 10^{-3} rad., but the beam size is now approximately the size of the objective lens aperture; i.e., several hundred microns. This is a simple method of improving the quality of channeling patterns obtained with two-lens instruments.

Figure 2.6(c) corresponds to beam crossover being at the focal point of the objective lens. In this case the only contribution to the beam divergence is the finite size of the beam at crossover, and values of α can be obtained at $\approx 10^{-4}$ rad. The beam diameter is the size of the final aperture, this can be reduced to approximately $10 \mu\text{m}$ while still maintaining sufficient current for the detectors. This type of operation can be obtained with a two-lens instrument, but switching between conventional images and channeling patterns is cumbersome.

Having obtained a collimated beam, the scanning must be altered to produce beam rocking about a single point on the specimen surface. This can be accomplished electronically in three ways: the double deflection system, in which the strength of the lower scan coils is reduced; addition of an after lens deflection coil; or deflection focusing, where the objective lens replaces the lower scan coils. These are illustrated in Figure 2.7.

Figure 2.7(a) is the conventional scanning system and the double deflection system is illustrated in Figure 2.7(b) (Schulson and Van Essen, 1969). The objective aperture must be removed, since the beam is displaced

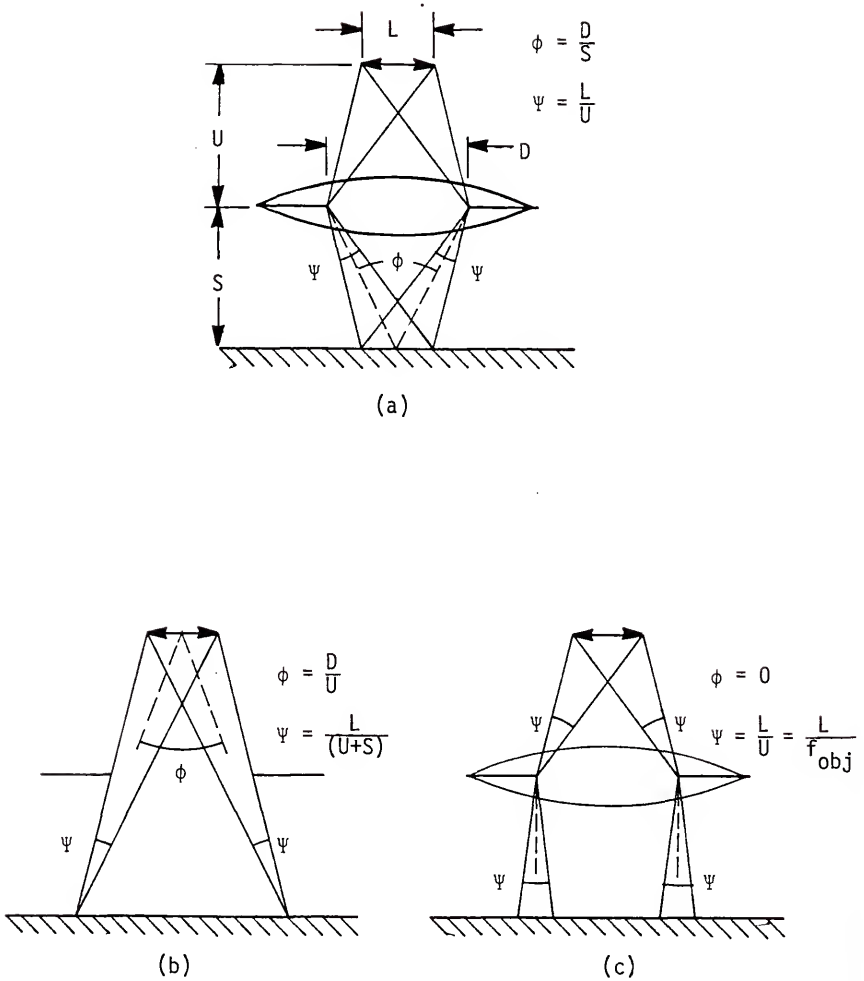


Figure 2.6 Methods of reducing beam divergence. (a) conventional image operation (b) objective lens turned off (c) focal length of objective lens at condenser lens crossover (Schulson and Van Essen, 1969).

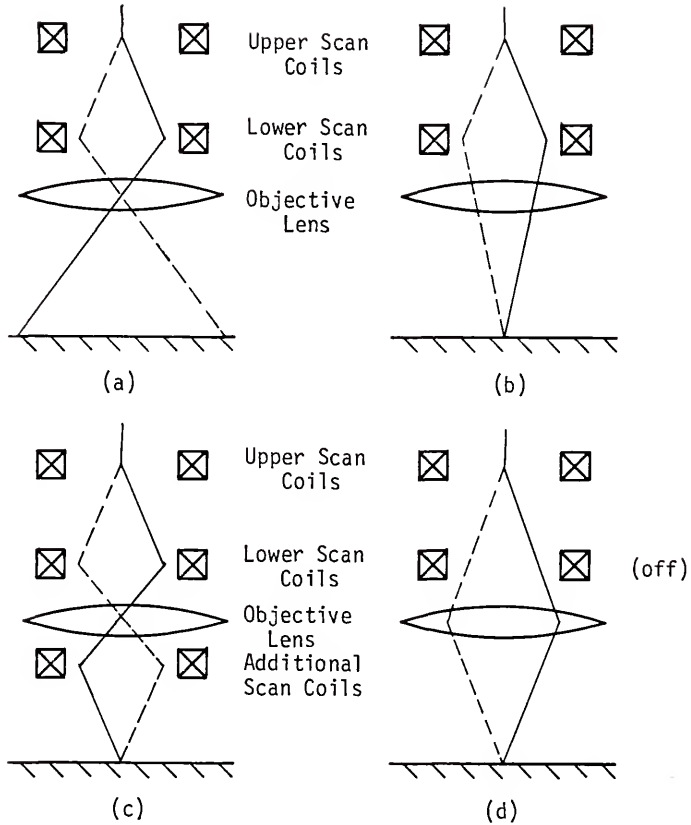


Figure 2.7 Scanning systems for selected area channeling. (a) conventional operation. (b) double deflection, (c) after lens deflection, (d) deflection focusing.

a considerable distance in the plane of the objective lens. This method was employed in early work on the Cambridge Stereoscan. Figure 2.7(c) shows the after lens deflection coil (Lane et al., 1974). The objective aperture does not need to be reduced in size, the conventional scan coils are left on, and the additional scan coil needs only to be turned on and off for channeling operation. This system is used by ETEC Corporation in its microscopes. Figure 2.7(d) shows deflection-focusing, where the bottom scan coil is turned off and the beam deflected by the objective lens (Van Essen et al., 1970). The objective lens both deflects and collimates the beam. This method is used in appropriately modified Cambridge Stereoscans and JEOL machines equipped for channeling.

The choice of scan system is a combination of convenience and the ease with which the aberrations introduced by the scanning system may be corrected. The aberrations introduced by the scanning system determine the area channeled, and thus limit performance. The double deflection system introduces aberrations that are difficult to correct. This method is not used currently. Adding a third scan coil compounds the problem, but the after lens deflection coil makes operation more convenient. The most used system is deflection-focusing technique, primarily because the aberrations may be relatively easily corrected.

Lens currents must be changed along with the scanning system for channeling operation to produce a beam with minimum divergence, as discussed previously. The method shown in Figure 2.6(c) produces the lowest divergence and is most commonly used. By changing the current in the

condenser lens only the objective lens current remains unchanged between channeling and conventional operation. This is usually accomplished by the addition of a relatively weak third lens between the condenser and objective lenses whose current changes when mode of operation is changed.

Figure 2.8 shows a cross section of a JEOL JSM 35C, a three-lens SEM designed for channeling operation via the deflection-focusing scanning system.

Regardless of the scanning system used for channeling operation, a rotation exists between the topographic image and the channeling pattern. This rotation consists of two components, one of 180° and the other substantially smaller. One or both of these components are present in all scanning systems.

The origin of the 180° reversal of the SACP with respect to the topographic image is shown in Figure 2.9, which assumes, for clarity, that the channeling pattern and image are being obtained with a conventional scan system. Figure 2.9(a) shows a flat specimen, normal to the beam, during a single line scan across the specimen surface, from point A to point B, during which time the beam in the cathode ray tube (CRT) also makes a single scan of the image. Both the SEM beam and CRT beam move from left to right.

If the sample is also a single crystal with a low index pole perpendicular to the surface, this pole will appear in the middle of the scan line when looking at the electron channeling pattern, at the point marked P.

If the sample is tilted, as shown in Figure 2.9(b), the topographic image will change to reflect the tilt of the specimen. Point B will be

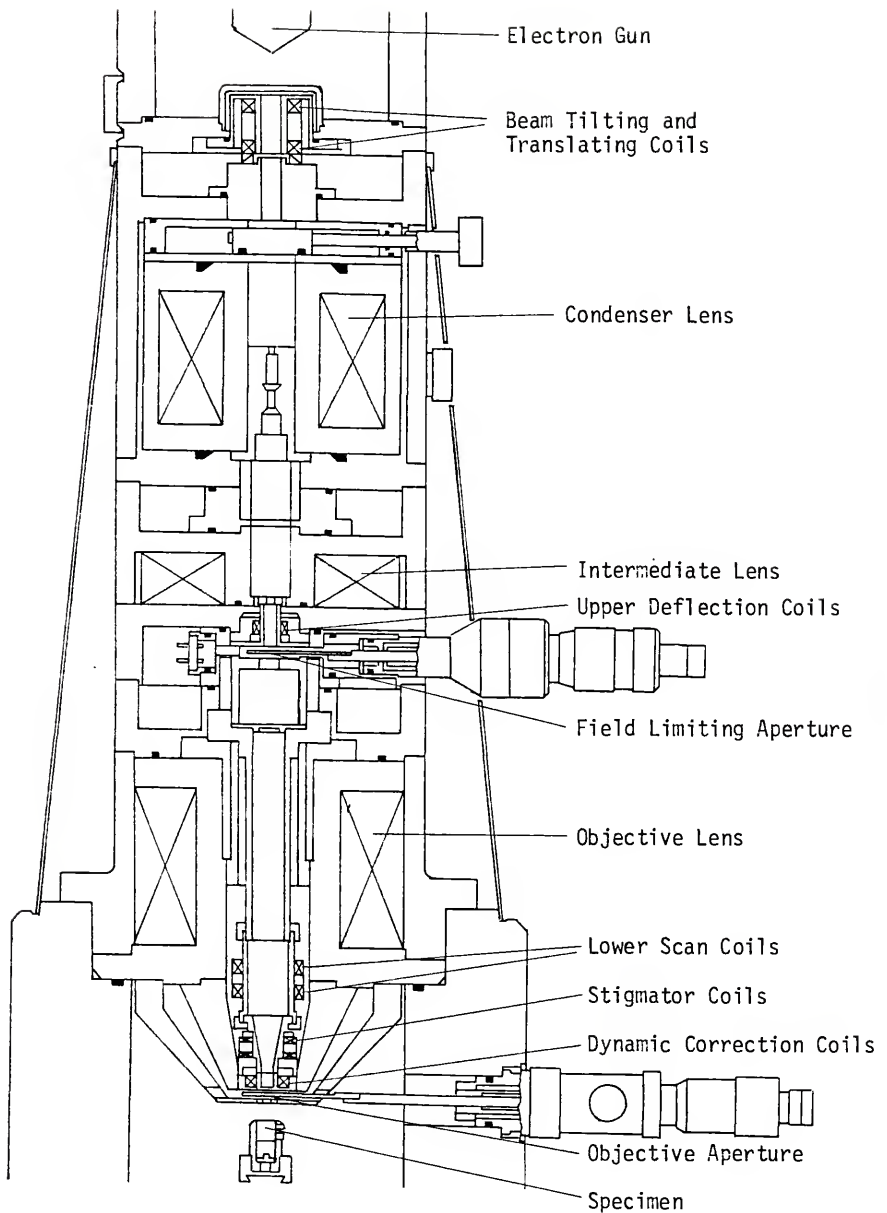


Figure 2.8 Cross section of a JEOL JSM 35C three-lens SEM.

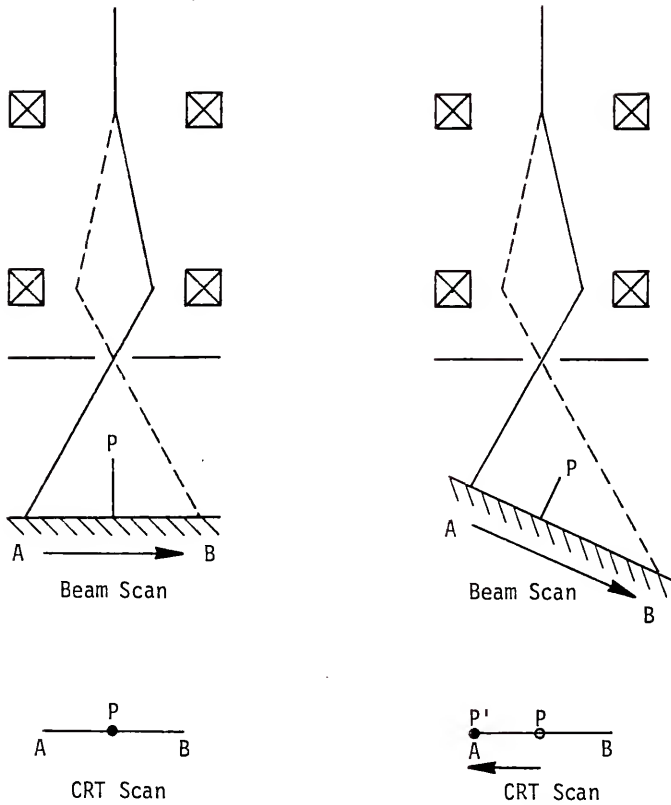


Figure 2.9 Apparent 180° rotation of SACP relative to image. Specimen is a single crystal with pole P . When specimen is tilted to the right, the pole moves to the left in the SACP.

at a greater working distance than point A and the image of the specimen appears tilted "to the right." For the channeling pattern, the pole P has moved closer to the angle of the beam at point A and away from the angle of the beam at point B. This is a movement to the left on the image, to the point P'. This is opposite to the image movement. The effect can be accounted for by rotating the channeling pattern 180° with respect to the image photograph.

This 180° rotation exists in the double deflection and deflection-focusing scanning systems but not the after lens deflection system (Davidson, 1976).

The second component of the rotation is much smaller. It is due to field leakages, etc. and must be measured experimentally by comparing crystallographic directions in the topographic and channeling modes. This can be accomplished, for example, by scratching a (111) silicon wafer along a (110) direction (determined by x-ray) and comparing the scratch direction with the channeling pattern.

In the double deflection system the magnitude of the additional rotation is a function of working distance but may be as large as 34° in the Cambridge Stereoscan (Van Essen and Verhoeven, 1974). Smaller rotations are present in the ETEC machines using the after lens deflection coils, although quantitative plots have not been published because the magnitude of the rotation is a function of both lens current and working distance (Davidson, 1976).

In Cambridge machines using the deflection-focusing scanning system, there is a much smaller rotation (2° - 7°) (Joy and Maruszewski, 1975). This was attributed to stray lens fields.

Experiments by the author to measure small rotations present in the JEOL JSM 35C showed rotations, if present, were too small to measure (i.e., $< 1^\circ$). This was independently confirmed on an identical machine by Russell (1981). Apparently, improved design has eliminated the smaller rotation. The 180° rotation is, of course, still present.

One reason for using the deflection-focusing scanning technique is the relative ease with which the aberrations introduced by the scanning system may be corrected. The effects of aberrations are minimized by addition of a set of scan coils high in the optical column, so that relatively small angular deflections are required, and addition of a set of coils to correct for the spherical aberration of the objective lens.

The effects of spherical aberration are illustrated in Figure 2.10. Electrons entering the lens near the periphery of the lens bore are more strongly focused than those entering near the center. In conventional operation, the beam illuminates the entire area simultaneously, and the effects of spherical aberration cause an expansion and elongation of the beam in the area of the focal point. In channeling operation, the magnitude of the deflection of the beam from the axis is increased, which increases the effects of spherical aberration, but the beam is small ($\sim 10 \mu\text{m}$) and the entire bore is not simultaneously illuminated. The result of spherical aberration in channeling operation is to cause the beam to wander across the specimen surface, thus increasing the area being channeled.

A quantitative analysis of the effects of spherical aberration on beam position during channeling operation was investigated theoretically by Booker and Stickler (1972) and experimentally by Joy and Booker (1973).

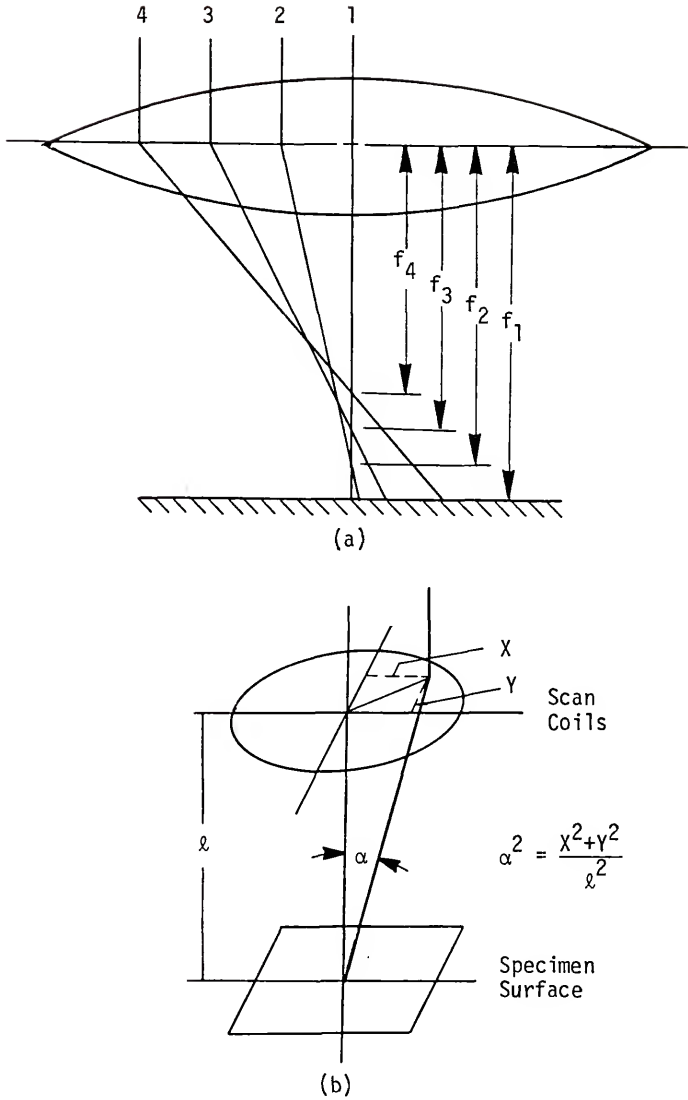


Figure 2.10 Spherical aberration during SACP operation. (a) As beam approaches the periphery, the focal length decreases. (b) Geometry of beam deflection.

The magnitude and direction of beam travel is a function of focus and C_s , and may be substantial. Since the entire bore of the lens is not simultaneously illuminated in channeling operation, the effects of spherical aberration may be corrected (Van Essen, 1970; Van Essen et al., 1971). This is done with correction coils that either increase the focal length of the lens or shift the beam laterally. The strength of these coils is dependent on the displacement of the beam from the lens axis, with greater strength for greater displacement. This lens operates only in the channeling mode.

2.3.2. The Three-Lens Scanning Electron Microscope

The three-lens microscope allows rapid changing from the conventional, or image, mode to the channeling mode, along with precise location of the channeled area on the conventional image. The modifications to the basic two-lens machine consist of the following:

- 1) an intermediate lens between the condenser and objective lenses.
- 2) an additional set of deflection coils immediately below the intermediate lens.
- 3) a field limiting aperture below the upper deflection coils.
- 4) an additional lens to correct spherical aberration in the objective lens during channeling operation.
- 5) a Selected Area Diffraction Control Unit (SDC) to allow two independent settings of the intermediate lens and additional scan coils, and controls for the correction coils for spherical aberration: This unit has a switch for selecting between three settings, as described in Table 2.1.

TABLE 2.1
OPERATING CONDITIONS FOR SDC CONTROL UNIT

	MODE		
	IMAGE	SAI	SACP
Intermediate lens	adjustable	same as image	adjustable
Main scan coils	on	off	off
Auxiliary scan coils	off	adjustable	same as SAI
Objective lens	adjustable	same as image	same as image
Dynamic correction coils	off	off	adjustable

Image = conventional operation, SAI = selected area image

SACP = Selected Area Channeling Pattern

2.3.3. The Image Mode

Operation of a three-lens microscope in the conventional, or image, mode is shown in Figure 2.11. Its operation is the same as the two-lens SEM described in section 2.2, with the intermediate lens acting as an additional condenser lens. If the machine is not to be used for channeling, the setting on the intermediate lens is somewhat arbitrary if the field limiting aperture is withdrawn. In this case, the intermediate lens is usually set to compensate for accelerating potential of the beam.

If the machine is to be used for both channeling and imaging, the crossover will be adjusted to be at the field limiting aperture in the image mode, and it may be left in place.

2.3.4. The Selected Area Channeling Pattern (SACP) Mode

For channeling operation, the lower scan coils are turned off, the upper scan coils turned on, the field limiting aperture inserted, the objective aperture withdrawn, and the strength of the intermediate lens decreased so that the crossover of the beam occurs at the rear focal point of the objective lens. This results in the rays being formed into a parallel beam. The size of the beam is controlled by the field limiting aperture, as shown in Figure 2.12.

2.3.5. The Selected Area Image (SAI) Mode

The SAI mode is a mixture of the image mode and SACP mode and permits the observation of the area channeled in the SACP mode. This is done by forming the image of the field limiting aperture on the specimen. The intermediate lens is left at the shorter focal length of the image mode

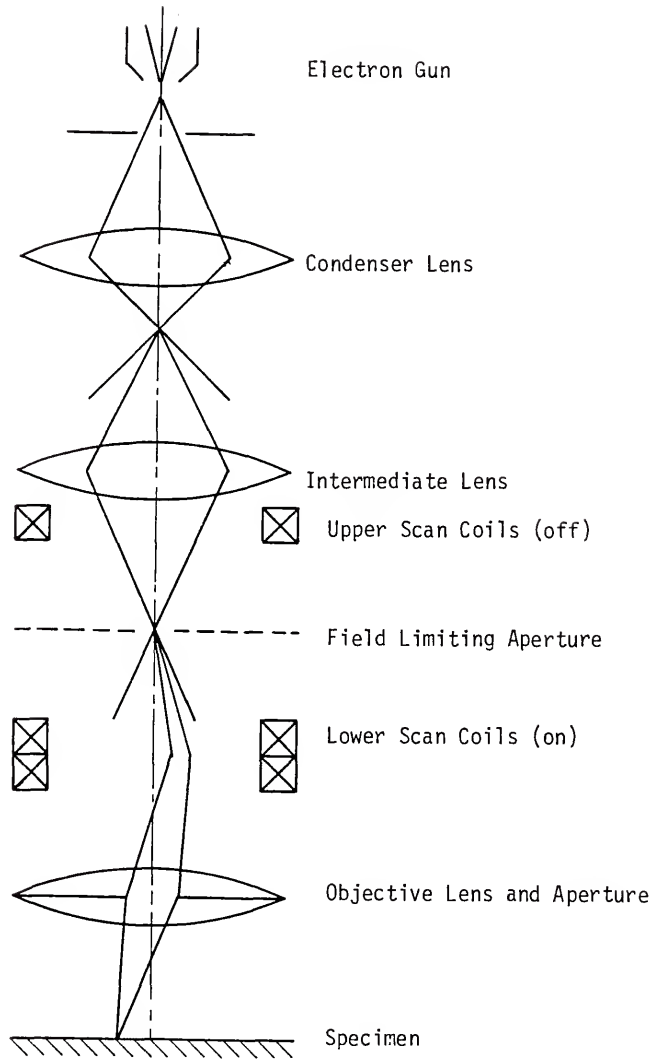


Figure 2.11 Ray diagram for operation of a three-lens SEM in the image mode.

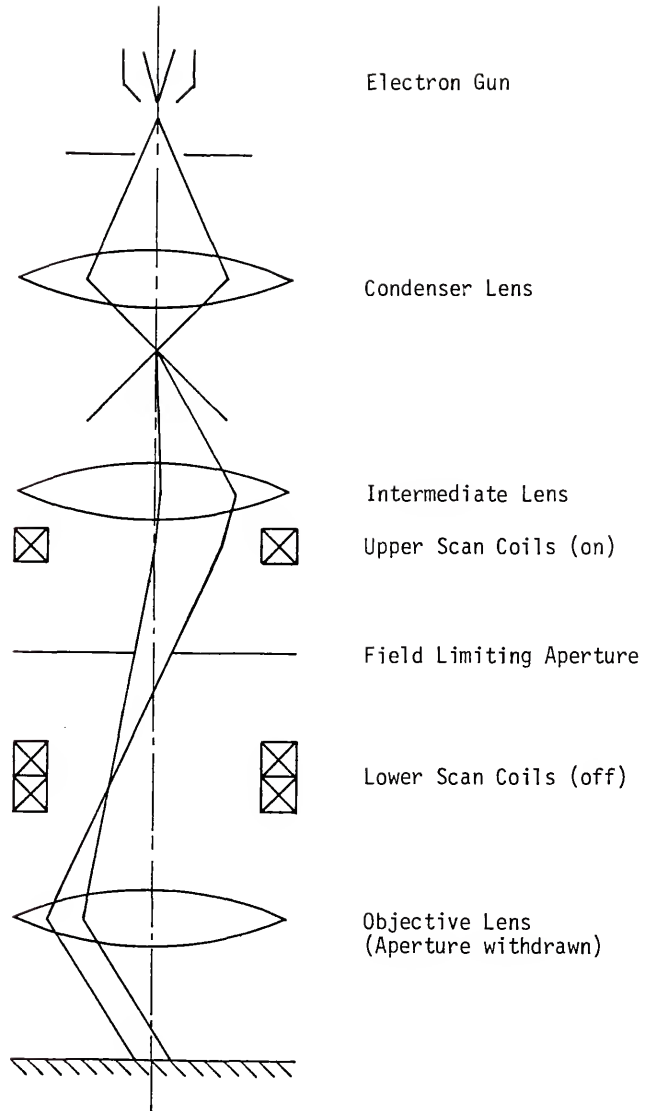


Figure 2.12 Ray diagram for operation of a three-lens machine in the SACP mode.

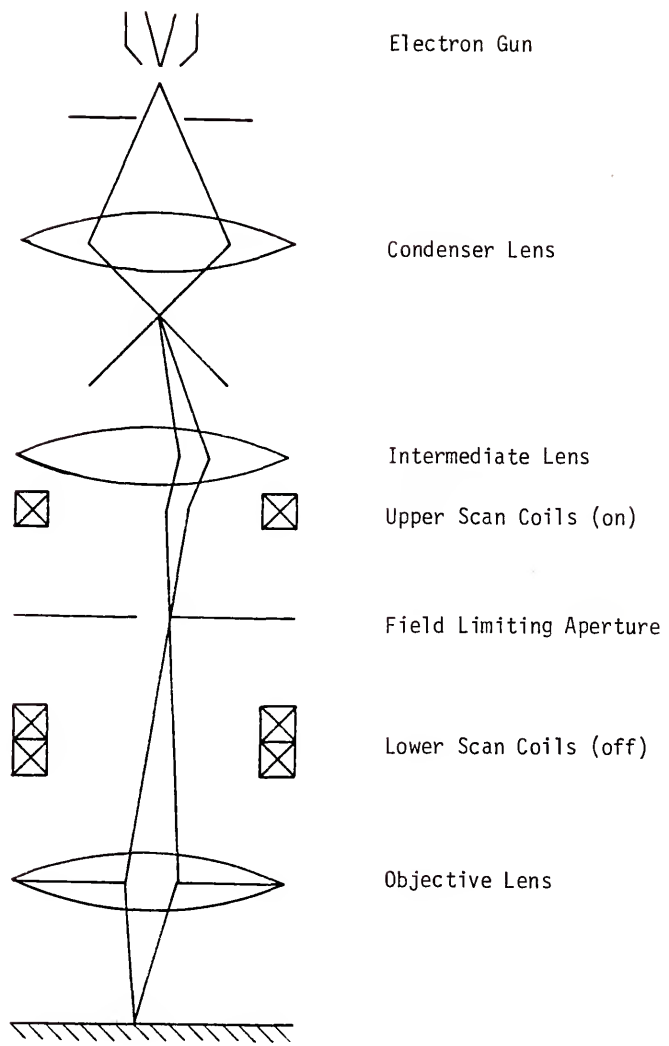


Figure 2.13 Ray diagram for operation of a three-lens SEM in the SAI mode.

but the conventional (lower) scan coils are turned off, and the upper scan coils turned on, as shown in Figure 2.13. Notice that, as the beam is scanned past the edges of the field limiting aperture, it is blanked, but when it passes through the aperture, it scans the specimen surface as it does in the image mode. Thus, the illuminated area of the specimen corresponds to the aperture image.

That the diameter of the aperture image obtained in the SAI mode is the same as the diameter of the beam in the SACP mode is illustrated in Figure 2.15. In the SAI mode, the scanning effectively "pivots" around the objective aperture, and:

$$\frac{d_s}{d_a} = \frac{b}{a} \quad (1)$$

where d_a = diameter of field limiting aperture

d_s = diameter of aperture image on specimen surface

b = distance from objective aperture to specimen surface

a = distance from field limiting aperture to objective aperture.

Using the thin lens equation and realizing that the aperture is an object plane and the specimen surface an image plane

$$\frac{1}{a} + \frac{1}{b} = \frac{1}{f} \quad \text{or} \quad f = \frac{ab}{(a+b)} \quad (2)$$

In the SACP mode, Figure 2.15(b), a , b , and f do not change. Because of the change in current in the intermediate lens, the image of the aperture is formed at infinity, i.e., the crossover is at the focal point of the objective lens. By similar triangles

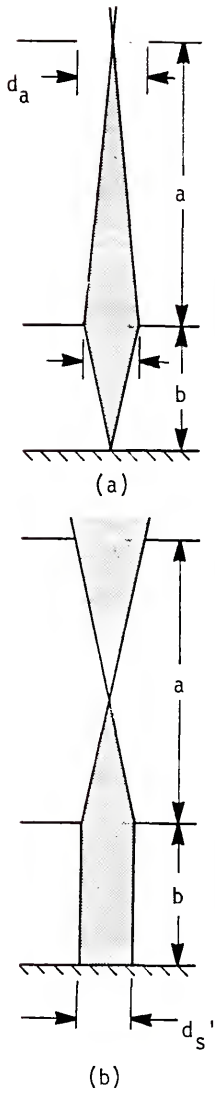


Figure 2.14 Comparison of SACP and SAI modes of operation. (a) SAI mode, (b) SACP mode. f = focal length of objective lens, d_s = diameter of area scanned on the specimen surface in the SAI mode.

$$\frac{d_s'}{d_a} = \frac{f}{a - f} = \frac{1}{\frac{q}{f} - 1}$$

where d_s' = final beam diameter in the SACP. Substituting equation (2)

$$\frac{d_s'}{d_a} = \frac{1}{\frac{a(a+b)}{ab} - 1} = \frac{1}{\frac{a+b}{b} - 1} = \frac{1}{\frac{q}{b}} = \frac{b}{q}$$

This is the identical result obtained for d_s/d_a in equation (1). Thus, $d_s = d_s'$.

2.3.6. Large Area Channeling Patterns

At times it is desirable to scan finite areas in the channeling mode, for example, to distinguish individual grains in polycrystalline samples. This can be accomplished in two ways, overfocus or underfocus as shown in Figure 2.15. These conditions can be obtained by increasing or decreasing the condenser lens current, but this also requires an increase or decrease in the correction for spherical aberration and, if the intermediate lens is not reset, the focal point of the objective lens will no longer be at beam crossover, and thus the divergence of the beam increases. Also, to return to the image mode, the objective lens must again be reset.

A simpler way of obtaining the same result is to mechanically raise or lower the specimen stage. The optics of the machine are unaltered, and the stage must only be returned to its original position in the image mode.

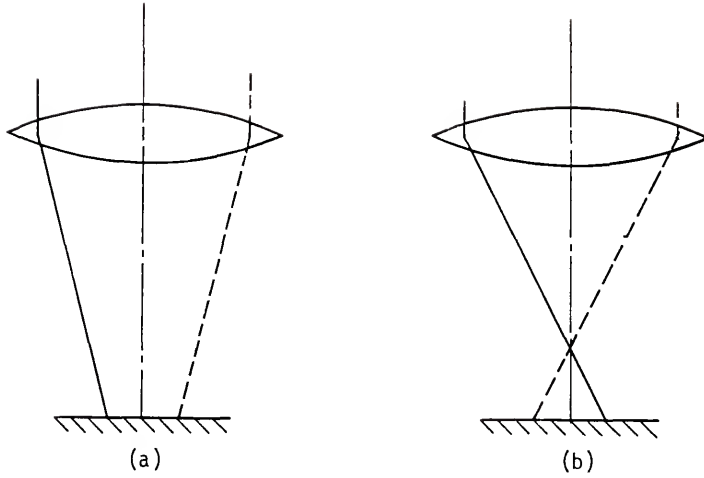


Figure 2.15 Methods of obtaining large area electron channeling patterns. (a) underfocus, (b) overfocus.

2.4 Procedures for Machine Adjustment and Alignment

2.4.1. Electron Gun and Condenser Lens Alignment

During different modes of operation the current in the intermediate lens changes. It is necessary to insure that the axis along which this lens focuses is along the optical axis of the machine. The procedure is initiated by placing the machine in the Image Mode and centering a 100 μm objective aperture. The aperture is centered by observing the location of the center of rotation of the image when the objective lens current is varied. The position of the aperture is mechanically adjusted until the center of image rotation coincides with the center of the screen. This aligns the intermediate lens with the objective lens and aperture.

Next the electron gun and condenser lens must be aligned. This is done by setting the current for the intermediate lens arbitrarily high in the image SAI Mode and arbitrarily low in the SACP Mode. The condenser lens current is decreased until a minimum-sized image circle is produced on the screen. This corresponds to the crossover being imaged on the objective aperture plane. Since the image is much larger than the aperture, a beam of electrons the size of the aperture strikes the sample when a part of the image is over the aperture, as shown in Figure 2.16. When electrons strike the sample, a signal is produced and is recorded as a bright point on the CRT display. If the size of the objective aperture were increased, the resolution of the image would decrease. Obviously, when the beam is not striking the aperture, no signal is produced and records on the image as a dark point.

The current to the filament in the electron gun is carefully decreased until a filament image, consisting of a ring surrounding

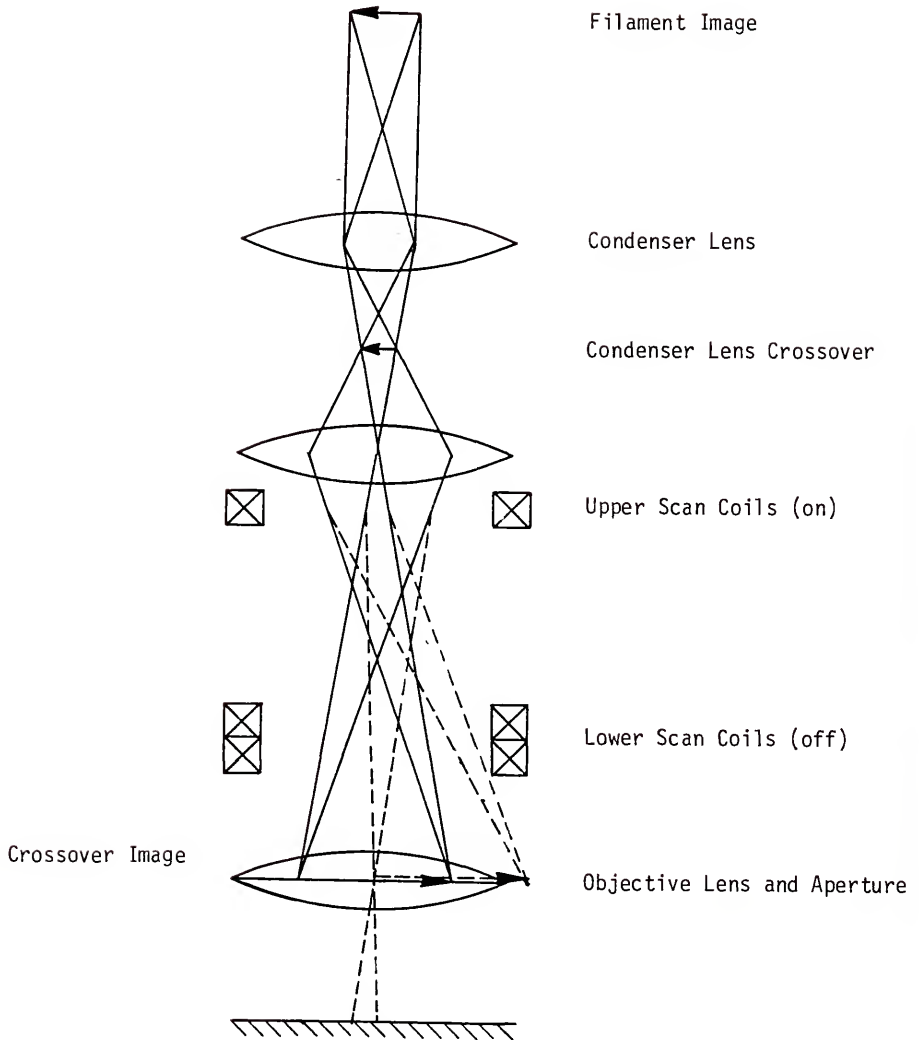


Figure 2.16 Ray diagram for filament image formation for machine alignment. Dashed lines indicate beam at maximum scan.

a bright central spot, is produced. Although the electron gun is mechanically fixed in position, it can be effectively tilted or translated electronically in two orthogonal directions (see Figure 2.8). The tilt knobs are used to center the spot of the filament image on the inside of the ring, and the translation knobs used to center the combined image on the CRT screen. This permits accurate location of the center of the filament.

The condenser lens current is increased slightly and the machine switched to the SACP Mode, which decreases the current to the intermediate lens. The intermediate lens current is then adjusted slightly to produce a minimum-sized image. The increasing of the focal length of the intermediate lens reduces the size of the image until it is much smaller than the 100 μm objective aperture. Thus, as the beam is scanned back and forth across the aperture plane, the image of the aperture is formed on the specimen, as shown in Figure 2.17. This is the same method used to form the image in the SAI Mode (see section 2.3.5) but differs substantially from the formation of the filament image.

The condenser lens can be mechanically shifted in two orthogonal directions and is used to center the aperture image on the screen. Shifting the condenser lens also shifts the ring pattern obtained in the SAI Mode at the shorter focal length setting on the intermediate lens. Thus, an iteration must be performed until the ring image and the aperture image are centered on the same point on the CRT. Before continuing, the filament must be re-saturated.

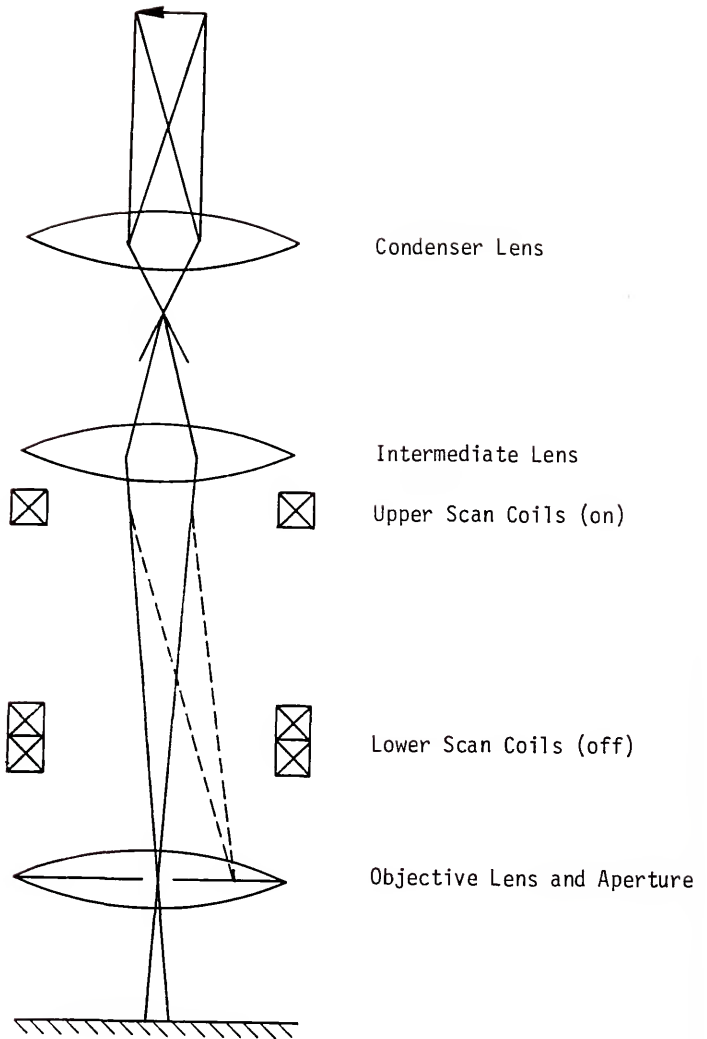


Figure 2.17 Ray diagram for formation of objective aperture image. Dashed lines indicate maximum scan position.

2.4.2. The Image and SAI Modes

A 240 μm objective aperture is installed and a secondary electron image obtained in the image mode. A 120 μm field-limiting aperture is installed and the mode switched to SAI. An image of the field-limiting aperture is formed on the CRT. The intermediate lens current is then adjusted to produce the sharpest aperture edge. This corresponds to beam crossover in the aperture plane, as shown in Figure 2.13. This current in the intermediate lens is dependent on the condenser lens setting, so it must be at its final adjusted value before the intermediate lens current is adjusted.

The objective lens current must be readjusted upon returning to the image mode, since the current in the intermediate lens alters the final focus of the objective lens.

An image magnification must be selected to form the image of the channeled area in the SAI mode. The current in the auxiliary scan coils must be adjusted to produce a beam deflection equivalent to the main scan coils, i.e., provide the same magnification. Since the beam deflection produced by the main scan coils varies with magnification, images of the channeled area are only accurate at one magnification. This is done by switching between Image and SAI Modes while adjusting the current to the auxiliary scan coils until the size of surface features inside the aperture image and Image Mode is the same.

2.4.3. Correction of Spherical Abberation

Spherical aberration correction is adjusted with the assistance of a 1000-mesh grid for a specimen. The grid can be conveniently attached

to the surface of a silicon wafer, which will be used in the final adjustment of beam divergence. The image formed by the grid in the channeling mode of operation will be a distorted view of the grid surface formed by beam movement resulting from the effects of spherical aberration, as shown in Figure 2.18. The spacing of the grid bars is $45\ \mu\text{m}$, the uncorrected beam covers a circle of approximately $180\ \mu\text{m}$ radius.

The magnitude and direction of the spherical aberration correction is changed until the beam pivots around a single point, indicated by a uniformly illuminated circle, as shown in Figure 2.19. A superimposed image of the beam on the grid is shown in Figure 2.20. With this coarse grid, all that can be said is that the beam moves less than $10\ \mu\text{m}$ from the center. A finer grid could produce more accurate adjustment of the spherical aberration corrections.

The correction applied for spherical aberration can change with many operating parameters. Controls on the SDC Unit allow magnification and shifting of the CRT display. Both of these will affect the spherical aberration correction. The amount of correction will decrease with increasing magnification, since increasing magnification corresponds to a decrease in the magnitude of the beam scan, thus reducing the magnitude of the correction, as shown in Figure 2.10.

Magnification and translation of the channeling pattern are used in the examination of the fine structure in pole centers described in Chapter 3. If this type of analysis is to be done on a polycrystalline sample, the spherical aberration must be readjusted by using a grid, as described above, to prevent beam wandering. If a single crystal sample is being analyzed, the increased channeled area will be of no consequence.

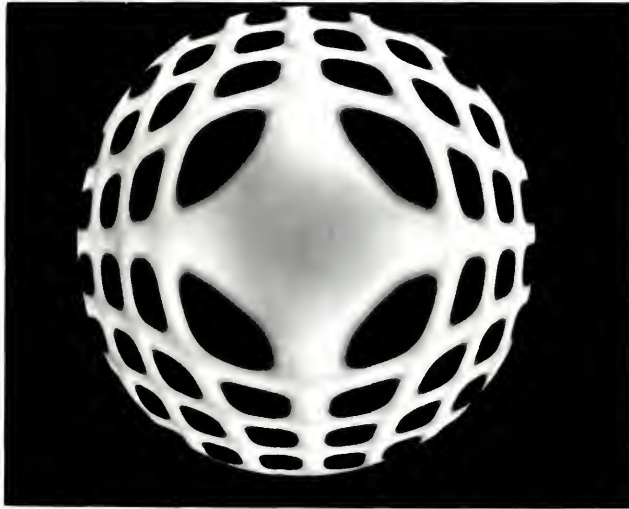


Figure 2.18 Uncorrected grid image in channeling operation.

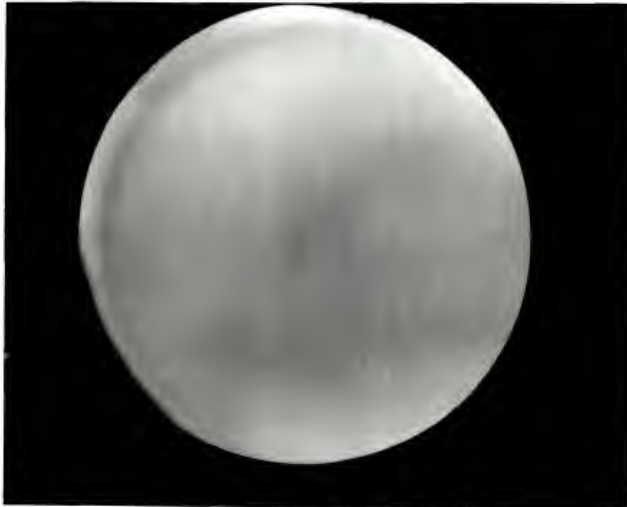


Figure 2.19 Grid image in channeling operation with dynamic correction applied.

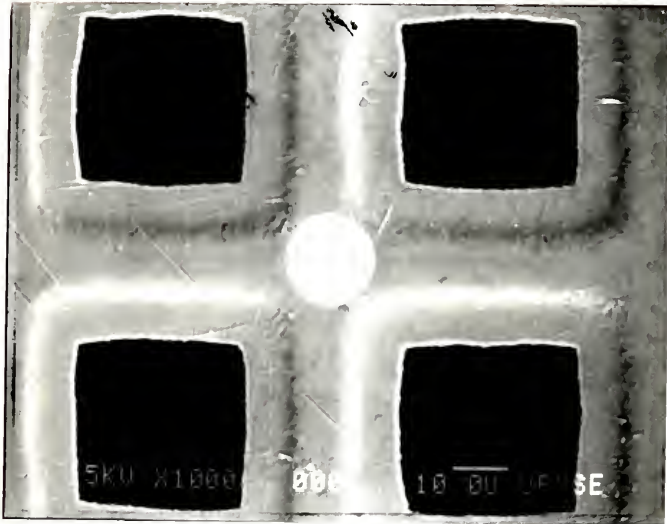


Figure 2.20 Beam image for channeling operation superimposed on conventional grid image.

2.4.4. The SACP Mode

The current in the intermediate lens in the SACP Mode can only be set by observing the quality of an electron channeling pattern of a brittle material, typically a silicon single crystal. The current in the intermediate lens is adjusted until the lines of a channeling pattern from such a material are sharpest and the greatest number of higher order lines appear. It is important to use a strong material as a specimen for making this adjustment, since a ductile material will have the higher order lines eliminated by small amounts of strain.

2.5 Additional Electronics for Electron Channeling

In order to quantitatively analyze an electron channeling pattern, such things as intensity contrast and widths of bands need to be measured accurately. Although these parameters can be measured from photographs, they can be far more accurately measured from an intensity profile across a band. Such intensity profiles can be generated in the CRT display and modified to produce a vertical deflection rather than an intensity change with changing detector signal, as shown in Figure 2.21. Quantitative information still requires measurements of distances on a photograph, and thus has limited accuracy.

Scanning electron microscopes equipped with an energy dispersive x-ray system, including a multi-channel analyzer (MCA) and mini-computer, may be modified to allow recording of intensity profiles on the MCA and storage on a floppy disc on the mini-computer. These modifications are shown schematically in Figure 2.22 and consist of the following: the

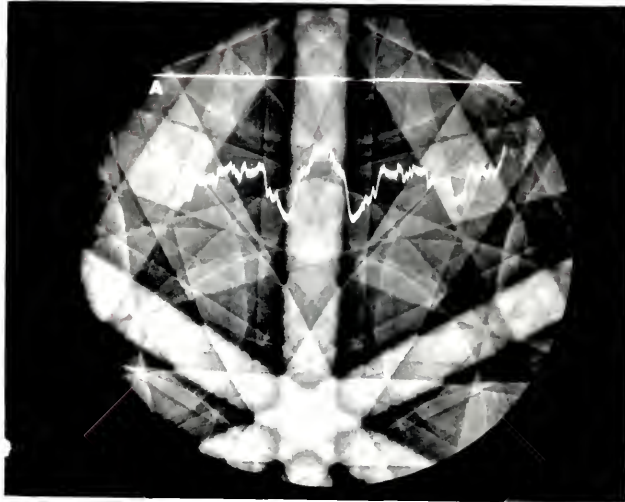


Figure 2.21 CRT intensity profile (A) for selected scan line,
(B) from electron channeling pattern.

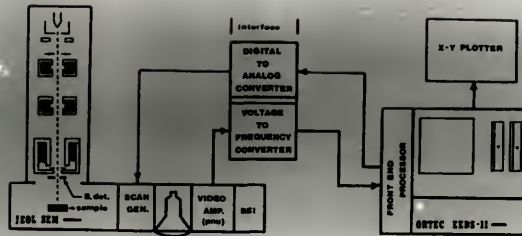


Figure 2.22 Schematic diagram for intensity profile gathering and storage on MCA.

scan generator is computer-controlled to step along a selected scan line, in 512 steps, with the length of time spent between steps controlled by a mini-computer, via a digital-to-analog converter. A typical value is 200 ms. While the beam is held on a point, the total signal produced is measured by counting the pulses on a voltage-to-frequency converter and stored in a channel on the MCA. As the beam is stepped to the next position, the MCA switches to the next channel, and the process is repeated. The result is a digital intensity profile for a slow scan of the entire scan line. This intensity profile may be subject to mathematical manipulation, such as multiplication, smoothing, black level suppression, or any user-written programs. Intensity profiles can be stored on the floppy disc for later retrieval, and hard copies can be obtained with an x-y plotter. The MCA display for the intensity profile of the scan line on the channeling pattern in Figure 2.21 is shown in Figure 2.23.

Another system for recording intensity profiles was developed by Farrow and Joy (1981). The system is similar to the one described above except the beam is scanned repeatedly and the results of several scans averaged, rather than a single slow scan.

Use of these systems is limited to intensity profiles from a scan line. Intensity profiles across a band in the channeling pattern should be along a line perpendicular to the band, thus requiring scan lines being perpendicular to the band. This can be accomplished by mechanical rotation of the sample or, in machines so equipped, electronic rotation of the scan raster. Thus, for a single channeling pattern, intensity profiles can be obtained along any direction and passing through any point.



Figure 2.23 Intensity profile from Figure 2.21 stored and displayed on MCA.

There are several forms of signal processing that can be used to improve the clarity of electron channeling patterns. The fine lines throughout the pattern and in particular near the pole centers can be enhanced by differentiating the signal (Coates, 1969). The effects of differentiation are directional in that lines perpendicular to the scan lines are largely affected while ones parallel to scan lines are unaffected.

Another system for enhancing fine lines has been developed by Vicario et al. (1970b). This system selectively subtracts a D.C. signal from bright areas of the sample. This enhances the fine structure at the pole centers.

When samples are tilted to allow observation of poles more than a few degrees from the surface normal, one edge of the pattern becomes dark and the other light due to the directional nature of the backscattered electrons. This can be compensated by adding a range signal to the intensity of a scan, as described by Morin and Vicario (1976). Using their device patterns of uniform contrast were obtained with specimen tilts of 54° .

CHAPTER 3
FINE STRUCTURE NEAR THE CENTER OF LOW INDEX
POLES IN ELECTRON CHANNELING PATTERNS

3.1 Origin of Fine Structure

Fine lines exist near the centers of low index poles in electron channeling patterns. When viewed in a normally amplified signal they are difficult to see because of their small size, low contrast, and the brightness of the immediate region. A magnified channeling pattern of the area around a (111) pole is shown in Figure 3.1, which has had its contrast adjusted to enhance the visibility of the fine lines. Alternatively, the signal may be differentiated so that only changes in signal intensity are visible, or the signal may be processed to suppress the brightness near the pole center.

Also visible on electron channeling patterns near low index poles is a variety of geometric figures, such as hyperbolas, parabolas and circles. Of greatest significance for the analysis of fine structure near the pole centers are the circles centered on the pole, shown in Figure 3.2. The analysis of the origin of these circles leads directly to the origin and geometry of the fine structure.

Although visible in Coates' early papers (Coates, 1968), fine structures were not discussed or analyzed. Vicario et al. (1971) mathematically explained the origin of the circles, along with the other geometric figures in channeling patterns. He also studied some high order planes (Vicario and Pitival, 1969). A summary of Vicario's analysis follows, and serves

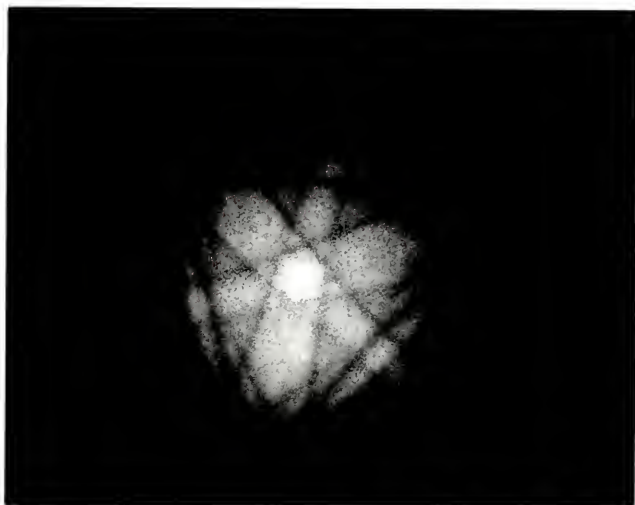


Figure 3.1 Fine structure near (111) pole at 35 kV.

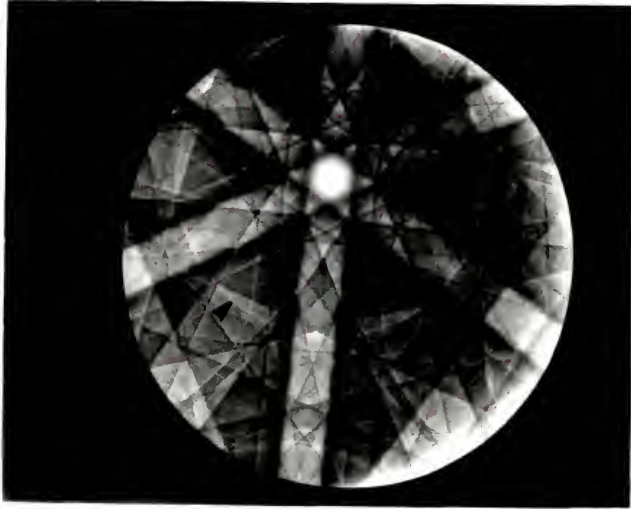


Figure 3.2 ECP for (111) silicon at 35 kV.

as a basis for the origin of the fine structure and provides data for an alternative and more convenient method of analysis.

Following Vicario, Figure 3.3 shows a typical plane in a crystalline solid making a small angle α with the [001] axis. This means that the pole of the plane will make an angle β with the [001] pole, where $\beta = 90 - \alpha$, that is very near 90° . Thus $\cos\beta$ must be small. $\cos\beta$ may be obtained by obtaining the dot product of the plane in question with [001] and dividing by the magnitude of the pole of the plane. If the plane has Miller indices (p q r),

$$\cos\beta = \frac{r}{\sqrt{p^2 + q^2 + r^2}} \quad (1)$$

Thus, the angle between planes and the [001] axis is determined by the third Miller index. If $r = 0$, the plane is perpendicular to the axis. These are planes of the [001] zone axis that form the bulk of the channeling pattern. If $r = 1$, the planes will not be perpendicular to the axis but will always make a small angle. Thus, the planes in which we are interested have the form (p q 1).

In a channeling pattern of sufficient angular width, the plane [pq1] will form a band with edges at $(\alpha + \theta_B)$ and $(\alpha - \theta_B)$, where θ_B is the Bragg angle, shown in Figure 3.3 as points B and B'. The location of these band edges can be calculated:

$$\sin\alpha = \cos\beta = \frac{1}{\sqrt{p^2 + q^2 + 1}} \quad (2)$$

$$\sin\theta_B = \frac{\lambda}{2d_0} \sqrt{p^2 + q^2 + 1} \quad (3)$$

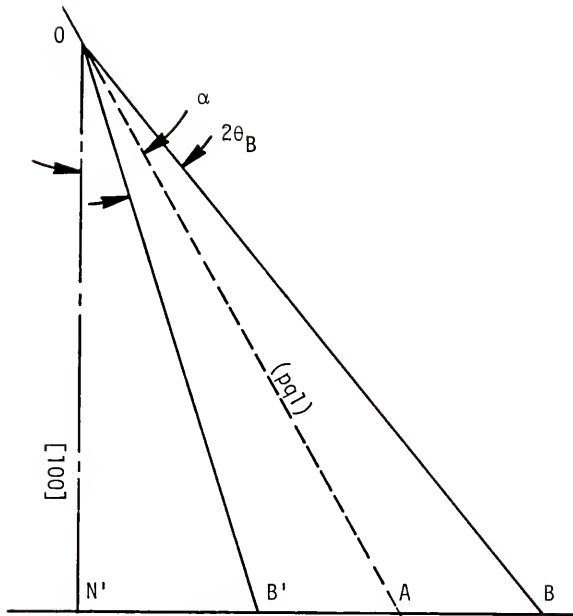


Figure 3.3 Geometry of channeling patterns from Vicario et al. (1971).

$$\lambda = \sqrt{\frac{150}{V}} \quad (4)$$

where: λ = the wavelength of electrons in the primary beam, in Angstroms

V = primary beam potential, in volts

d_0 = lattice parameter for the material being examined

For any material and accelerating potential, α and θ_B may be calculated and plotted as a function of $(p^2 + q^2 + 1)$. This is done for silicon at 30 kV in Figure 3.4, along with the location of one band edge ($\alpha + \theta_B$). For $100 < (p^2 + q^2 + 1) < 200$, $(\alpha + \theta_B)$ changes very little. Thus, several groups of planes have one band edge in a very small angular range, i.e., the point B' in Figure 3.3 is almost fixed. For any value of $(p^2 + q^2 + 1)$, there exist several planes distributed rotationally around the [001] axis. These planes form a circle of radius $(\alpha + \theta_B)$.

Further mathematical analysis shows that the minimum in the plot of $(\alpha + \theta_B)$ versus $(p^2 + q^2 + 1)$ occurs at $\alpha = \theta_B$. As an example, for the [001] axis of silicon at 30 kV, 60 planes make up the circle.

The existence of the fine structure follows directly from the existence of the circle. If $\alpha \cong \theta_B$ and $(\alpha + \theta_B)$ forms the circle, then the other edge of the band, located at $(\alpha - \theta_B)$, is very close to the center of the circle, in this case the [001] axis. Since α and θ_B vary substantially, and $(\alpha + \theta_B)$ is constant, $(\alpha - \theta_B)$ varies significantly and thus fewer planes are visible in the center than on the circumference of the circle.

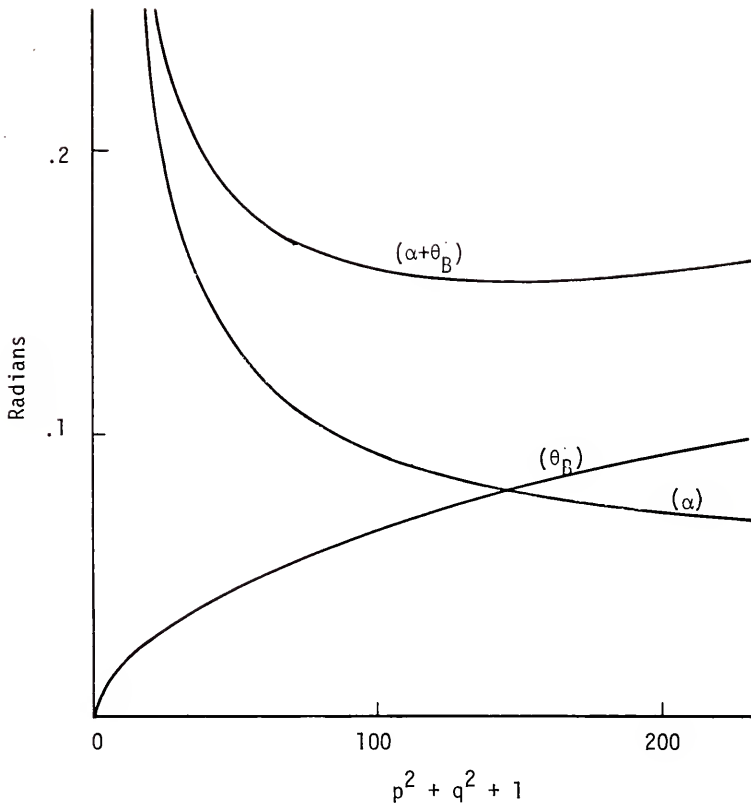


Figure 3.4 From Vicario et al. (1971).

Using this technique, further determination of the geometry of the fine structure is somewhat tedious, involving a series of angles determined by dot products with major planes (i.e., (220)).

3.2 Application of the Reciprocal Lattice-Ewald Sphere Construction to the Fine Structure in Electron Channeling Patterns

The reciprocal lattice-Ewald sphere construction has been used to predict diffraction patterns for electrons and x-rays. It consists of the construction of a reciprocal lattice in which diffracting planes that exist in the crystal structure in real space are represented by points whose distance from the origin of reciprocal space is the reciprocal of their plane spacing. Also, a line connecting the point in reciprocal space and the origin is perpendicular to the planes the point represents. The reciprocal lattice consists of a regular periodic array of points, much like the atoms of the crystals do in real space.

An Ewald sphere with radius $1/\lambda$ is then drawn tangent to the origin of reciprocal space with the radius at the point of tangency lying along the beam direction. The geometry of this construction, to be discussed in more detail shortly, is such that points in reciprocal space that are intercepted by the Ewald sphere satisfy the Bragg condition, i.e., diffraction occurs.

The fine structure at the center of electron channeling patterns of low index poles and the circles centered on these poles can be explained in terms of this same construction. Although electron channeling is not electron diffraction in the strict sense, large changes in the intensity of channeling patterns do occur near the Bragg condition.

Looking more closely at the geometry of the reciprocal lattice, only those planes which diffract exist in reciprocal space, and not all planes diffract with equal intensity. Thus, for non-primitive unit cells, all planes in real space do not exist in reciprocal space. For cubic crystals of high symmetry for elements, all points in reciprocal space diffract with equal intensity, but for lower symmetry crystal structures or for compounds consisting of two or more atomic types, the number and intensity of points in reciprocal space will vary.

Fortunately, the intensity of diffraction from points in reciprocal space can be modeled mathematically. This results in a quantity known as the structure factor. To exist in reciprocal space a plane must have a non-zero structure factor, and the intensity of the diffracted beam is proportional to the square of the structure factor. The structure factor is a complex number.

Restricting ourselves to pure elements, structure factor calculations for a face-centered cubic (fcc) crystal allows points in reciprocal space only if the Miller indices of the planes are either all odd or all even. This gives a body-centered cubic structure in reciprocal space, as shown in Figure 3.5.

The diamond cubic structure of silicon, with its lower symmetry, has the same points in reciprocal space as the fcc structure, but some points have much lower intensity, also shown in Figure 3.5. Some texts ignore the weaker points (Cullity, 1978) but Hirsch et al. (1977) state that parallel planes in reciprocal space must be identical, a condition which is not satisfied by omitting these weaker diffracting points.

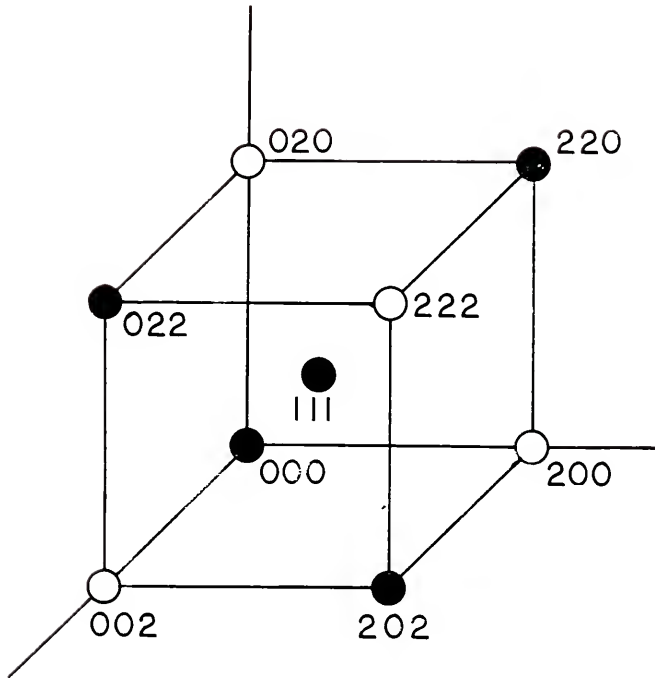


Figure 3.5 Diamond cubic and face centered cubic structure in reciprocal space. For face centered cubic, all points are of equal intensity. For diamond cubic, open points have very low intensity.

Planes of a zone can be drawn directly from the geometry of the "unit cell" of reciprocal space or can be deduced mathematically from the structure factor and the fact that the dot product of planes of a zone and the zone axis must be zero. All planes of a zone lie in the plane of reciprocal space containing the origin, but parallel planes may be constructed using basic geometry. The mathematical approach is often quicker and more convenient, especially in the case of higher order zone axes. We will now examine the geometry of points in parallel planes of reciprocal space, following Hirsch et al. (1977).

Parallel planes of reciprocal space are called Laue zones. The plane containing the origin is called the zero order Laue zone. Approaching the center of the Ewald sphere you encounter the first Laue zone, second Laue zone, etc. For a zone axis (uvw) and a point $(hk\ell)$ lying in reciprocal space, the order of the Laue zone may be determined by the relationship $hu + kv + \ell w = N$, where the value of N determines the Laue zone in which the point lies. N has a regular sequence of values, determined by the structure factor and found by inspection. For the zero order Laue zone, $N = 0$. This is consistent with the zone axis and planes of the zone being perpendicular, i.e., the dot product equals zero. If the crystal structure is fcc and $(uvw) = (211)$, points such as $(02\bar{2})$ would be in the zero order zone. If the first order zone corresponded to $N = 1$, points such as $(11\bar{2})$ would be included, and this point, being of mixed odd and even indices, is not allowed by the structure factor. Planes of the type $(22\bar{4})$ are allowed, and thus $N = 0, 2, 4, 6\dots$ For the (111) axis in fcc, $N = 0, 1, 2, 3\dots$

The zero order Laue zone may be plotted graphically by determining the angles between points in the zone, i.e., points for which $N = 0$, by

dot products and remembering that the distance from the origin is the reciprocal of the plane spacing in real space. Plots of the zero order zones for axes of low indices are available for most crystal structures (Eddington, 1975).

The higher order Laue zones are plotted as projections on the zero order zone. Since parallel planes have identical arrays of points, the higher order zones may be plotted by knowing the projection of a single point on the zero order zone. Looking at Figure 3.6, (uvw) is the zone axis, (hkl) is a point in the N^{th} order Laue zone, the intersection of the N^{th} order Laue zone with the zone axis is at a point $P = c(uvw)$, where c is a constant. Since point P lies in the N^{th} order plane,

$$cu^2 + cv^2 + cw^2 = N$$

or

$$c = \frac{N}{u^2 + v^2 + w^2}$$

and thus vector $OP = \frac{N(uvw)}{u^2 + v^2 + w^2}$. Vector OP must be subtracted from point (hkl) to get Q , the projection of (hkl) on the zero order plane. Thus, the point Q is at $(h - cu, k - cv, l - cw)$.

As an example, the (001) zone axis in reciprocal space is plotted in Figure 3.7. The points in the zero order zone must have their l index 0, i.e., be of the type $(hk0)$. Since zero is an even number, the remaining two indices must also be even. Thus, the planes (200) , (020) and their negatives are all in the zero order zone, as shown in Figure 3.7. The first order zone corresponds to $N = 1$, and planes of the first order zone are of the type (hkl) . Arbitrarily choosing the (111) plane:

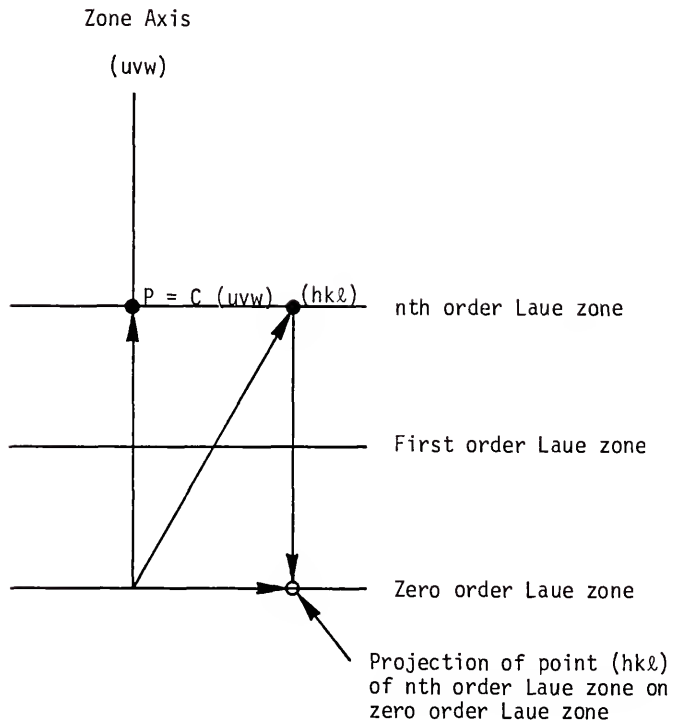


Figure 3.6 Geometry of Laue zones in reciprocal space.

$c = 1$, and the projection of (111) on the zero order zone is at (110) or $1/2(220)$. The remaining points can then be plotted.

The Ewald sphere is constructed tangent to the origin with radius $1/\lambda$. The geometry of the Ewald sphere-reciprocal lattice construction is shown in Figure 3.8. Note that for a point in reciprocal space intersected by the Ewald sphere,

$$\sin\theta_B = \frac{1/d}{2/\lambda} = \frac{\lambda}{2d}$$

or

$$\lambda = 2d \sin\theta_B.$$

Thus, the point satisfies the Bragg condition, and diffraction occurs.

Points in reciprocal space have a finite size due to thermal vibrations of atoms and specimen thickness effects. Thus, several points in the zero order zone are intersected by the Ewald sphere. The number of points intersected depends on the radius of the Ewald sphere, which in turn depends on the primary beam energy. Thus, for higher energy electrons (100-200 kV), such as are commonly used in the transmission electron microscope, the diffraction pattern contains many points from the first order zone. Diffraction patterns at lower accelerating potentials will contain correspondingly fewer points.

The Ewald sphere construction may now be used to predict the geometry of the fine structure at the center of electron channeling patterns. Using the criteria for obtaining fine structure (and of circles), $\alpha = \theta_B$, is only satisfied by points in the first order Laue zone, since all points in the zero order zone represent planes that are parallel to the axis. Returning to Figure 3.8, the triangle formed by the origin of reciprocal space, the

center of the Ewald sphere, and a diffracting point is isocetes with a vertex angle of $2\theta_B$. The planes corresponding to the diffracting point are perpendicular to the base and thus bisect the angle of the vertex. Since one side of this triangle is the zone axis, half the vertex angle is also the angle the plane makes with the pole, α , and thus $\alpha = \theta_B$. Any point along the circle formed by the intersection of the Ewald sphere and the first order Laue zone satisfies the requirement for the formation of a circle in an electron channeling pattern, and the circle formed on the pattern has the same angular diameter as the circle formed by the intersection described above.

Figure 3.7 shows the first order Laue zone for an [001] axis in silicon. Points that contribute to the circle as determined by Vicario et al. are given in Table 3.1 and plotted in Figure 3.7 as open squares. From Figure 3.8, the radius of the circle formed by the intersection of the Ewald sphere and the first order Laue zone can be calculated.

$$R = \sqrt{\frac{2h}{\lambda} - h^2}$$

$$h = \frac{1}{d_0 \sqrt{u^2 + v^2 + w^2}}$$

where R = radius of the circle of intersection

h = separation of planes in reciprocal space

u, v, w = Miller indices of the pole ([001])

d_0 = lattice constant of material (5.409 Å for Si).

Once the radius is known, the corresponding value of $(h^2 + k^2 + l^2)$ can also be calculated:

$$\frac{1}{d^2} = h^2 + R^2$$

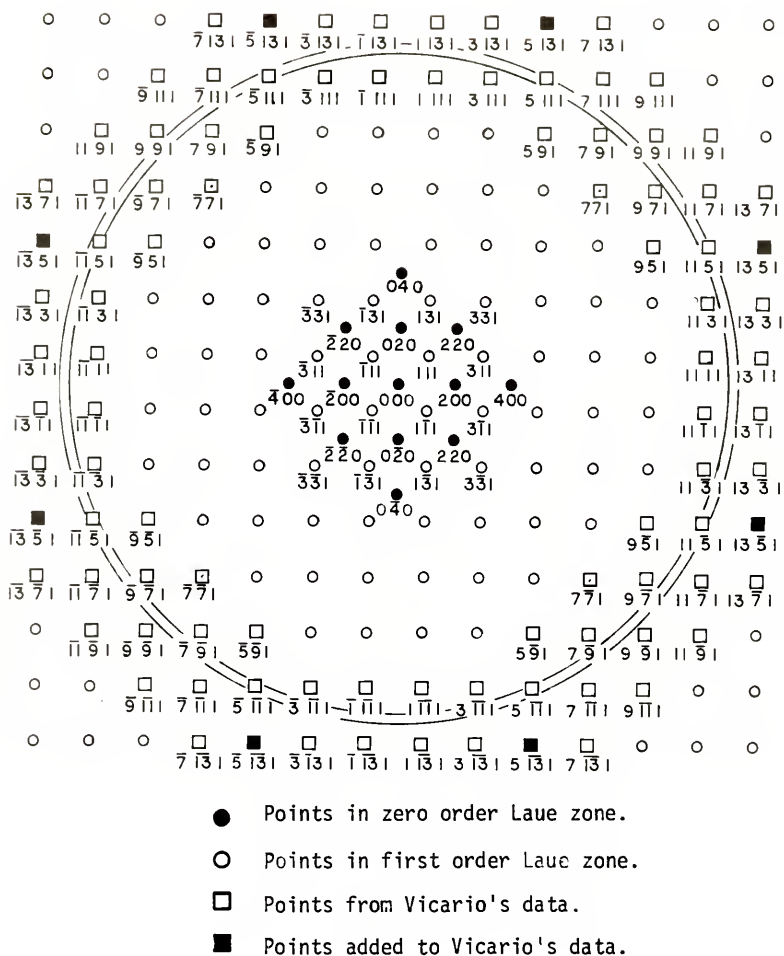


Figure 3.7 First order Laue zone for (100) silicon. Circles are the intersection of the first order zone with the Ewald sphere at 30 kV (smaller circle) and 35 kV (larger circle).

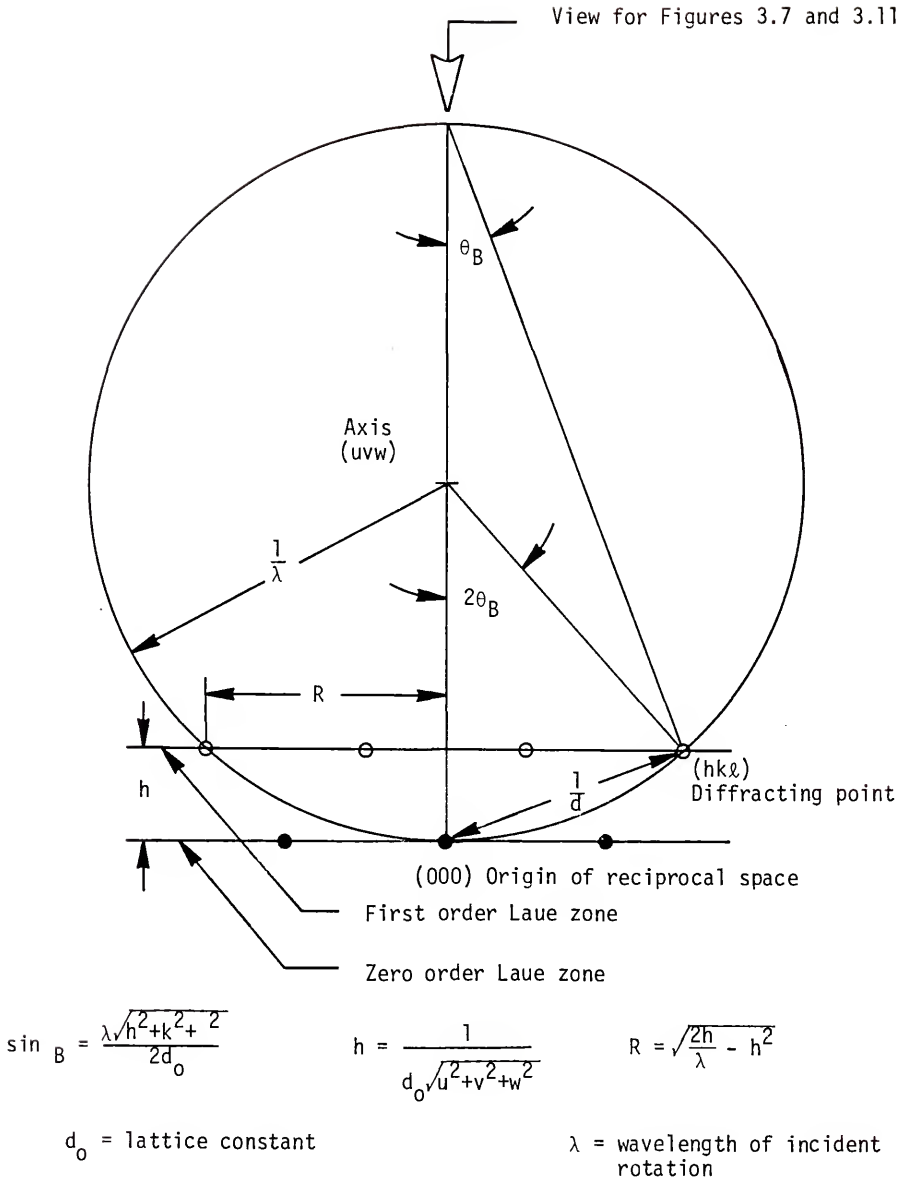


Figure 3.8 Ewald sphere-reciprocal lattice construction.

TABLE 3.1
 PLANES CONTRIBUTING TO THE FORMATION OF CIRCLES
 (Vicario et al., 1971)

Indices	$h^2+k^2+l^2$	$\theta_B(^{\circ})$	$\alpha(^{\circ})$	$(\alpha+\theta_B)$	$(\alpha-\theta_B)$	# of planes
7 7 1	99	3.7443	5.7682	9.5125	2.0239	4
9 5 1	107	3.8919	5.5477	9.4396	1.6558	8
11 1 1	123	4.1724	5.1732	9.3456	1.0008	8
9 7 1	131	4.3078	5.0123	9.3201	.7045	8
11 3 1	131	4.3078	5.0123	9.3201	.7045	8
11 5 1	147	4.5641	4.7321	9.2962	.1680	8
9 9 1	163	4.7509	4.5450	9.2459	-.2054	4
11 7 1	171	4.4234	4.3857	9.3091	-.5377	8
13 1 1	171	4.4234	4.3857	9.3041	-.5377	8
13 3 1	179	5.0376	4.2865	9.3242	-.7511	8
11 9 1	203	5.3656	4.0247	9.3903	-1.3409	8
13 7 1	219	5.5737	3.8747	7.4484	-1.6990	8
*13 5 1	195	5.2370	4.1066	9.3443	-1.1311	8

* point added to Vicario's data

$$\frac{1}{d^2} = \frac{(h^2 + k^2 + \ell^2)}{d_0^2}$$

$$(h^2 + k^2 + \ell^2) = d_0^2 \left(\frac{1}{d}\right)^2$$

$$(h^2 + k^2 + \ell^2) = d_0^2 (h^2 + k^2)$$

where d = the plane spacing

Vicario's experimental conditions give the following results:

$$\lambda = 7.0711 \times 10^{-2} \text{ \AA}^{-1}$$

$$h = .1849 \text{ \AA}^{-1}$$

$$R = 2.2892 \text{ \AA}^{-1}$$

$$(h^2 + k^2 + \ell^2) = 152.98$$

In Table 3.1, the value of $(\alpha - \theta)$ passes through zero between $(h^2 + k^2 + \ell^2) = 147$ and $(h^2 + k^2 + \ell^2) = 163$. The circle corresponding to $(h^2 + k^2 + \ell^2) = 152.98$ has been drawn in Figure 3.7. Points lying near this circle here $\alpha \approx \theta_B$, and those having $(\alpha - \theta_B) < \sim 1^\circ$ will have one edge of their band visible as fine structure at the pole center. Of the planes listed in Table 3.1, seven groups consisting of 52 planes will have structure in the center.

The center structure may be plotted directly on top of the first order Laue zone. An arbitrary angular scale is selected, centered on (000). For a given group of planes, a circle of radius $(\alpha - \theta_B)$ is drawn. All planes in this family must be tangent to this circle and perpendicular to a line connecting the origin and the point representing the plane. If $(\alpha - \theta_B)$ is > 0 , the tangent is drawn on the same side as the point. If $(\alpha - \theta_B) < 0$, the line is drawn on the opposite side. The first and zero order zones do not lie in the same plane, and thus the line connecting the origin and the point representing the

plane is not in the plane of the paper used for the construction, the points are far enough from the center that the error involved is small. This procedure is repeated for all values of $(\alpha - \theta_B)$ until all planes have been drawn.

Data at 35 kV for the (001) pole are shown in Figure 3.9. Figure 3.7 has the circle of intersection for 35 kV also drawn. Its radius corresponds to $(h^2 + k^2 + l^2) = 165.27$. Although the radius has changed little from the 30 kV accelerating potential, the values of θ_B have changed enough to cause a noticeable change in the fine structure. Since the distance between points in reciprocal space depends only on the crystal structure and lattice constant of the material, values for α do not change with accelerating potential.

Points producing fine structure at 35 kV in an [001] crystal of silicon are given in Table 3.2. The plotted fine structure is shown in Figure 3.10. The 44 planes are within 1° of the [001] pole; thus, the intricate structure. Not all of the lines have the same intensity. Calculation of the intensity of zero order Laue zone lines in an ECP from theory is only semi-quantitative, and the calculations are involved and laborious. Intensities of lines lying in the first order zone are another step beyond, and were not attempted.

The graphical method of determining fine structure has the advantage that once the geometry of the first order zone has been determined, the Miller indices of the planes which approximate the $\alpha \approx \theta_B$ condition, i.e., those which lie close to the circle formed by the intersection of the Ewald sphere and the first order zone, is obvious. A strictly mathematical analysis gives only the values of $(h^2 + k^2 + l^2)$. It is tedious to determine, for example, that $(h^2 + k^2 + l^2) = 195$ is a plane of type $\{13\ 5\ 1\}$, especially when not all values of $(h^2 + k^2 + l^2)$ have integer indices for

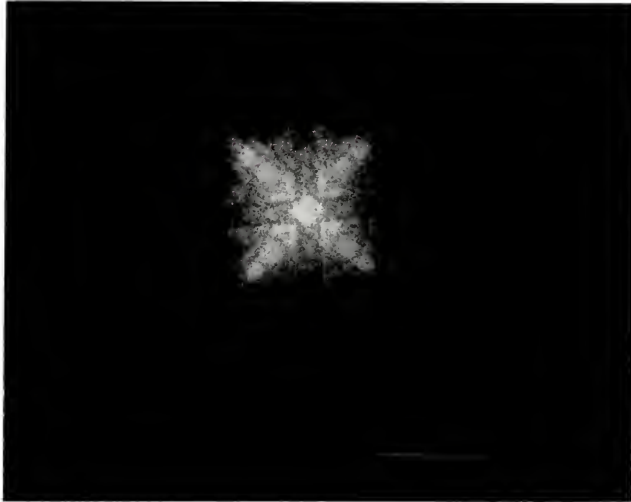
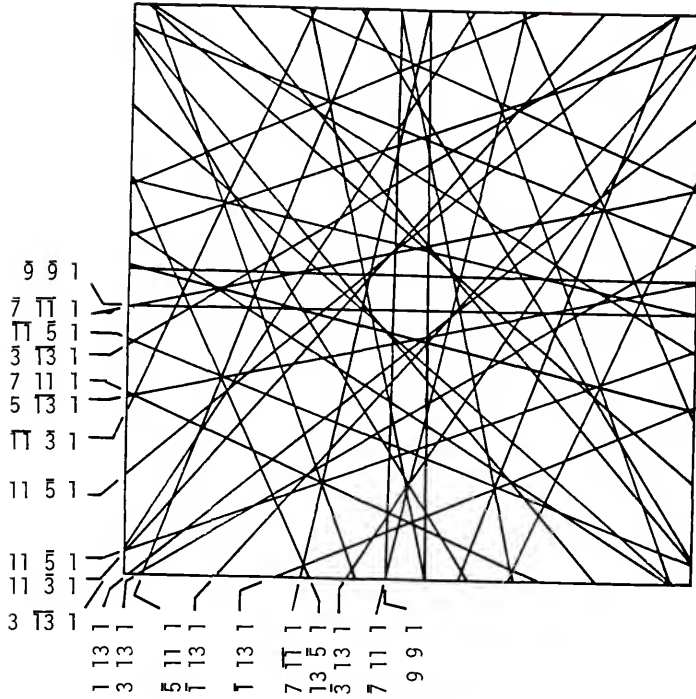


Figure 3.9 Fine structure near the (001) pole at 35 kV.

TABLE 3.2
 PLANES IN THE FINE STRUCTURE AROUND THE
 [001] AXIS OF SILICON AT 35 kV

Indices	$h^2+k^2+l^2$	$\theta_B(^{\circ})$	$\alpha(^{\circ})$	$(\alpha-\theta_B)$	# of Planes
11 5 1	147	4.2076	4.7311	.741	8
9 9 1	163	4.4311	4.4924	.061	4
11 7 1	171	4.5388	4.3858	-.153	8
13 1 1	171	4.5388	4.3858	-.153	8
13 3 1	179	4.6439	4.2865	-.357	8
13 5 1	195	4.8475	4.1066	-.741	8



8 {11 5 1} planes

8 {13 1 1} planes

4 {9 9 1} planes

8 {13 3 1} planes

8 {11 7 1} planes

8 {13 5 1} planes

Figure 3.10 Calculated fine structure near the (100) pole of silicon at 35 kV.

h , k and l , and that even when integer values do exist, they may be excluded by the structure factor. Plotting of Vicario's data reveals that planes of type $\{13\ 5\ 1\}$ have been omitted. They have been added to Table 3.1 and Figure 3.7.

The analysis of the $[001]$ pole is simplified by the fact that membership in the first order zone is relatively easily determined, i.e., the last index must be one, the other two must be odd. For higher index poles it is not as obvious.

As a second example, the $[111]$ pole of silicon will be analyzed. The large angle ECP is shown in Figure 3.2 and the fine structure in Figure 3.1. By measuring the width (in centimeters) of the 220 type bands in Figure 3.2, calculating the Bragg angle for a $\{220\}$ plane and remembering that the width of a band in an ECP is $2\theta_B$, a conversion factor from cm to degrees can be determined. The radius of the circle centered on the pole may then be measured.

$$\theta_B \{220\} = .98^\circ$$

$$\text{width of } \{220\} \text{ planes} = .82 \text{ cm}$$

$$1 \text{ cm} = 2.39^\circ$$

$$\text{Average diameter of circle} = 5.7 \text{ cm}$$

$$\text{radius of circle} = 6.8^\circ$$

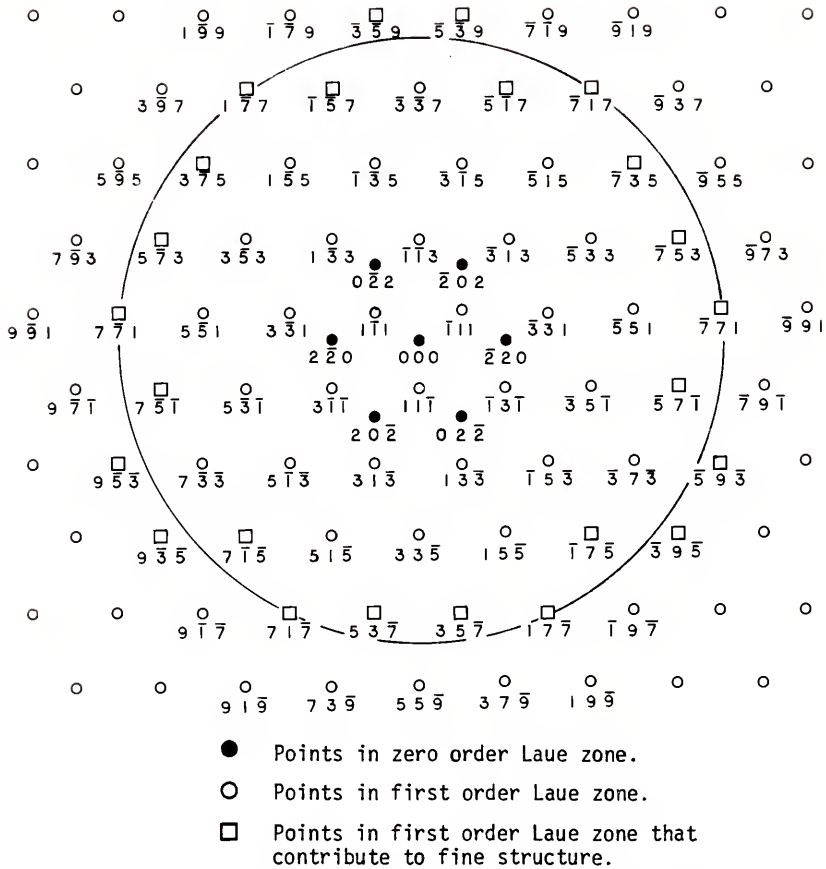
The first order Laue zone for the $[111]$ pole may be drawn as described previously. The result is shown in Figure 3.11. Calculations give the following values:

$$\lambda = 6.5465 \times 10^{-2} \text{ \AA}^{-1}$$

$$h = .10674 \text{ \AA}^{-1}$$

$$k = 1.8027 \text{ \AA}^{-1}$$

$$h^2 + k^2 + l^2 = 95.4$$



To calculate the radius of the circle of intersection, we must first note that its radius is $2\theta_B$ (Figure 3.8).

$$\sin 2\theta_B = \frac{R}{1/\lambda} = R\lambda$$

$$2\theta_B = 6.78^\circ$$

This is in very good agreement with the experimentally determined value.

Table 3.3 lists the planes forming the fine structure. Only planes of the form $h + k + l = 1$ appear. Thus, for the family of planes {375}, only (375), (735), (357), (573), (537) and (753) appear. There are only 24 planes within 1° of the center as opposed to 44 planes for the [001] axis at the same beam energy. This is due to the lower density of points in reciprocal space and the lower symmetry (three-fold) of the [111] pole compared to the [001] (four-fold). The planes are plotted in Figure 3.12.

The effect of a change in accelerating potential on the overall channeling pattern is basically one of magnification due to changes in θ_B . The fine structure should change in geometry rather than in size. Since crystal lattice parameters are known to several significant figures from x-ray diffraction, the geometry of the fine structure could be used to calculate accurate values of accelerating potential. As an example, Figure 3.13 shows the entire channeling pattern and the fine structure for the (111) pole at 30 kV. This compares with Figures 3.1 and 3.2. The ECP changes very little, but the fine structure changes noticeably.

TABLE 3.3
 PLANES IN THE FINE STRUCTURE AROUND THE [111] POLE IN SILICON AT 35 kV

Indices*	$h^2+k^2+l^2$	$\theta_B(^{\circ})$	$\alpha(^{\circ})$	$(\alpha-\theta_B)$	# of Planes
751	75	3.0004	3.8226	.878	6
375	83	3.1604	3.6334	.472	6
177	99	3.4520	3.3265	-.125	6
359	115	3.7208	3.0862	-.634	6

* only planes of the form $h + k + l = 1$ appear

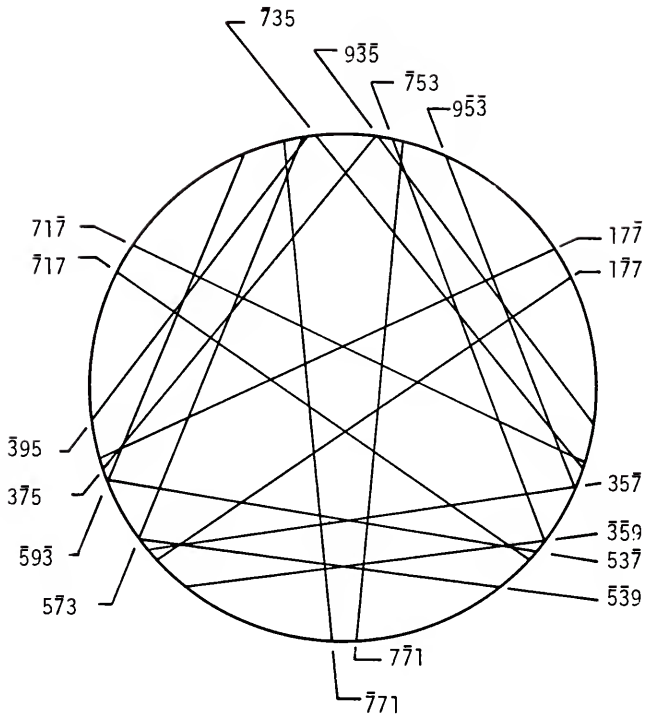
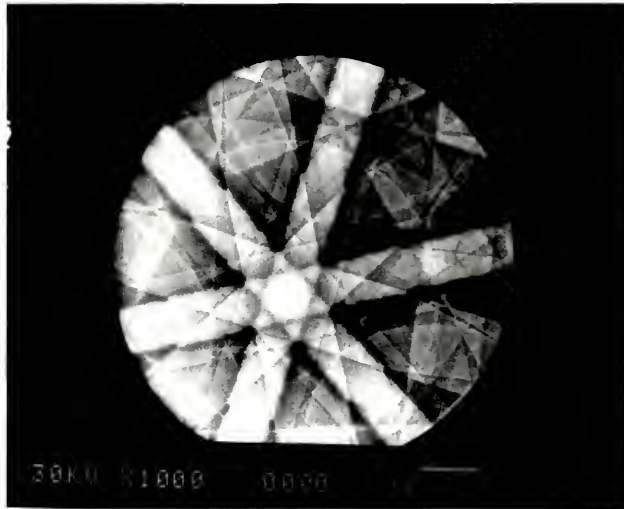
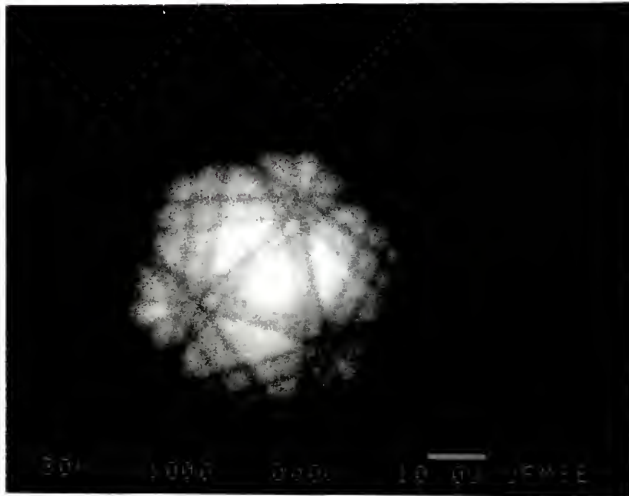


Figure 3.12 Calculated fine structure for (111) silicon at 35 kV.



(a)



(b)

Figure 3.13 ECP (a) and fine structure (b) of the 111 pole at 30 kV.

3.3 Changes to Fine Structure During Elastic Strain

The geometry of the fine structure near pole centers is dependent on α and θ_B over the 10μ area from which channeling patterns are being obtained. Elastic strain causes uniform long-range changes in the distances between atoms which then change α and θ_B , and thus the geometry of the fine structure. Plastic flow, which is characterized by dislocations and local, non-uniform changes in the distances between the atoms, should perhaps cause a decrease in contrast due to lattice disarray, but no changes in geometry. The disappearance of fine lines at high levels of plastic strain has been reported by Schulson et al. (1969).

Although the analysis of the effects of strain on fine structure could be performed on any pole, it is simplified by selecting a pole with relatively few lines, i.e., the (111) pole in the case of silicon, and is further simplified by looking only at a limited number of lines. In the fine structure of the (111) pole shown in Figure 3.12, the $35\bar{7}$, $\bar{7}35$ and $5\bar{7}3$ lines were analyzed. These lines form a triangle.

The effects of strain can be qualitatively assessed as follows: Compressive strain causes a decrease in lattice spacing (d) along the strain axis. From the Bragg equation, $\lambda = 2d\sin\theta_B$, a decrease in d means an increase in θ_B . Looking at Figure 3.6, a decrease in d means an increase in $1/d$. Since α is the angle between a line perpendicular to $1/d$ and the major pole, an increase in $1/d$ results in a decrease in α . The difference $(\alpha - \theta_B)$ must decrease. Thus, for a compressive strain, the line in the fine structure would move closer to the pole.

Of course, a compressive strain also causes an increase in d spacing in directions orthogonal to the strain directions due to the Poisson effect,

and this would shift lines away from the pole. To assess the changes in the fine structure, the location of a point in reciprocal space must be resolved into components along the coordinate axes based on the direction of the applied strain. The case of a (111) crystal strained in the $[02\bar{2}]$ direction is shown in Figure 3.14. The important components are a, e and f, since these lie along the coordinate axes. The magnitude of these components can be determined by the following equations:

$$b = \frac{a_0}{\sqrt{h^2+k^2+l^2}} \quad \gamma = \text{angle between } (hkl) \text{ and } (02\bar{2})$$

$$a = \frac{1}{a_0 \sqrt{u^2+v^2+w^2}} \quad \cos \gamma = \frac{2k-2}{\sqrt{h^2+k^2+l^2} \sqrt{8}}$$

$$c = \sqrt{b^2 - a^2} \quad g = b \sin \gamma$$

$$\sin \alpha = \frac{a}{b} \quad e = b \cos \gamma$$

$$f = \sqrt{g^2 - a^2}$$

The results for the $35\bar{7}$, $\bar{7}35$ and $5\bar{7}3$ planes at 35 kV are given in Table 3.4.

Refer. to Figure 3.14 and 3.15. If a compressive strain is applied along the X axis, remembering that we are dealing with reciprocal space, and assume a value of Poisson's ratio for (111) silicon of .342 (Rungan, 1965):

$$e' = e \left(\frac{1}{1 - \epsilon} \right)$$

$$a' = a \left(\frac{1}{1 + \nu \epsilon} \right)$$

$$f' = f \left(\frac{1}{1 + \nu \epsilon} \right)$$

where primes (') indicate values after straining.

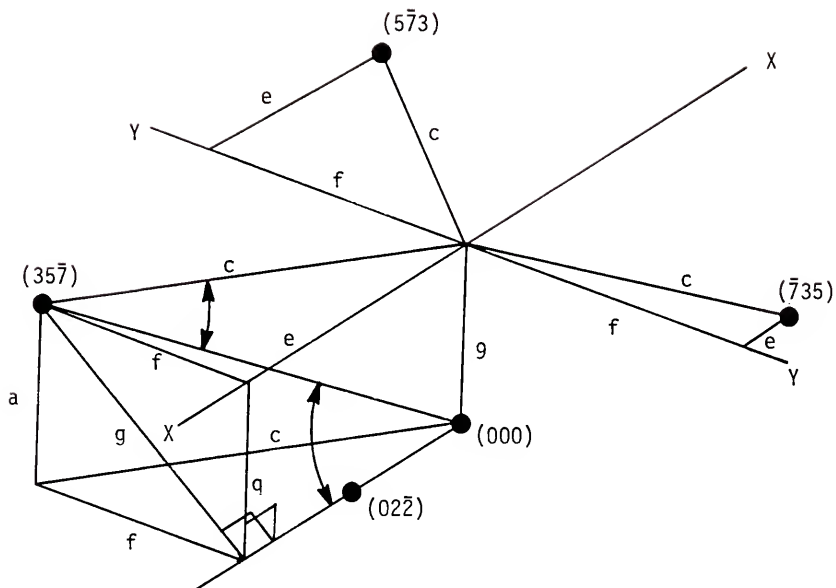


Figure 3.15 Geometry of reciprocal lattice used in strain calculations.

TABLE 3.4
COMPONENTS OF THE {753} PLANES AT 35 kV

	<u>357</u>	<u>735</u>	<u>573</u>
a (Å^{-1})	.10674	.10674	.10674
b (Å^{-1})	1.6843	1.69483	1.6843
c (Å^{-1})	1.6909	1.6809	1.6809
α ($^\circ$)	3.6334	3.6334	3.6334
γ ($^\circ$)	21.3489	89.9301	140.909
g (Å^{-1})	.6132	1.66388	1.0620
e (Å^{-1})	1.5687	.2615	1.3073
f (Å^{-1})	.6038	1.6605	1.0567

The following values may then be calculated:

$$(c')^2 = (e')^2 + (f')^2$$

$$(b')^2 = (c')^2 + (a')^2 = (e')^2 + (f')^2 + (g')^2$$

$$\theta_B' = \sin^{-1} \left[\frac{\lambda}{2} b' \right]$$

$$\alpha' = \tan^{-1} \left[\frac{a'}{c'} \right]$$

The values for a 2% compressive strain are given in Table 3.5.

These data are plotted in Figure 3.16. The actual shifting of points in the (111) reciprocal space is relatively small. The maximum shift for the (111) plane, shown in Figure 3.11, is less than 1 mm. Thus, the major effects are the changes in α and θ_B , and the triangle formed by the 357, 735 and 573 lines will remain a triangle but the length of the sides will change. If bending moments are introduced, the lines forming the triangles could become curved.

To investigate the effect of beam energy on strain sensitivity of the fine structure, calculations were performed at 15 kV and at 200 kV. 15 kV can be obtained on most scanning electron microscopes and represents the beam close to the lower limit of clear patterns with current backscattered electron detectors. 200 kV is the maximum energy available on commercial scanning transmission electron microscopes, some of which can be operated in a channeling mode.

The visibility of fine structure in the 111 plane is limited to a radius of $\theta_{B(220)}$ around the (111) pole. The number of fine lines visible is a result of two effects. As the voltage is decreased, the

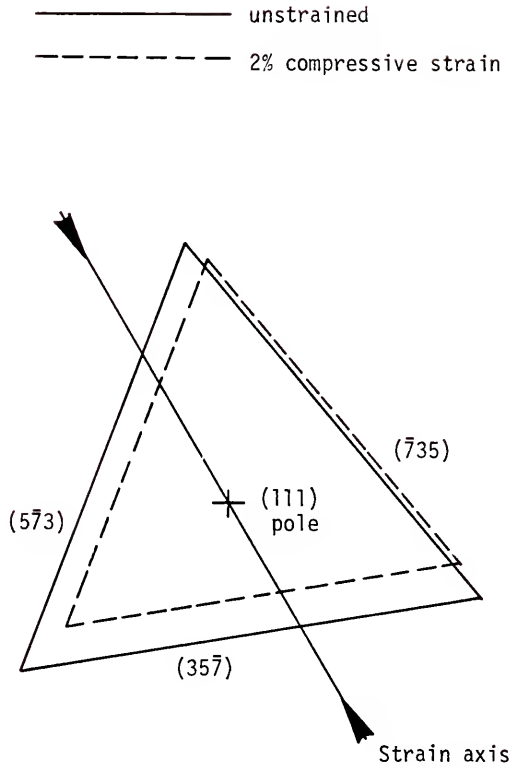


Figure 3.16 Calculated shifts of selected lines in the fine structure near the (111) pole after 2% compressive strain.

TABLE 3.5
 COORDINATE VALUES FOR 2% COMPRESSIVE STRAIN (111) POLE At 35 kV

	$\bar{357}$	$\bar{735}$	$\bar{573}$
a'	.1050	.1060	.1060
e'	1.6007	.2668	1.3340
f'	.5997	1.6492	1.0495
c'	1.7094	1.67061	1.6973
b'	1.7127	1.6740	1.2006
θ_B'	3.2136	3.1409	3.1910
α'	3.5489	3.6311	3.5741
$(\alpha' - \theta_B')$.335	.490	.384
$\alpha - \theta_B^*$.472	.472	.472
$\Delta(\alpha - \theta_B)$	-.137	-.018	-.088

* from Table 3.3

radius of the circle of the intersection of the Ewald sphere and the first order Laue zone decreases, thus decreasing the number of points near the condition $\alpha = \theta_B$. This decreases the number of lines. At the same time, the radius of the visible area around the pole increases, which tends to increase the number of visible lines. The first effect predominates, and the number of visible fine lines decreases with decreasing accelerating potential.

The fine structure at 15 kV is shown in Figure 3.7. Analysis of this structure using the methods described previously reveals that the isolated triangle is formed by {733} planes, specifically the ($\bar{3}\bar{3}7$), ($7\bar{3}\bar{3}$) and ($\bar{3}\bar{7}\bar{3}$). In general, planes with repeated indices where the remaining index is not a 1 will form triangles around the (111) pole. The results for a 2% compression strain for 15 kV are given in Table 3.6.

Notice that one side of the triangle lies on the X axis. All of the changes in $(\alpha - \theta_B)$ are larger than in the 35 kV case.

For 200 kV, there are 39 planes within $\theta_B(220) = .41^\circ$ of the (111) pole. Of these, only the {7713} planes will form a triangle. The results of a 2% compressive strain are given in Table 3.7. Shifts are smaller than at 15 kV.

Thus, although the magnitude of shift in the fine structure does not vary greatly with accelerating potential, the shifts appear to be enhanced at lower accelerating potentials.

TABLE 3.6
 CHANGES IN FINE STRUCTURE AROUND THE (111) POLE
 FOR 2% COMPRESSIVE STRAIN AT 15 kV

	$\bar{3}\bar{3}7$	$7\bar{3}\bar{3}$	$\bar{3}7\bar{3}$
q	.10674	.1067	.1067
e	1.30730	0	1.3073
f	.75480	1.5095	.7548
α	4.04500	4.0450	4.0450
θ_B	4.33900	4.3390	4.3390
$(\alpha - \theta_B)$	-.294	-.294	-.294
a'	.1062	--	--
e'	1.3340	0	1.3340
f'	.7497	1.4992	.7497
α'	4.3986	4.3096	4.3986
θ_B'	3.9633	4.0451	3.9633
$(\alpha' - \theta_B')$	-.435	-.264	-.435
$\Delta(\alpha - \theta_B)$	-.141	+0.30	-.141

TABLE 3.7
 CHANGES IN FINE STRUCTURE AROUND THE (111) POLE
 FOR 2% COMPRESSIVE STRAIN AT 200 kV

	$77\bar{1}\bar{3}$	$7\bar{1}\bar{3}\bar{7}$	$\bar{1}\bar{3}\bar{7}\bar{7}$
q	.10674	.10674	.10674
e	2.6145	2.6145	0
f	1.5095	1.5095	3.0190
α	2.0250	2.0250	2.0250
θ_B	2.3707	2.3707	2.3707
$(\alpha - \theta_B)$	-.346	-.346	-.346
a'	.1060	.1060	.1060
e'	2.6679	2.6679	2.6679
f'	1.4992	1.4992	1.4992
α'	1.9840	1.9840	2.0248
θ_B'	2.4032	2.4032	2.3546
$(\alpha' - \theta_B')$	-.419	-.419	-.419
$\Delta(\alpha - \theta_B)$	-.073	-.073	-.016

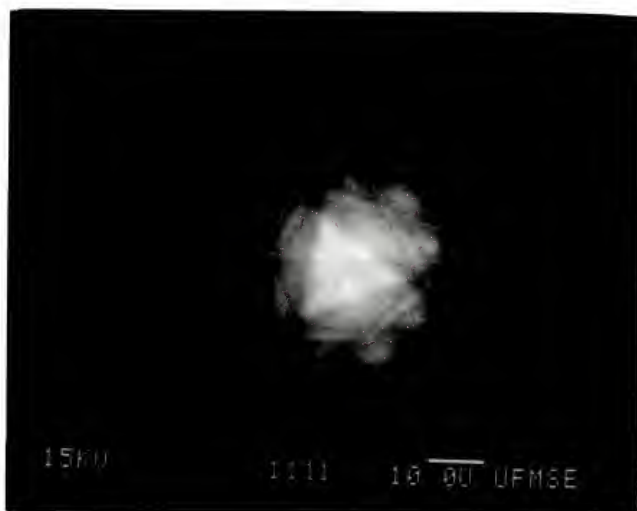


Figure 3.17 Fine structure around the (111) pole at 15 kV.

3.4 Other Lines From the First Order Laue Zone

Figure 3.18 shows an electron channeling pattern of silicon at 15 kV. There are several lines that intersect in the center of the bands formed by the {220} planes near the circle formed by the intersection of the Ewald sphere and the first order Laue zone, as shown in Figure 3.19. These lines have approximately the same contrast as the higher order lines of the zero order Laue zone; e.g., the {440} lines, but their three-fold symmetry suggests an origin in the first order zone.

Unknown lines in electron channeling patterns suspected of being in the first order zone can be indexed in the following manner: First, a drawing of the channeling pattern is made to a convenient scale on top of a map of the first order zone, such as Figure 3.11. The low order planes; i.e., the {220} planes in the case of (111) pole, should be included, along with the circle formed by the intersection of the Ewald sphere with the first order zone. The channeling pattern may be calibrated by measuring the width of the {220} bands or, more accurately, by measuring the diameter of the circle formed by the intersection of the Ewald sphere and the first order zone. The width of the {220} bands equals $2\theta_{B(220)}$, while the diameter of the circle is $2\theta_C$, where

$$\theta_C = \sin^{-1} [R\lambda] = 2 \tan^{-1} \left[\frac{h}{R} \right]$$

from Figure 3.8. An unknown line is selected and the perpendicular distance from the unknown line to the center of the (111) pole measured on the channeling pattern and converted to degrees. This number must be $\pm (\alpha - \theta_B)$. The unknown line is then drawn on the drawing of the channeling

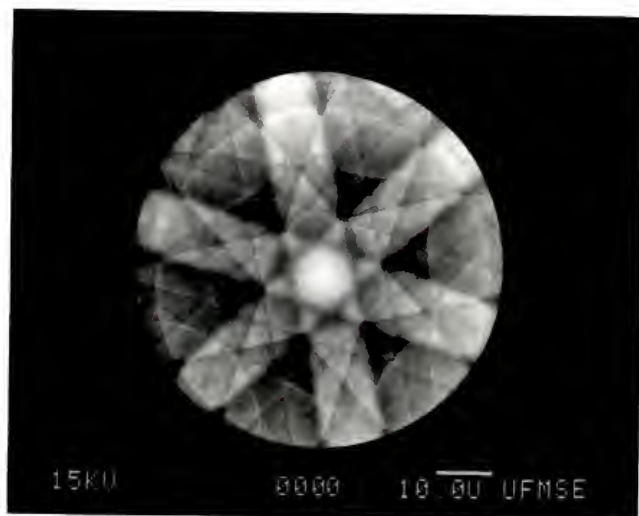


Figure 3.18 ECP of (111) silicon at 15 kV.

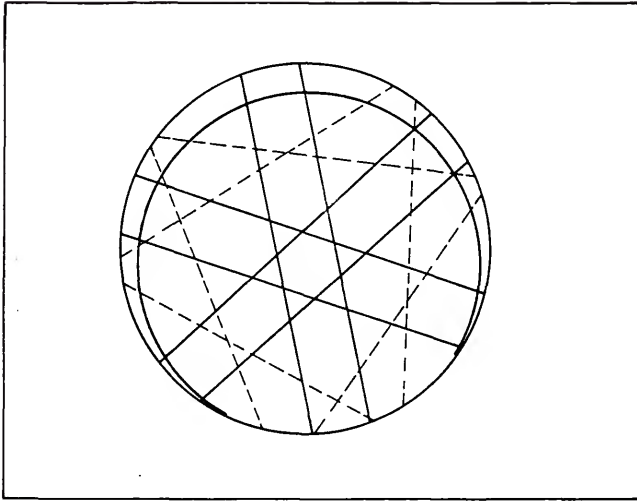


Figure 3.19 Lines in the (111) channeling pattern at 15 kV with three-fold symmetry are shown dotted.

pattern superimposed on the first order Laue zone. Another line is then drawn perpendicular to the unknown line and passing through (000). The point in the first order Laue zone representing the unknown must lie on (or near) this line. Points near the line are selected and values for $(\alpha - \theta_B)$ calculated. By comparison with the measured value for $(\alpha - \theta_B)$, the indices of the plane can be determined. Other members of the same family of planes can then be plotted and visually compared with the experimental channelling pattern.

As an illustration of this technique, the lines in Figure 3.19 will be analyzed. Figure 3.20 shows the zero order lines plotted on a first order map and one of the unknown lines plotted along with a perpendicular line running through (000). The distance measured from the center (from Figure 3.18) was 5.2° , using a calibration of $1^\circ = 3.58$ mm determined from measuring the diameter of the circle of intersection. It is important to note that any {220} plane is not equivalent crystallographically to the planes 30° on either side. Thus, orientation of the drawing of the electron channeling pattern to the experimental pattern based only on points in the zero order zone has a two-fold ambiguity. Although both possibilities could be tried and the correct one selected, the ambiguity can be eliminated by the fine structure in the center of the (111) pole which only has three-fold symmetry. In Figure 3.17, the triangle formed by the three {733} lines is faintly visible. If it were not, the channeling pattern could be re-photographed with the brightness reduced to make the center area visible, or the center area could be temporarily magnified with the brightness suppressed. Either way, the orientation of the triangle can be determined experimentally, and by

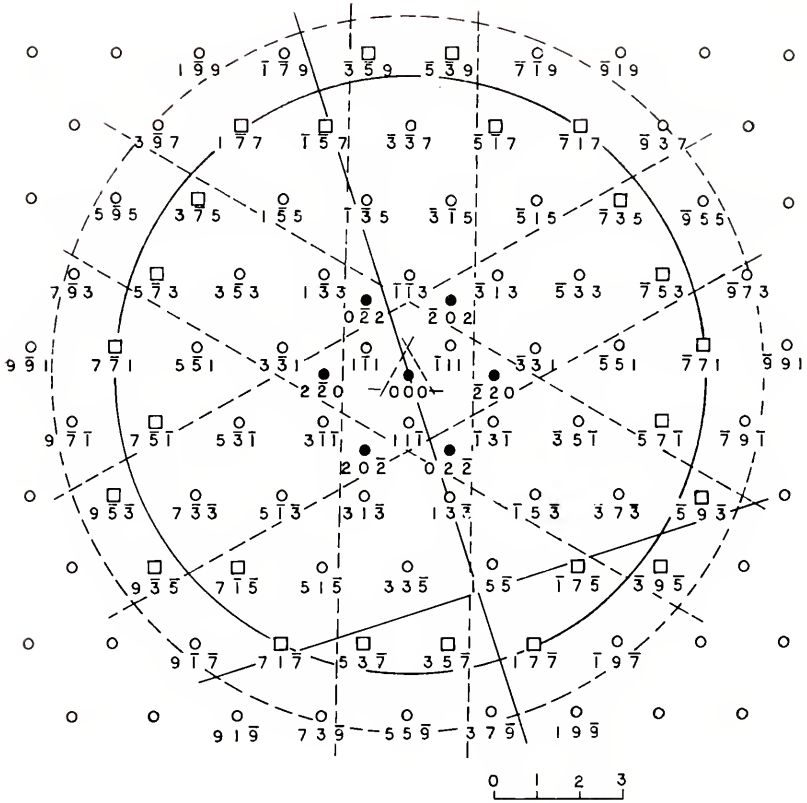


Figure 3.20 Analysis of one of the three-fold symmetry lines of Figure 3.19. Dotted lines are zero order planes superimposed on first order plot. Unknown line is shown solid at bottom, with perpendicular line passing through the origin. Scale is in degrees.

drawing the three {733} lines on the constructed channeling pattern, the proper orientation can be assured.

From Figure 3.18, the possible planes forming the unknown line are $\bar{1}\bar{7}9$, $\bar{1}\bar{5}7$, $\bar{1}\bar{3}5$ and $13\bar{3}$. Table 3.8 shows the calculated angles for those planes.

Note that since the unknown line is not parallel on the opposite side of (000) (see Figure 3.18) the $\bar{1}\bar{7}9$, $\bar{1}\bar{5}7$ and $\bar{1}\bar{3}5$ planes would have to have $(\alpha - \theta_B) < 0$, i.e., $\sim -5.2^\circ$, while the $13\bar{3}$ would have to have $(\alpha - \theta_B) = +5.2^\circ$. This eliminates all planes except the $13\bar{3}$. The other five {133} planes, viz, $31\bar{3}$, $\bar{3}31$, $\bar{3}13$, $1\bar{3}3$ and $3\bar{3}1$, can then be drawn. The result is shown in Figure 3.21, which is merely an indexed version of Figure 3.19.

Why the {331} planes appear and other planes with similar values of α and θ_B , such as the {513}, do not, is unknown.

The {331} lines, like the fine structure near the pole center, should be sensitive to strain. Calculations identical to those described in Section 3.2 were performed on three of the {331} planes. The results are given in Table 3.9, with primed values indicating a 2% compressive strain.

Comparison of Table 3.9 with Table 3.6 reveals that the angular changes caused by a 2% compressive strain are greater for the {331} lines than the {733} lines. However, the greater magnification used when analyzing the center structure makes the actual shift on the CRT (or the photograph) more apparent for the {733} lines. The {331} line shifts can be used on a standard SEM equipped for channeling, while the center structure analysis requires decreasing current to the scanning coils while in the channeling mode to increase magnification.

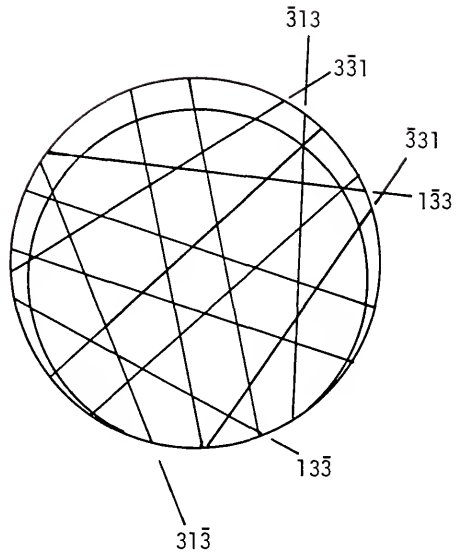


Figure 3.21 Indices of three-fold symmetry lines.

TABLE 3.8
 α AND θ_B VALUES FOR POSSIBLE PLANES FORMING UNKNOWN LINES
 IN FIGURE 3.19

	$h^2+k^2+l^2$	α	θ_B	$(\alpha - \theta_B)$
179	131	2.8915	5.0734	-3.192
157	75	3.822	4.592	-7.700
135	35	5.600	3.135	2.465
133	19	7.6114	2.309	5.302

TABLE 3.9
 SHIFTS IN {331} LINES FOR A 2% COMPRESSIVE STRAIN AT 15 kV

	31 $\bar{3}$	$\bar{3}31$	1 $\bar{3}3$
a	.10674	.10674	.10674
e	.522911	.261455	.78436
f	.60382	.75476	.15095
a'	.106015	.106015	.0106015
e'	.53358	.26679	.80037
f'	.59972	.74963	.14992
c'	.80273	.75969	.81429
b'	.80970	.80272	.821162
θ_B'	2.3202	2.3002	2.4241
α'	7.5234	7.9443	7.4178
$(\alpha' - \theta_B')$	5.2032	5.6441	4.9937
$\Delta(\alpha - \theta_B)$	5.302	5.302	5.302
$(\alpha - \theta_B)$	-.099	+.362	-.308
shift, mm*	.35	1.29	1.10

*on the scale of Figure 3.18

3.5 Summary

Fine structure near low index poles has been observed for some time, and although assumed that these lines were from high index planes, no simple method for indexing these lines existed. A method for indexing these lines based on the Ewald sphere-reciprocal lattice construction has been proposed, where the origin of these fine lines is in the first order Laue zone rather than the zero order Laue zone, which is the origin of the majority of the lines in an electron channeling pattern.

In addition, there are other lines in an electron channeling pattern located well away from the area surrounding the poles, that also originate in the first order Laue zone. These lines had not been previously indexed.

The position of lines in the first order Laue zone are sensitive to elastic strain. A method for calculating shifts in the fine structure due to strain has been described.

Some lines remain absent from the fine structure for, as yet, undetermined reasons.

CHAPTER 4 EXPERIMENTAL METHODS

4.1 Introduction

The proposed research involves changes in channeling patterns produced by elastic and plastic strains on single crystals. Plastic strains are produced by prior plastic deformation; and elastic strains by use of a tensile stage in the SEM, so channeling patterns can be obtained at various levels of elastic strain. Ideally, the plastically strained sample would contain parallel arrays of dislocations of the same type and Burgers vector.

Initial attempts involved the growing of thin, single crystal epitaxial films of gold and silver. Both materials are face-centered cubic crystal structure and form pure edge dislocations during plastic straining. Thin films have the advantage of needing no further preparation for transmission electron microscopy and the high atomic numbers of both materials mean a high backscattered electron coefficient. Samples could be plastically strained by mounting on a TEM grid, followed by gentle squeezing to strain the film. The extent of deformation could be determined by observing the dislocations formed in the TEM. Elastic strain could be obtained by placing the film over a small hole in a standard tensile dogbone and applying tensile strain.

Attempts to grow macroscopically-sized (i.e., 1-2 mm) single crystals proved unsuccessful with the available equipment. Preparation of these films has been reported in the literature, but apparently requires an exceptionally clean, dedicated vacuum system to obtain consistent results.

A second material tried was single crystal aluminum. The approach was to take thin slices of annealed bulk single crystals of Al of known orientation, plastically deform samples by bending to a known radius, and electrochemical thinning to allow TEM examination to determine the character of the dislocations. Channeling would also be performed on selected thinned areas of the samples. Elastic strains would be obtained on rectangular samples epoxied to steel ends to form a composite "dogbone" for the tensile stage of the SEM. Aluminum also forms edge dislocations when plastically deformed.

Several problems were also encountered on the aluminum samples. Dislocations, although present in appreciable concentrations, were highly mobile, especially in areas of high concentrations, and beam heating in the TEM caused them to move. This same heating caused thinned areas of the foil to bend and distort, thus changing the local crystallographic orientation. Thinned areas were also very fragile, and tended to crack and bend with time. Channeling was impossible on thinned areas due to local bending.

Finally, silicon was selected as a material. Silicon has the distinct advantage of being brittle at room temperature, allowing elastic strain experiments to be done free from dislocation formation; and ductile at higher temperatures, allowing dislocations to be introduced by plastic straining at high temperature and frozen in place by cooling to room temperature. Silicon is also readily available in macroscopically-sized dislocation-free, polished single crystals from the electronics industry.

4.2 Preparation of Samples for Elastic Straining

{111} discs of electronic grade silicon two inches in diameter by .010 inches thick were cut, by laser, into 2 mm wide strips perpendicular to the (110) direction (indicated on the sample by a flat edge). Initially, samples were epoxied to metal ends to form a composite dogbone for testing. Shifting of the metal ends in the grips during loading caused bending moments, and premature fracture during tensile loading. Also, the use of ductile metal ends made strain measurement via change in crossbead position inaccurate.

Samples were finally simply epoxied into place on the crossheads, a procedure which made specimen removal after completion of testing more difficult but made determination of the zero strain point much easier, and application of moments during testing due to sample shifting was eliminated.

Crossheads were spaced at 1 cm before the sample was epoxied in place, and a small 1000 mesh TEM grid attached to the upper surface for channeling alignment. The crossheads had to be modified to bring the sample up to the small (~ 9 mm) working distance required for electron channeling.

Initial tests were performed in tension, but maximum strain in this situation was limited to < 1% before brittle fracture occurred. Testing was switched to compressive mode, allowing ~ 2% strain before failure. Testing was performed with fine structure on the ECPs being recorded at 1% increment strain intervals until failure occurred.

4.3 Plastically Strained Specimen Preparation

Specimens $3/8" \times 1-1/2"$ were cut from $2"$ dia. $\times .010"$ silicon wafers as shown in Figure 4.1. These were then placed between two U-shaped rods of fused silica to form a 4-point bending jig, as shown in Figure 4.2. A weight was placed on top of the upper U-shaped rod and the entire assembly heated to 1025°C for 20 minutes in dry hydrogen to allow plastic flow.

After deformation, two $1/8"$ wide strips from the areas immediately beneath the inner two rods were removed by scratching with a diamond scribe and fracturing. The remaining silicon was discarded. The two $1/8" \times 3/8"$ strips were then attached to glass microscope slides with melted Crystobond*. Crystobond liquifies at low temperature and turns to a brittle solid upon cooling. Three mm discs were then cut ultrasonically using silicon carbide abrasive. Three discs could be cut from each strip, giving six discs per sample.

Thinning was accomplished in two stages, dimpling and final thinning. Specimens were prepared for dimpling by coating all but a $1.0-1.5$ mm area in the center of one side of the disc with "black wax" used in the semiconductor industry. This was accomplished by placing the disc in a small pool of melted black wax on the surface of a heated microscope slide and teasing the liquid wax around the circumference with a dental pick. The samples were then removed with forceps and allowed to cool.

Silicon wafers have only one highly polished surface, the other being somewhat rougher. Since the irregularities in the rougher surface require a substantial amount of etching to remove, dimpling was done on this surface.

*Aremco Products, Inc.

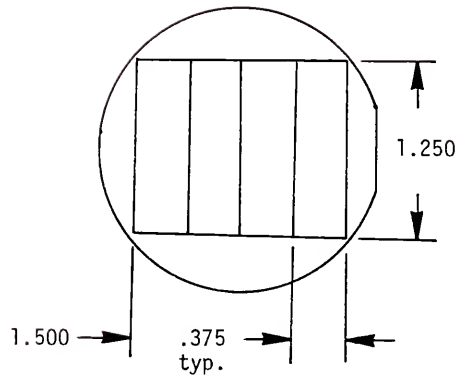


Figure 4.1 Cutting of samples for plastic straining.

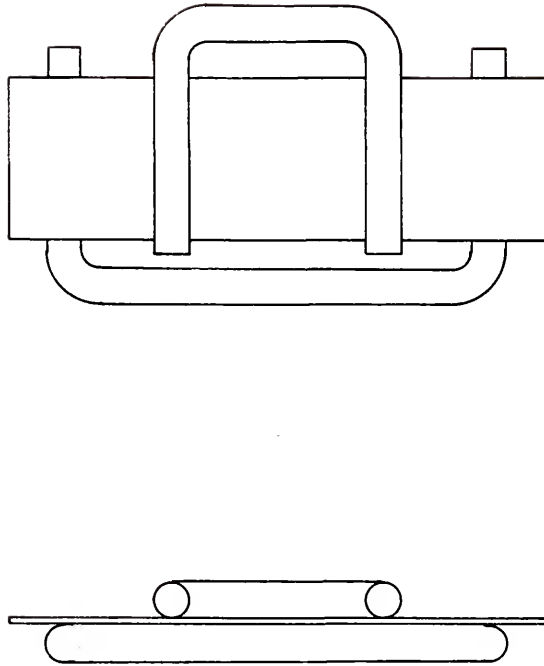


Figure 4.2 Four-point bending jig. Weight is applied to the smaller U-shaped piece. Drawing in three times full size.

Dimpling was accomplished by grasping the edge of the sample in locking forceps and suspending it in a magnetically stirred solution of 10% hydrofluoric acid and 90% nitric acid with the sample oriented so the stirred liquid impinges on the exposed area.

Samples were etched for 10 minutes, rinsed in distilled water, rinsed in methanol and placed in two baths of electronic grade trichloroethylene to remove the black wax. Samples were then washed in methyl alcohol and temporarily stored in distilled water.

Final thinning was accomplished by suspending the unmasked specimens, held by forceps as during dimpling, in the HF-HNO₃ mixture. After a two-minute initial etch, specimens were examined at 20-second intervals under a low-power binocular microscope to evaluate the progress of the thinning. Thin areas of the samples transmit light at longer wavelengths and appear red or yellow. At this point, samples were dipped in etching solution for several seconds between observations. Etching was stopped when a small hole had formed. The sample was given a final rinse in distilled water and stored in absolute ethanol until observation.

A great many problems were encountered in the preparation of thin samples suitable for electron channeling. The first was substantial amounts of surface contamination, shown in Figure 4.3. Although this sample would be suitable for conventional TEM due to the relatively large distances between particles, electron channeling requires a 10 μ diameter circle, and these particles obliterate the pattern. This problem was traced to solvent immiscibility. The original procedure included ethanol instead of methanol washes after the trichloroethylene. Trichloroethylene is insoluble in ethanol, and this apparently caused the problem.



Figure 4.3 Surface contamination from thinning.

The second problem was rough edges around the etched hole, as shown in Figure 4.4. This problem was never completely solved, but appears to be related to a second phase build-up near the hole, as shown in Figure 4.5. This phase was never identified, although occasionally a second set of spots was observed in the diffraction mode of the TEM, indicating crystallinity. Since the etching solution works by first oxidizing the silicon to quartz and then dissolving the quartz in hydrofluoric acid, one possibility is that this second phase is undissolved quartz, but changing the amount of HF in the etch did not eliminate the problem.

The problem was finally solved by etching for a slightly longer time during the final thinning. This produced a more steeply tapered foil but, as will be discussed shortly, a more steeply tapered foil was necessary for another reason.

Since channeling contrast increases with decreasing specimen thickness, one might assume that obtaining channeling patterns from thin foils would be easy. This is not the case for the reasons shown in Figure 4.6, which shows a trace of backscattered intensity along a scan line approximately perpendicular to the foil edge at 35 kV at two amplifier settings. The lower line was taken with the gain of the backscattered amplifier set for saturation of the film emulsion in the saturated region. This is at a considerably lower gain than is used for electron channeling. The effect of increasing the gain to the level required for channeling is shown in the upper line, which saturates at the same distance from the foil edge as the lower line.

Thus, channeling contrast from an area is superimposed on a steeply varying background. A typical channeling pattern obtained from the less



Figure 4.5 Second phase near thinned hole.

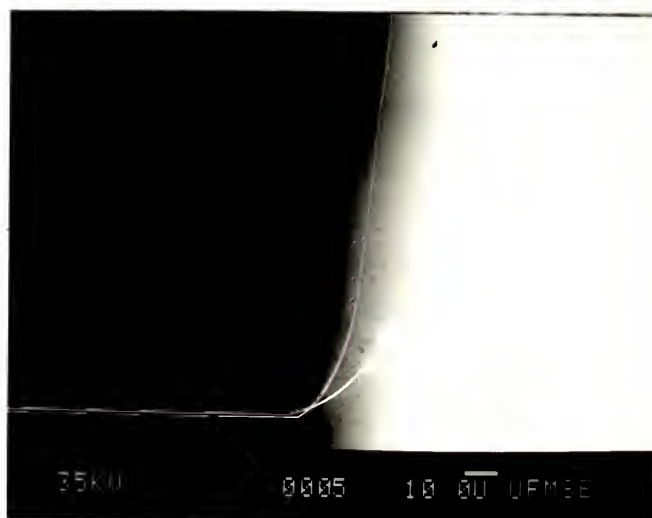


Figure 4.6 Backscattered signal intensity near tail edge at 35 kV.

than saturated area is shown in Figure 4.7. The edges of the bright area have visible channeling contrast. The bright and dark areas also have channeling contrast, but superimposed on either a too high or low background.

If the beam did not wander while tilting during channeling, the background signal in the channeling pattern would be more regular, being brighter when the beam was angled towards the thicker areas, weaker when angled towards the thinner sections, and weakest when normal to the foil centerline. The irregular contrast of Figure 4.7 indicates that, in spite of dynamic correction, the beam wandered around on the specimen surface. By taking a uniformly tapered specimen and channeling at various levels of D.C. suppression along two orthogonal directions, the exact path of the beam might be determined.

Unfortunately, the only variables on the backscattered electron amplifier are gain and D.C. suppression. The D.C. suppression subtracts a selected constant value of D.C. voltage from the input signal before amplification to eliminate what is, in the channeling signal from a thick specimen, a constant background signal. Since the background signal from a tapered film varies, D.C. suppression will provide proper contrast only over a small region.

If channeling patterns are made on areas in the saturated region, the foils are too thick to be visible with 200 kV on the TEM.

There are three possible ways out of this dilemma: Producing foils of constant thickness across a 10μ area, so that no variation of backscattered coefficient occurs in the channeled area; use of higher voltage in the TEM so that dislocations are visible in thicker areas of the foil;



Figure 4.7 Electron channeling pattern from thin tapered foil at 35 kV.

or decreasing the beam energy for electron channeling so that backscattered electron emission saturates at a point closer to the foil edge.

Fabrication of uniform thickness single crystal foils was deemed an unlikely alternative due to the presence of second phase material near the center of the dimples, where the thickness is likely to be the most uniform, and the efficiency of establishing landmarks without a hole edge for reference. Earlier efforts to establish landmarks with contamination marks proved unsuccessful due to the ease with which they could be erased.

The use of a higher energy TEM was eliminated because in silicon point defects occur at 220 kV, and these could also affect the channeling pattern. This effect would be especially severe since the only other machine available to the author with beam energy greater than 200 kV is the 1 MeV machine at Oak Ridge National Laboratories.

Thus, the method used to eliminate this problem was lowering the energy of the beam during channeling. The lower the beam energy, the wider the bands, and the greater the area of the pattern obscured by the center star. This serves to limit the areas from which good intensity profiles can be obtained. Also, as beam energy decreases, noise is increased, and detector efficiency decreases. 15 kV was selected as a good compromise. Figure 4.8 shows the backscattered intensity at 15 kV. The intensity saturates at $\sim 15 \mu$ from the foil edge, compared with $\sim 60 \mu$ at 35 kV (Figure 4.6) Figure 4.9 shows an ECP of the (111) pole of silicon.

As an experimental note, care was taken to insure that the black levels of the signal in Figures 4.6 and 4.8, corresponding to the signal when the beam is not striking the foil, was maintained at a small positive value of detector voltage. If this were not the case, signal saturation could be produced arbitrarily by changing D.C. suppression.

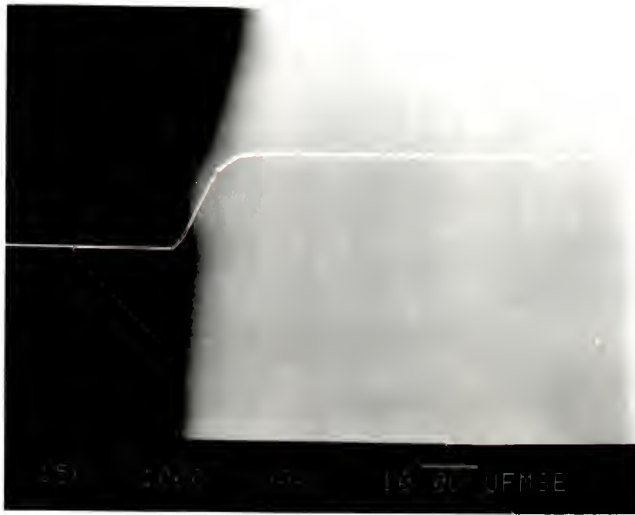


Figure 4.8 Backscattered signal intensity near foil edge at 15 kV.

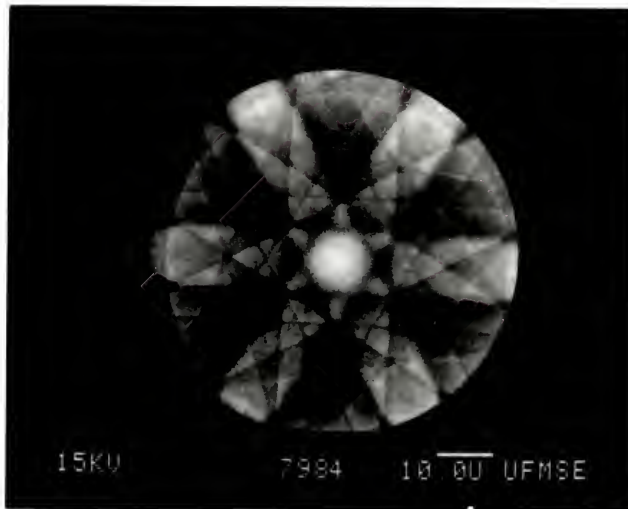


Figure 4.9 (111) silicon ECP at 15 kV.

In order to perform transmission electron microscopy on the same area as electron channeling patterns, accurate determination of the location of specific areas on the specimen surface is necessary. The most convenient landmark is the profile of the edge of the hole in the foil. A gradually tapered foil will produce acceptable channeling patterns too far from the edge to allow accurate location of the channeled area in the TEM. Thus, a relatively steeply tapered foil is an advantage. This can be obtained by leaving the specimen in the final thinning etch slightly longer.

CHAPTER 5 RESULTS AND DISCUSSION

5.1 Plastically Strained Samples

5.1.1 Electron Channeling Patterns

Channeling patterns were obtained from chemically thinned, plastically deformed silicon specimens prepared as described in the previous chapter. An area near the hole produced by the thinning was selected and the SEM switched to the channeling mode. The sample was moved until changes in the channeling pattern were noticed. The location of the channeling area was recorded by double exposures in the image/SAI mode. The channeling pattern was recorded along with intensity profiles along selected scan lines. In general, two scans were taken from each {220} band, one on either side of the (111) pole at the point where the {422} bands crossed, as shown in Figure 5.1. Scanning on both sides of the (111) pole was necessary because two of the {331} planes intersect at different points, as explained in Section 3.3, and this affects the intensity profiles.

The necessity of scanning at the same crystallographic location is shown in Figures 5.2, 5.3 and 5.4, which show multiple scans from a {220} plane on a bulk dislocation-free silicon sample. Although major features are symmetrical, the minor peaks are different on either side of the center. The width, contrast and shape of the {220} bands varies with distance from the center (i.e., the (111) pole).

The area immediately around the {220} plane in Figures 5.3 and 5.4 are shown in Figure 5.5 and 5.6. This is the same horizontal scale that

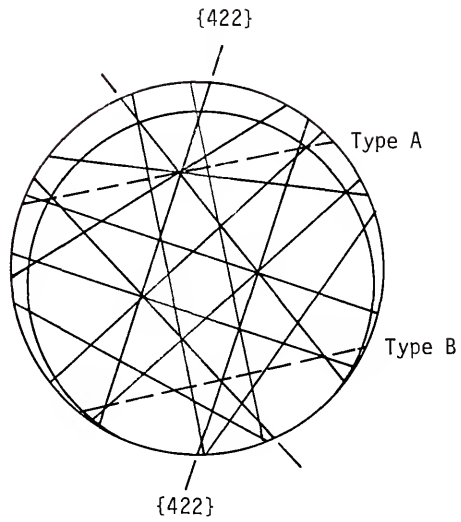


Figure 5.1 Location of intensity scans for typical $\{220\}$ plane at 15 kV.

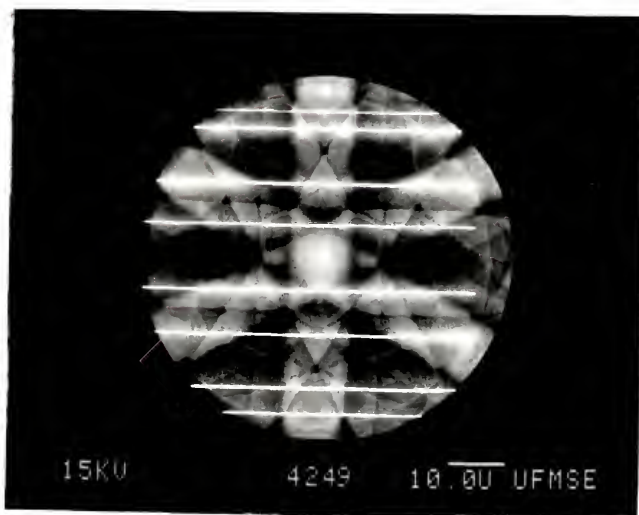


Figure 5.2 Scan lines for intensity profiles in Figures 5.3 and 5.4. Lines stopping short of the right edge are an electronic artifact.

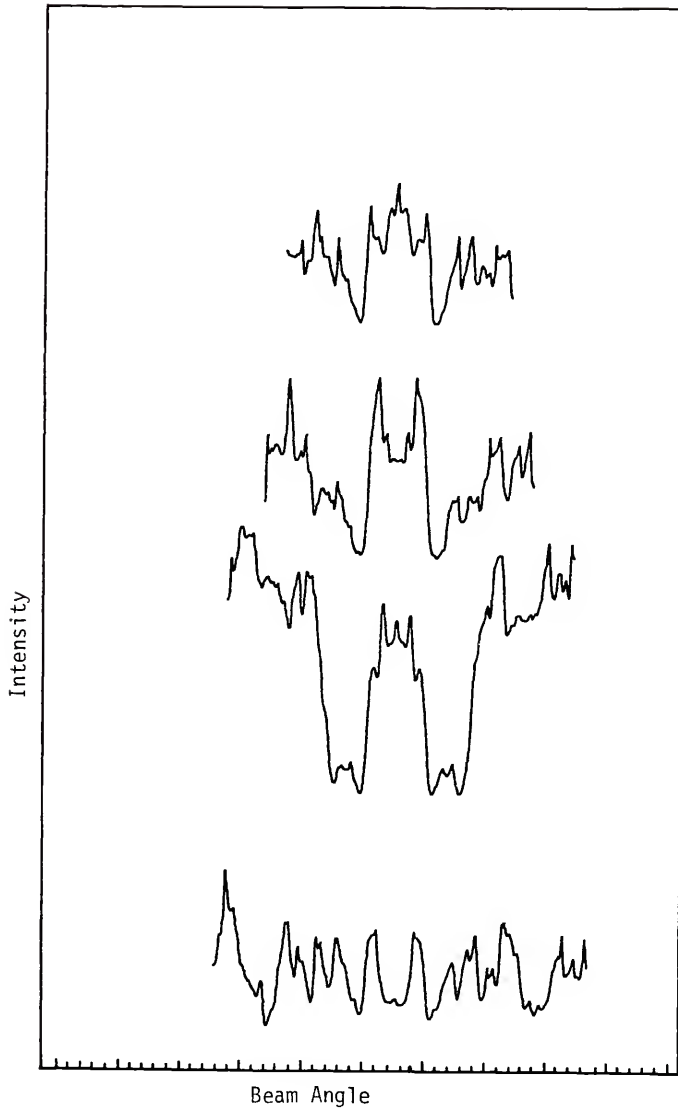


Figure 5.3 Upper four intensity profiles from Figure 5.2. Central pair of peaks is the {220} plane.

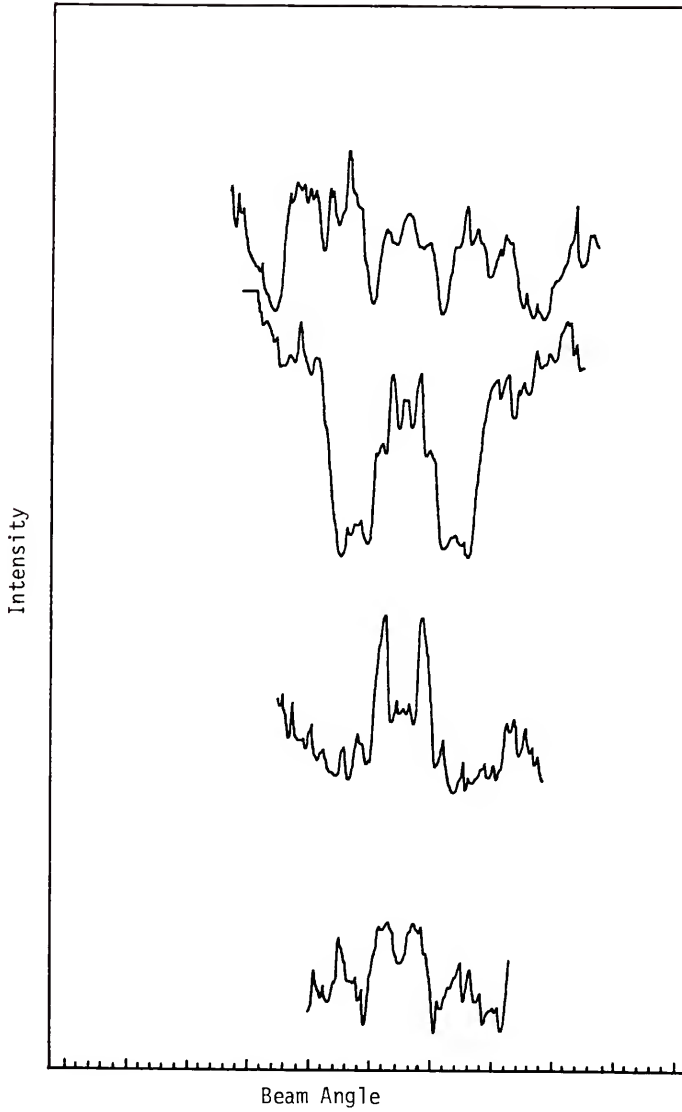


Figure 5.4 Lower four intensity profiles from Figure 5.2. Central pair of peaks is the {220} plane.

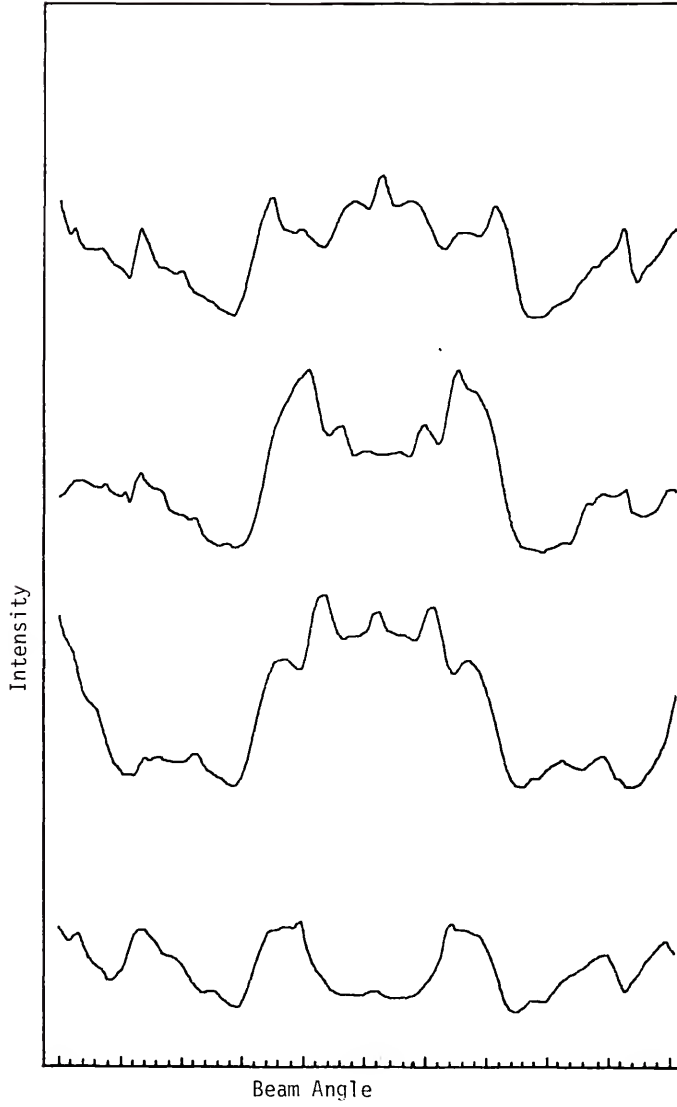


Figure 5.5 Area around the {220} plane from Figure 5.3.

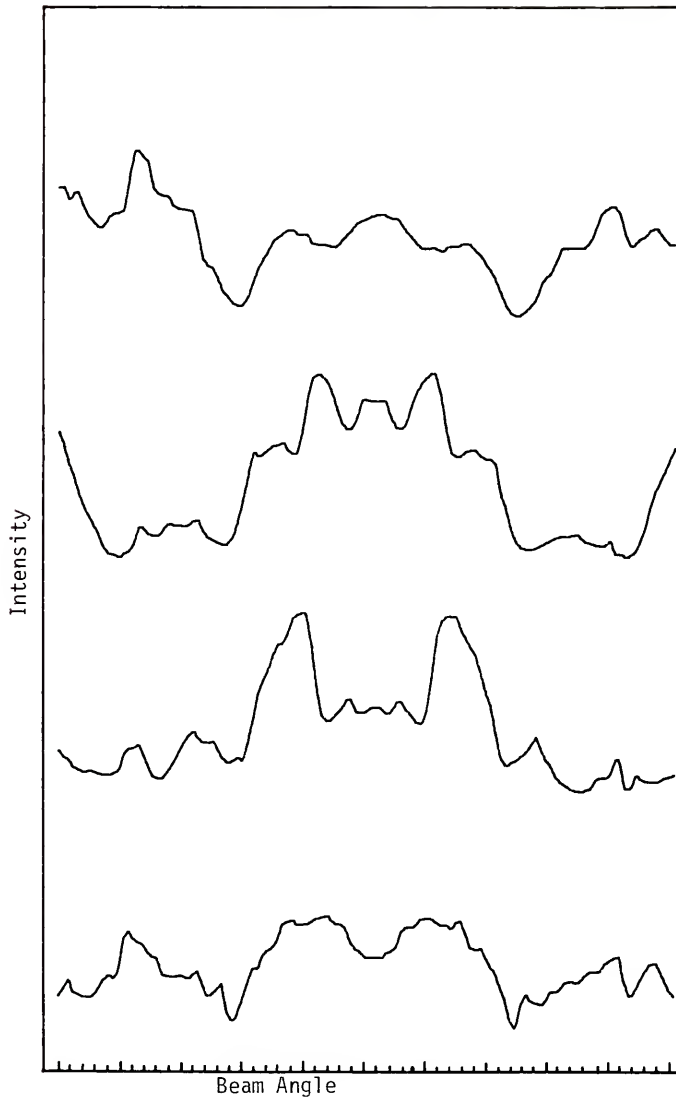


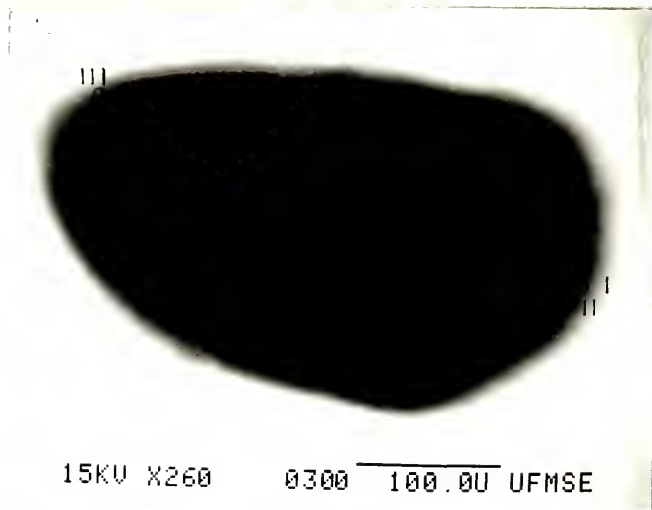
Figure 5.6 Areas around the $\{220\}$ plane from Figure 5.4.

scans were taken of deformed silicon. The differences in peaks in the {220} planes are more apparent.

In plastically deformed samples, the SEM was operated in the channeling mode and the area near the hole left by the thinning was mechanically searched for locations that produced the greatest changes in the electron channeling pattern. Areas producing large visible changes in the ECPs, as compared to a dislocation-free ECP, were recorded, along with an area that produced no visible changes to serve as a control. Locations of these areas were recorded photographically by double exposures in the image and SAI modes. Patterns were obtained close enough to the edge of the hole to be located at 1300X (1000X indicated*) using the edge as a reference. This was necessary so the same area could be located again if needed for generation of additional channeling patterns and so that the same area could be located for examination by transmission electron microscopy. The areas are shown on a low magnification photograph of the hole in Figure 5.7(a). Locations of the three areas are shown at 1300X in Figures 5.7(b), 5.8(a) and (b). Features of each area are summarized in Table 5.1.

On areas I and II, two scans were made on each {220} plane, one on either side of the (111) pole, for a total of six scans. For convenience, intensity scans for the same planes on opposite sides of center are designated type A and type B, as shown in Figure 5.1. Type B scans are from the half of the plane in which the two {331} lines cross farther from the (111) pole than the point where the {422} planes cross, while type A scans are those where the {440} and {331} planes cross coincidentally.

*see Acknowledgements.



(a)



(b)

Figure 5.7 (a) hole with arrows marked. (b) Area I.



(a)



(b)

Figure 5.8 (a) Area II. (b) Area III.

TABLE 5.1
AREAS OF INTEREST IN THE PLASTICALLY DEFORMED SAMPLE

<u>Designation</u>	<u>Figure</u>	<u>Characteristics</u>
Area I	5.7(b)	Control—no noticeable changes in electron channeling pattern
Area II	5.8(a)	Loss in contrast of ECP, no bending of bands
Area III	5.8(b)	Small loss in contrast with band broadening and severe band bending

On area III, all higher order lines and lines from the first order Laue zone were obliterated by the distortion of the pattern and the (111) pole was displaced from the center of the pattern so that only a single scan on one side of the pole was made of each plane. It was not possible to tell if individual scans were type A or B.

Thin films on channeled surfaces also decrease the contrast of ECPs, as discussed in Chapter 1. Contaminants can be formed on the surface of specimens due to the interaction of the electron beam, the specimen surface, and residual gases in the vacuum system (e.g., diffusion pump oil). The loss of contrast from contamination build-up could be erroneously interpreted as strain.

To eliminate this possibility, the specimen was slightly shifted after the area II intensity profiles were recorded to determine if the contrast of the ECP might be further reduced, i.e., if the location of area II was truly a minimum in ECP contrast. If the loss in contrast of the ECP from area II was due to contamination, any shift should increase contrast, since the contamination would occur only near where the electron beam struck the specimen surface. Any shifts to further minimize contrast would be small, since area II was selected for low contrast, i.e., any further minimization would be "fine tuning." As it turned out, a slight reduction in contrast was noticed by a shift in the channeled area to an area overlapping, but not coincident with, area II. This area was labelled area IIR and is shown in Figure 5.9, along with the location of area II. Six intensity profiles were determined from this area.



Figure 5.9 Area IIR with Area II indicated.

Intensity profiles from all areas are presented in Figure 5.10 through 5.31. A summary is given in Table 5.2. Individual scan lines were given numbers for reference.

Since type A and type B intensity scans do not compare directly, all of the intensity profile data was replotted with all the same type of scans for a given ECP plotted together. These plots are summarized in Table 5.3. Scans from area III are not included since there were only three scans.

Obtaining satisfactory intensity levels on a channeling pattern is a compromise between two factors: D.C. suppression and gain. To minimize electronically induced differences between intensity profiles, the gain was held constant at its maximum value and the D.C. suppression adjusted to produce an acceptable signal level.

5.1.2 Transmission Electron Microscope Studies

The same areas which were channeled were examined by transmission electron microscopy (TEM). The analysis was complicated by the high degree of taper of the specimens, which was necessary to produce areas that could be used for reference, as discussed in Chapter 4. This produced a large variation in intensity across the micrograph. Two-beam conditions were established to make dislocations visible by use of a double tilt specimen holder. All micrographs are at 5000X, all diffraction patterns at 82 cm camera length.

Analysis of area I was straightforward. A typical micrograph for area I and the corresponding diffraction pattern are shown in Figure 5.38. The area had few dislocations.

TABLE 5.2
SUMMARY OF INTENSITY PROFILE DATA

<u>Figure</u>	<u>Area</u>	<u>Description</u>
5.10	I	Unrotated ECP for scans 64-69
5.11(a)	I	Rotated ECP for scans 64-65
5.11(b)	I	Rotated ECP for scans 66-67
5.12	I	Rotated ECP for scans 68-69
5.13	I	Intensity profiles 64(A) and 65(B)
5.14	I	Intensity profiles 66(B) and 67(A)
5.15	I	Intensity profiles 68(B) and 69(A)
5.16	II	Unrotated ECP for scans 58-63
5.17(a)	II	Rotated ECP for scans 58-54
5.17(b)	II	Rotated ECP for scans 60-61
5.18	II	Rotated ECP for scans 62-63
5.19	II	Intensity profiles 58(A) and 59(B)
5.20	II	Intensity profiles 60(B) and 61(A)
5.21	II	Intensity profiles 62(B) and 63(A)
5.22	III	Unrotated ECP for scans 76-78
5.23(a)	III	Intensity profile for scan 76
5.23(b)	III	Rotated ECP for scan 76
5.24(a)	III	Intensity profile for scan 77
5.24(b)	III	Rotated ECP for scan 77
5.25(a)	III	Intensity profile for scan 78
5.25(b)	III	Rotated ECP for scan 78

TABLE 5.2—continued

<u>Figure</u>	<u>Area</u>	<u>Description</u>
5.26	IIR	Unrotated ECP for scans 70-75
5.27(a)	IIR	Rotated ECP for scans 70-71
5.27(b)	IIR	Rotated ECP for scans 72-73
5.28	IIR	Rotated ECP for scans 74-75
5.29	IIR	Intensity profiles for 70(A) and 71(B)
5.30	IIR	Intensity profiles for 72(B) and 73(A)
5.31	IIR	Intensity profiles for 74(B) and 75(A)

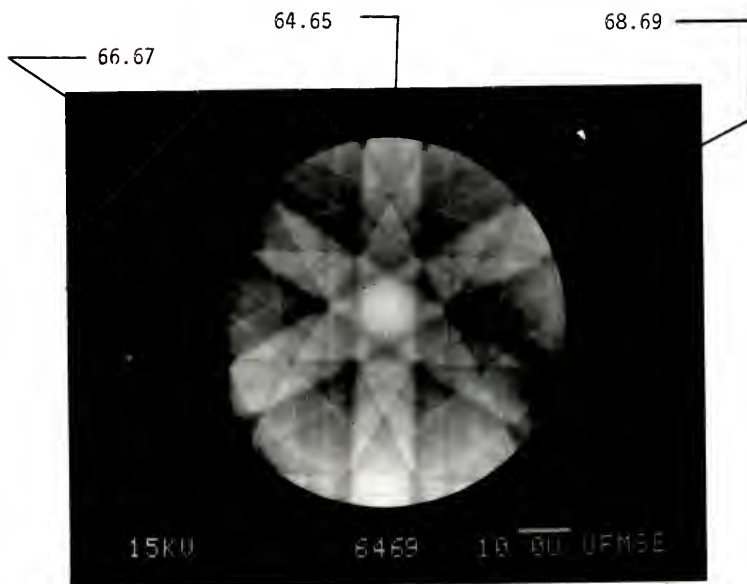
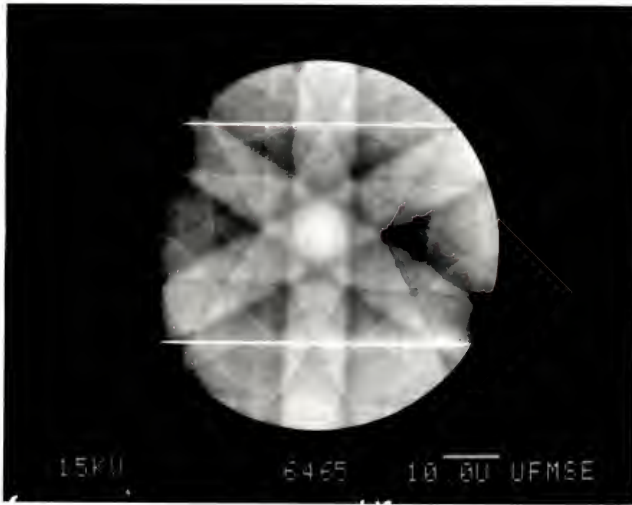
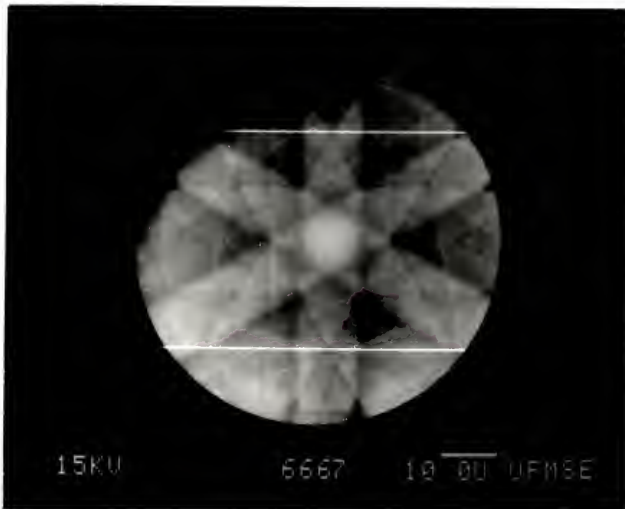


Figure 5.10 Unrotated ECP for scans 64-69, Area I.



(a)



(b)

Figure 5.11 Rotated ECP for scans 64-65 (a), and 66-67 (b).

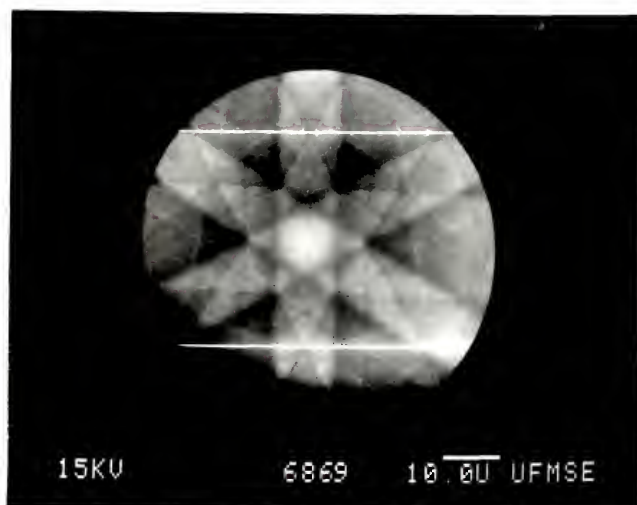


Figure 5.12 Rotated ECP for scans 68-69.

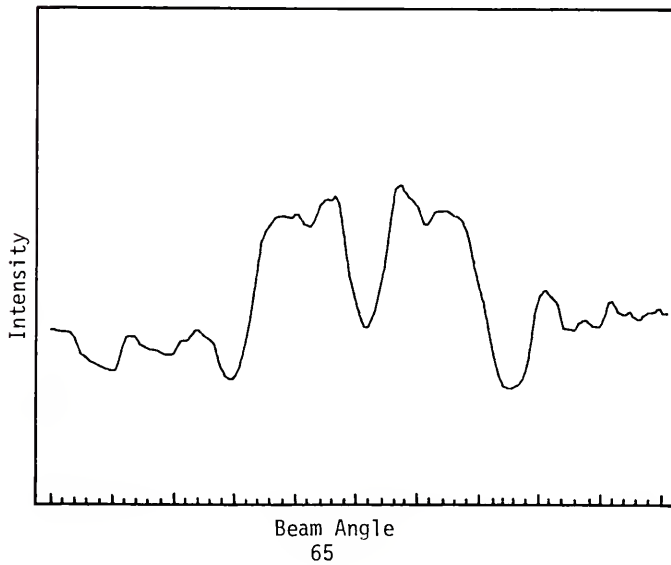
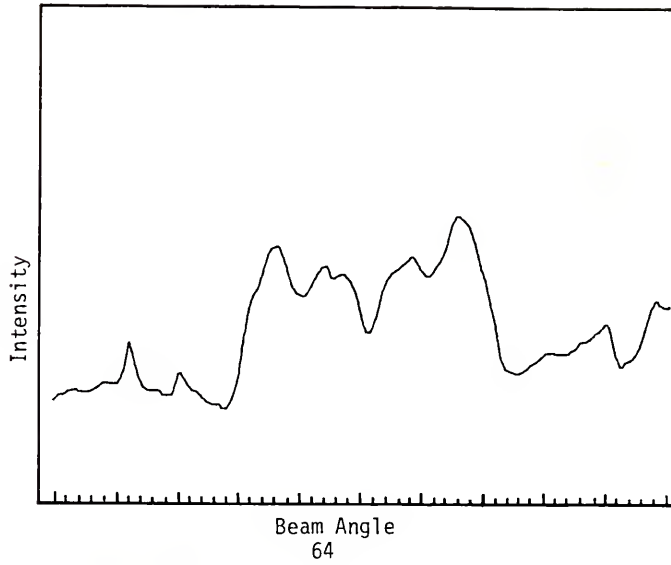


Figure 5.13 Intensity profiles from Figure 5.11, Area I.

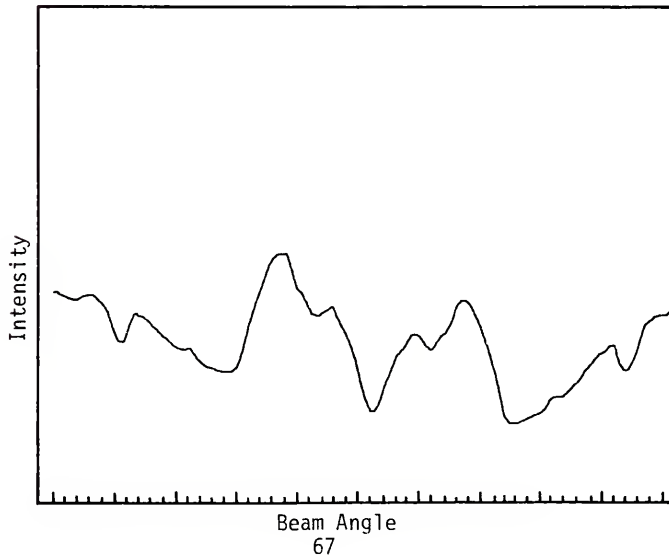
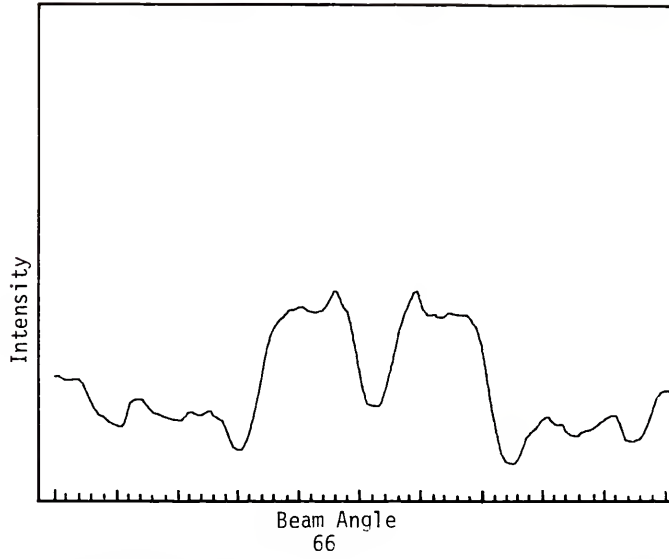


Figure 5.14 Intensity profiles from Figure 5.11(b), Area I.

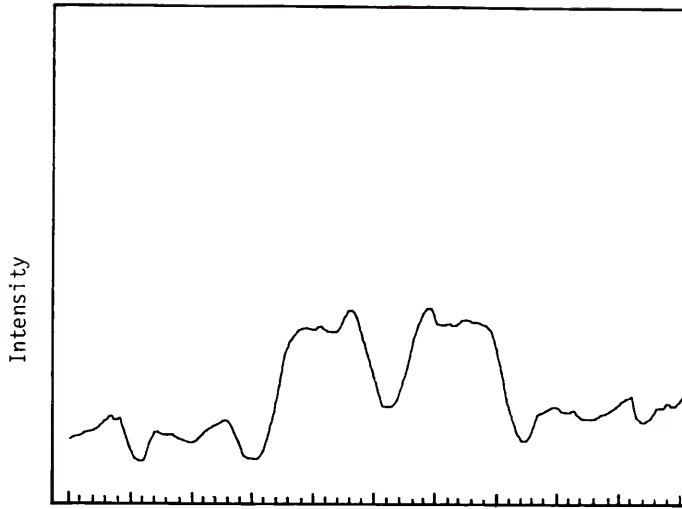
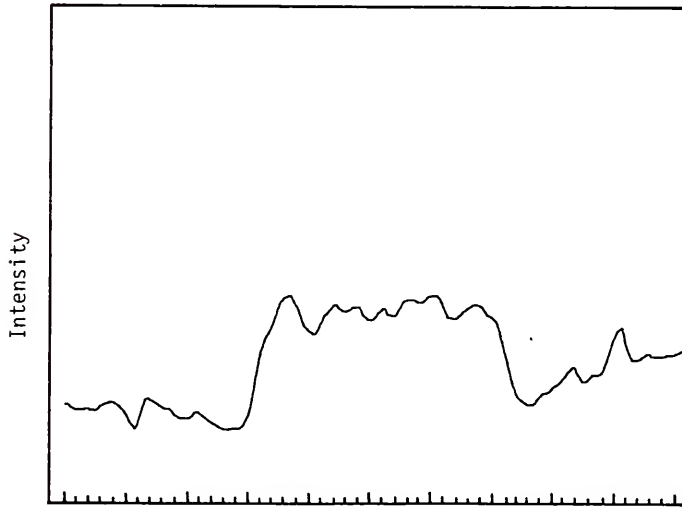
Beam Angle
68Beam Angle
69

Figure 5.15 Intensity profiles from Figure 5.12, Area I.

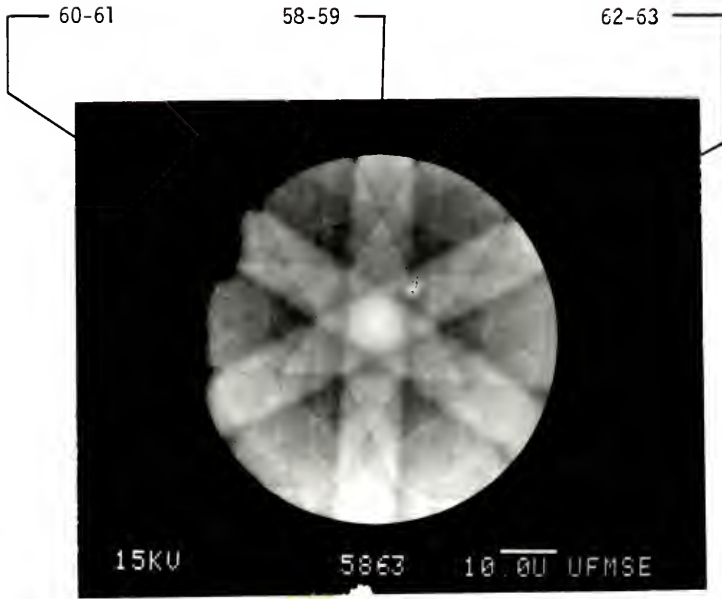
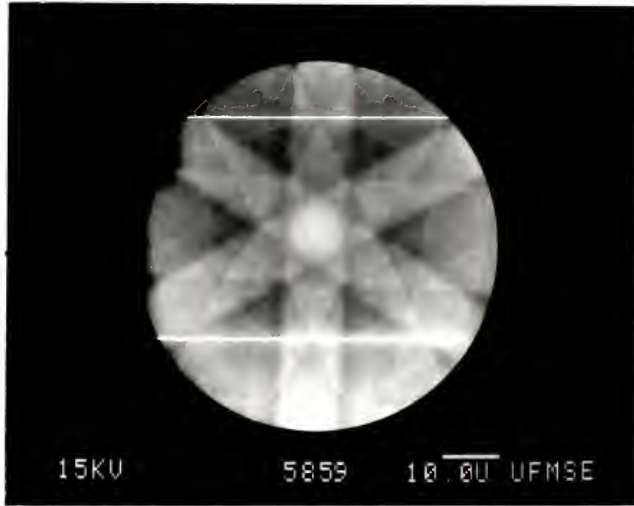
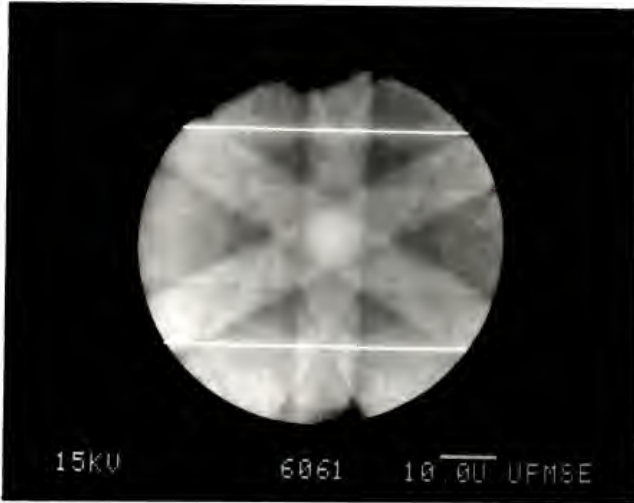


Figure 5.16 Unrotated ECP for scans 58-63, Area II.



(a)



(b)

Figure 5.17 Rotated ECP for scans 58-59 (a) and 60-61 (b).

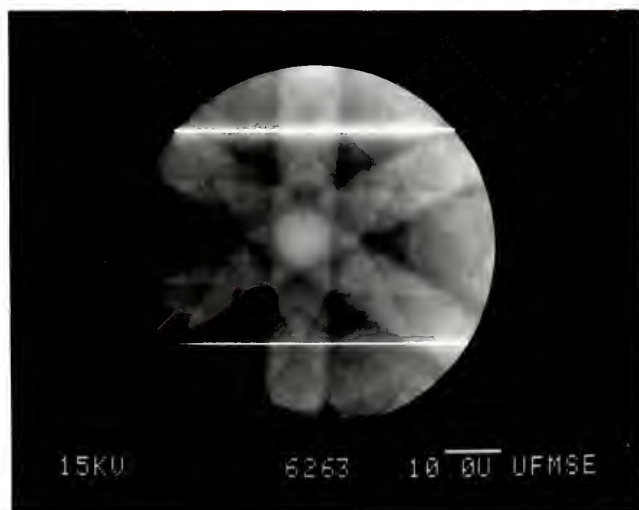


Figure 5.18 Rotated ECP for scans 62-63.

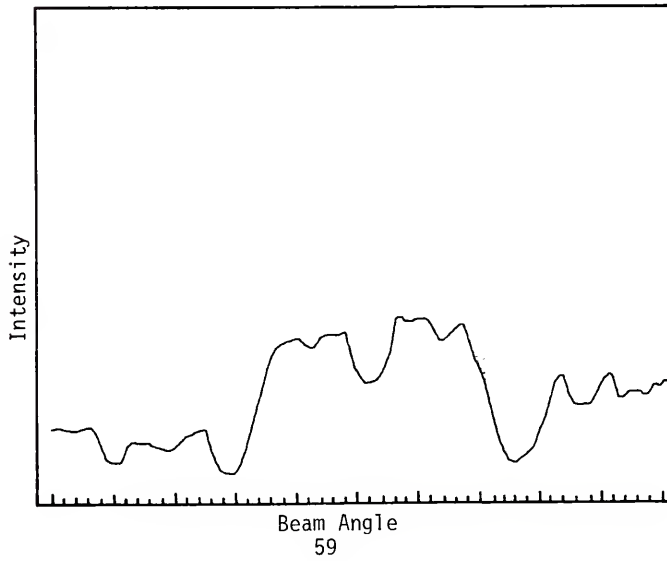
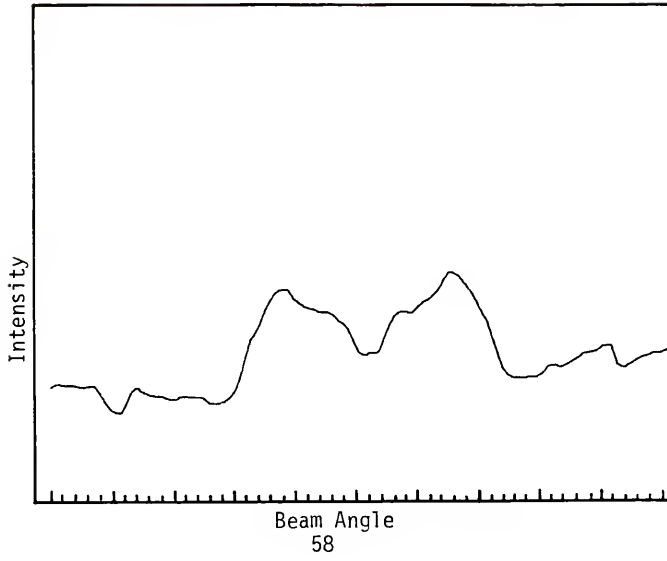
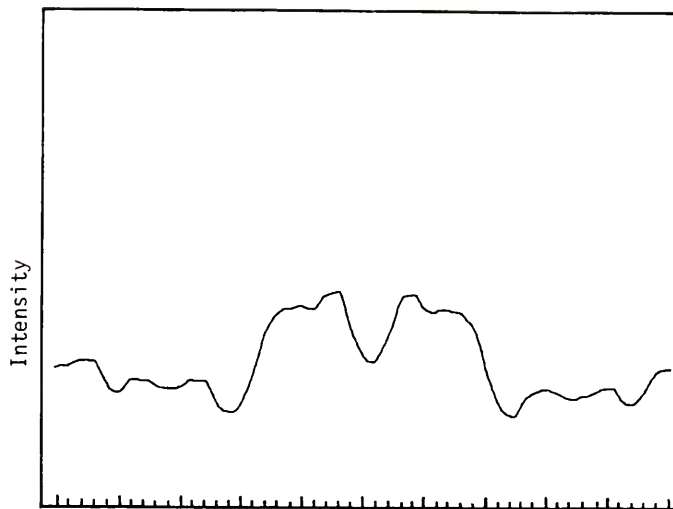
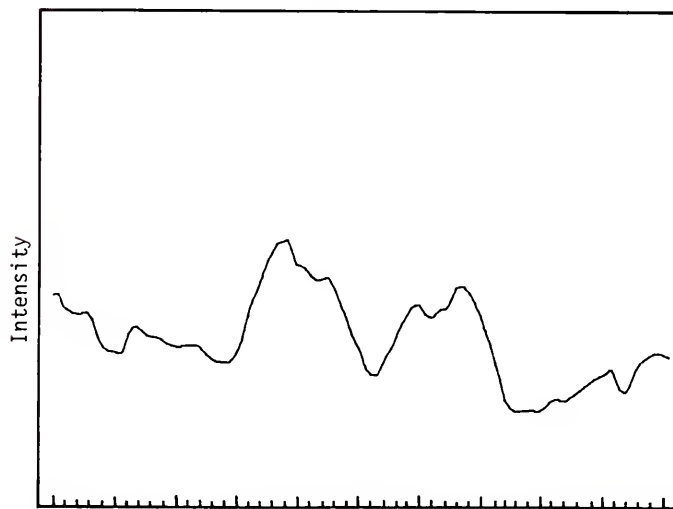


Figure 5.19 Intensity profiles for Figure 5.17(a), Area II.



Beam Angle
60



Beam Angle
61

Figure 5.20 Intensity profiles from Figure 17(b), Area II.

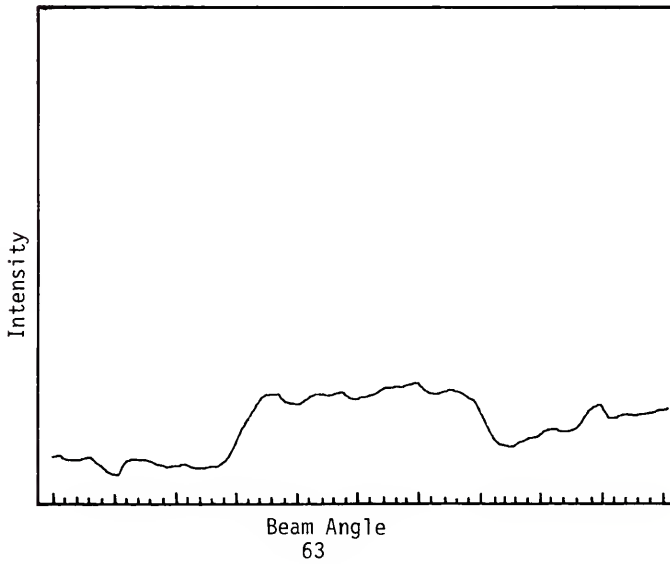
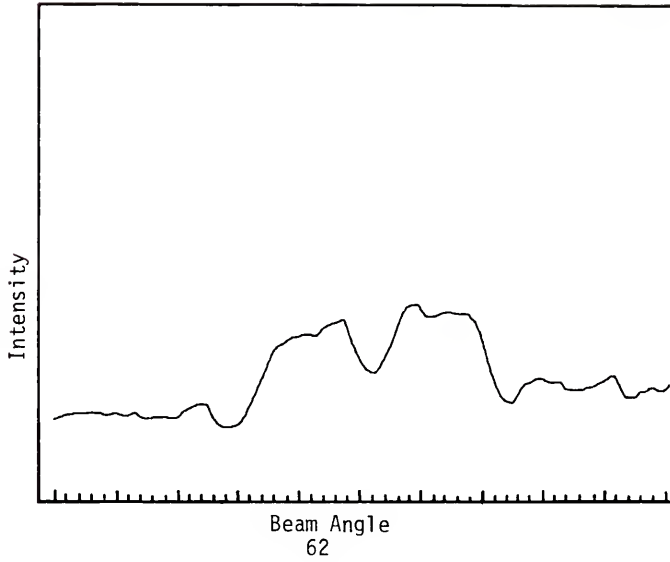


Figure 5.21 Intensity profile from Figure 5.18, Area II.

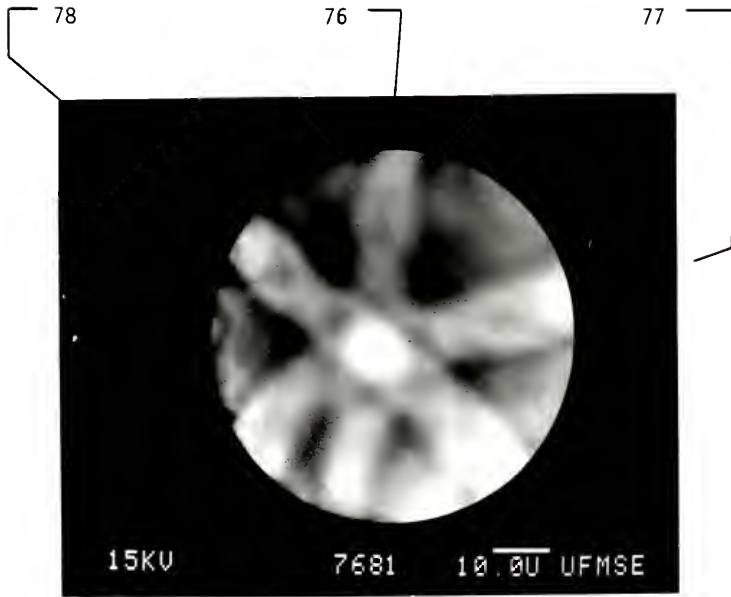


Figure 5.22 Unrotated ECPs for scans 76-78.

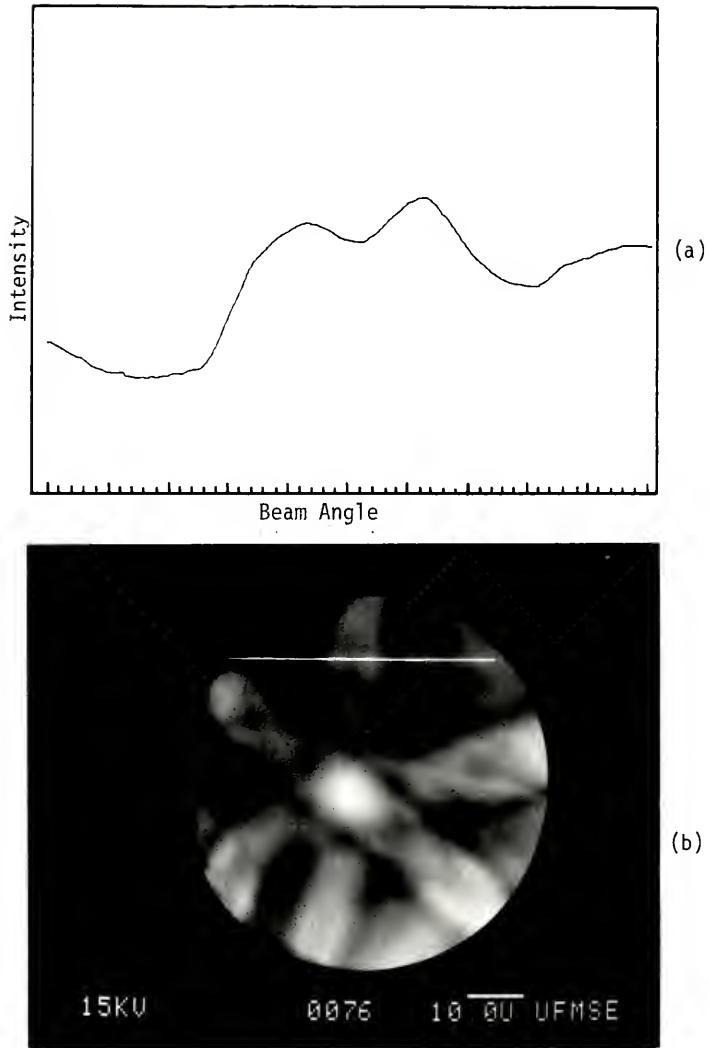


Figure 5.23 (a) Intensity profile and (b) rotated ECP for scan 76, Area III.

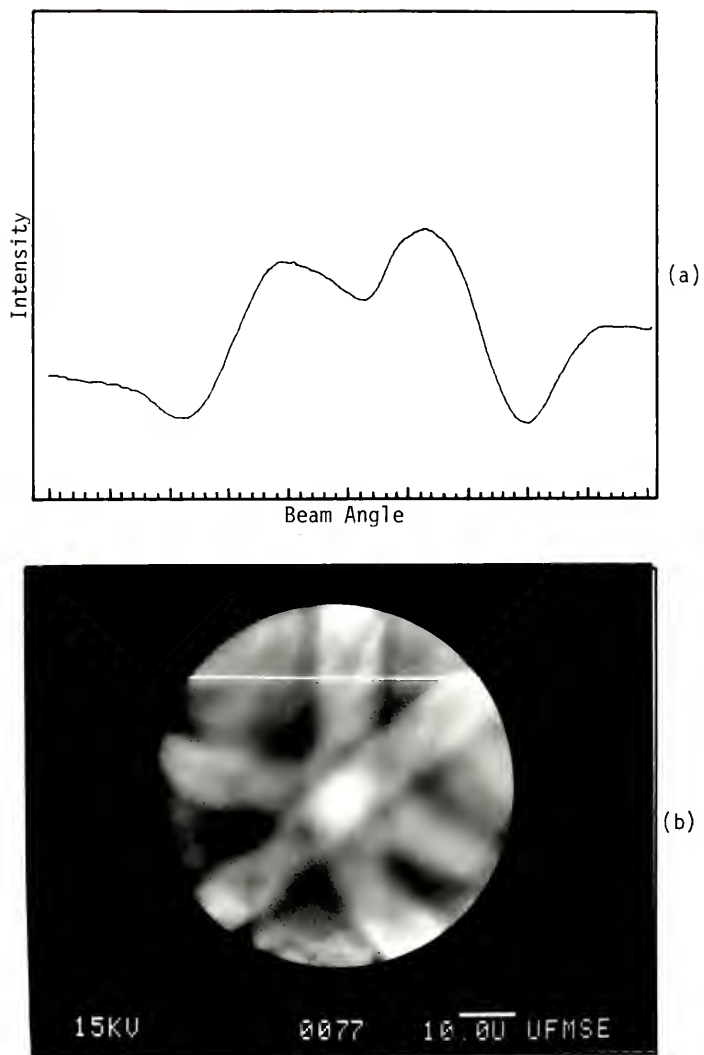


Figure 5.24 (a) Intensity profile and (b) rotated ECP for scan 77, Area III.

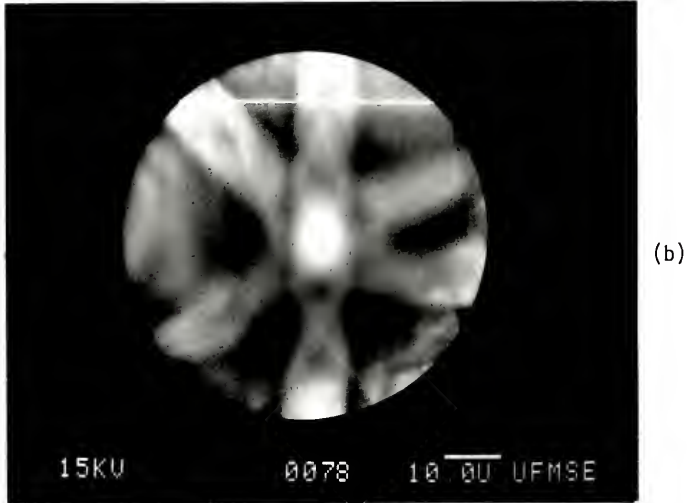
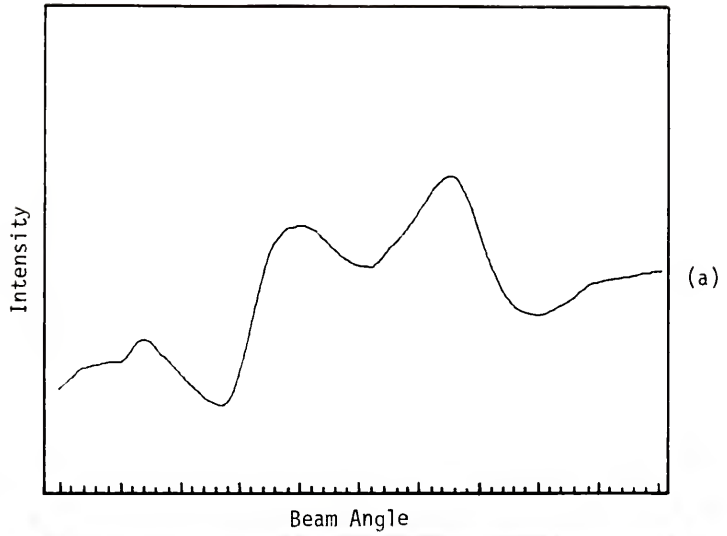


Figure 5.25 (a) Intensity profile and (b) rotated ECP for scan 78, Area III.

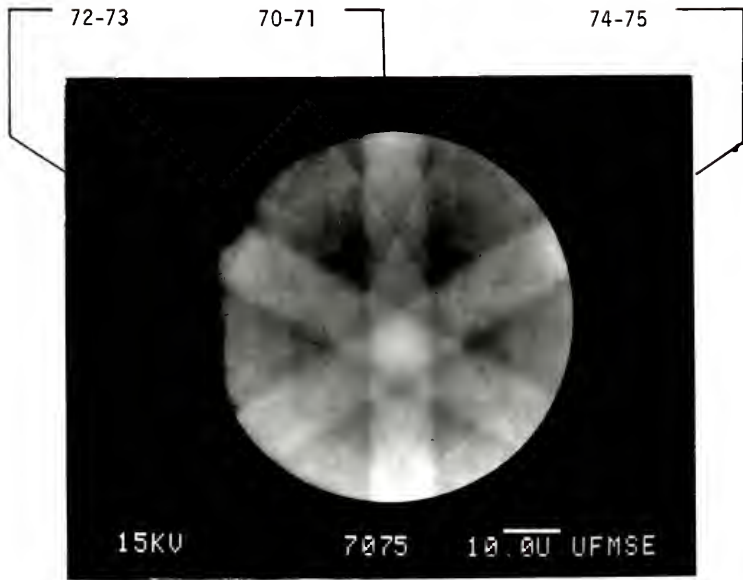
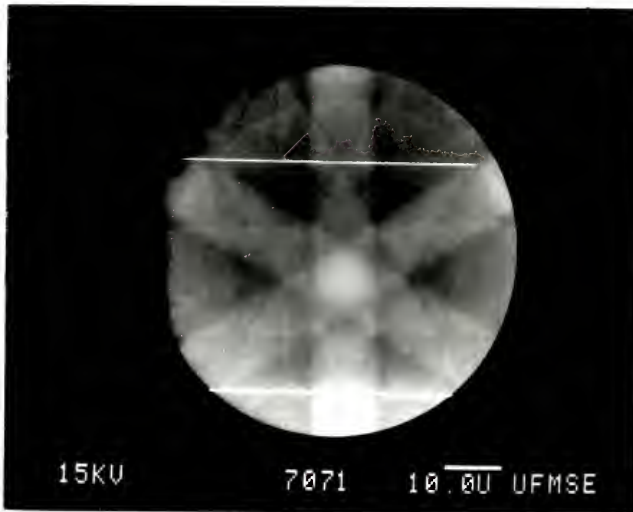
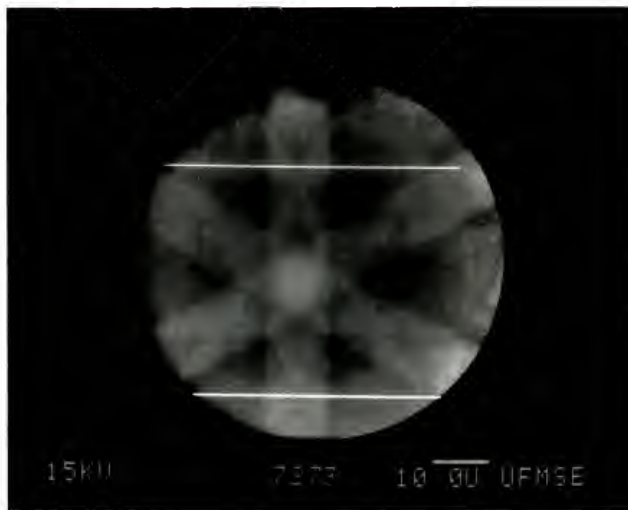


Figure 5.26 Unrotated ECP for scans 70-75, Area IIR.



(a)



(b)

Figure 5.27 Rotated ECP for scans 70-71 (a), 72-73 (b).

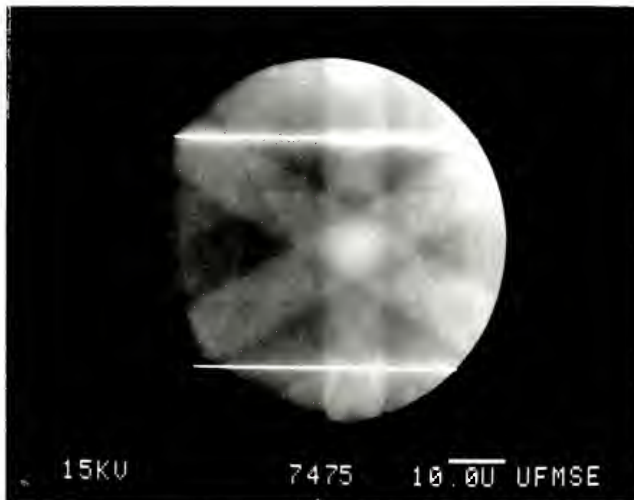


Figure 5.28 Rotated ECP for scans 74-75.

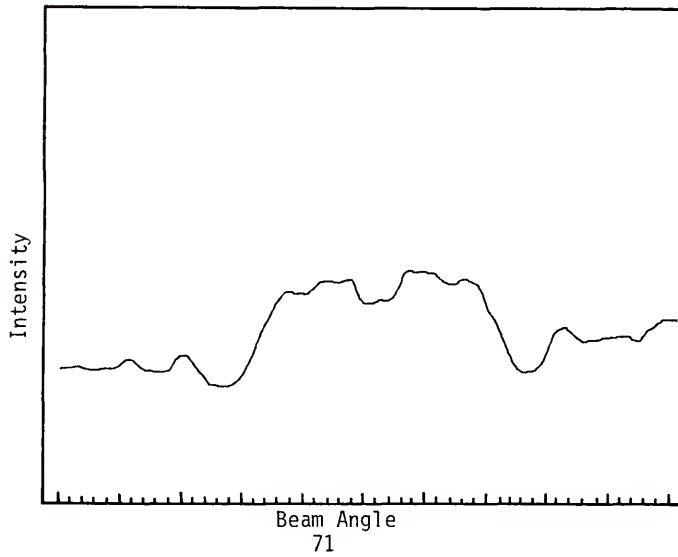
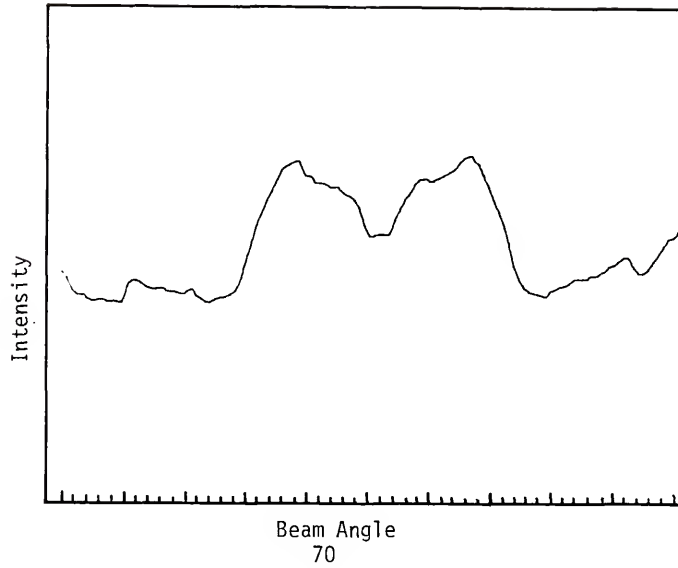


Figure 5.29 Intensity profiles for Figure 5.27(a), Area IIR.

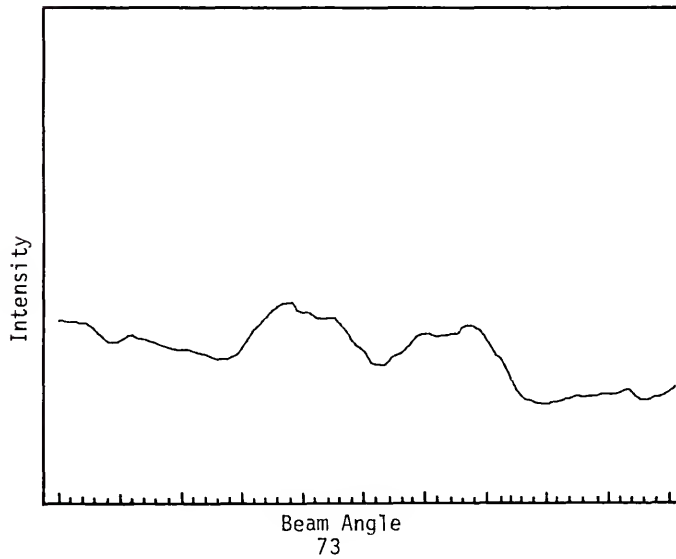
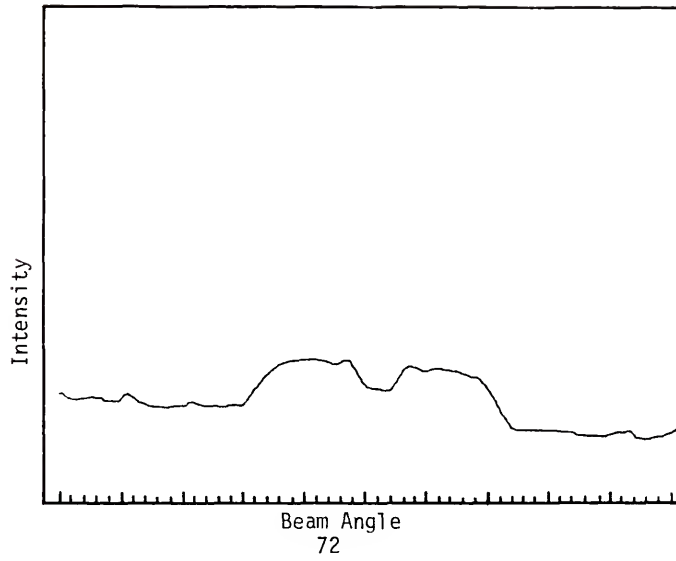


Figure 5.30 Intensity profiles for Figure 5.27(b), Area IIR.

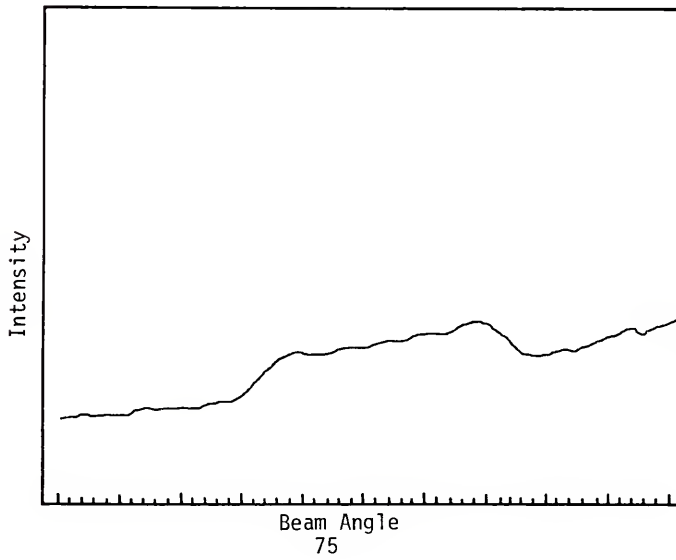
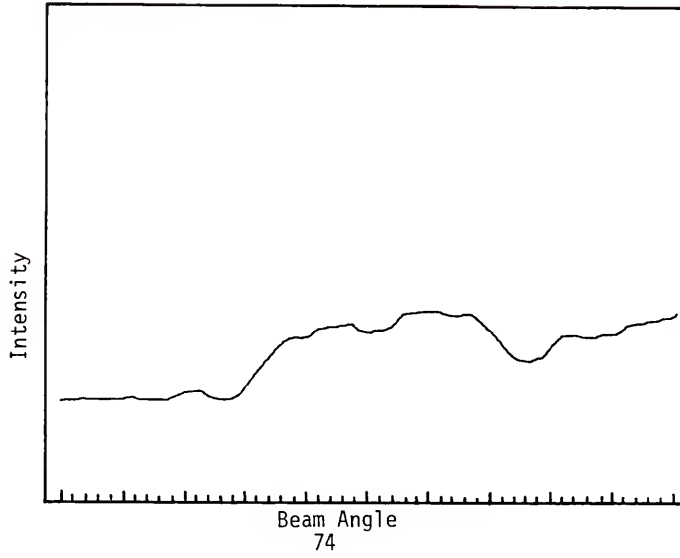


Figure 5.31 Intensity profiles for Figure 5.28, Area IIR.

TABLE 5.3
REARRANGEMENT OF INTENSITY PROFILE DATA

<u>Figure</u>	<u>Area</u>	<u>Intensity Scans</u>
5.32	I	64, 67, 69 (Type A)
5.33	I	65, 66, 68 (Type B)
5.34	II	58, 61, 63 (Type A)
5.35	II	59, 60, 62 (Type B)
5.36	IIR	70, 73, 75 (Type A)
5.37	IIR	71, 72, 74 (Type B)

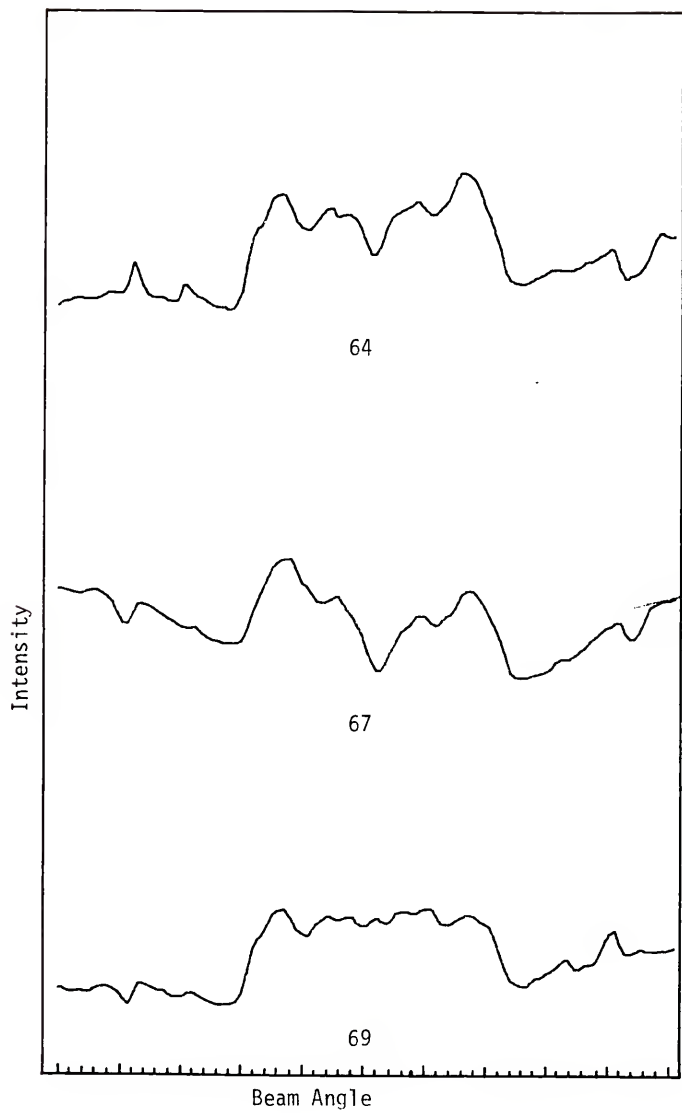


Figure 5.32 Type A intensity profiles from Area I.

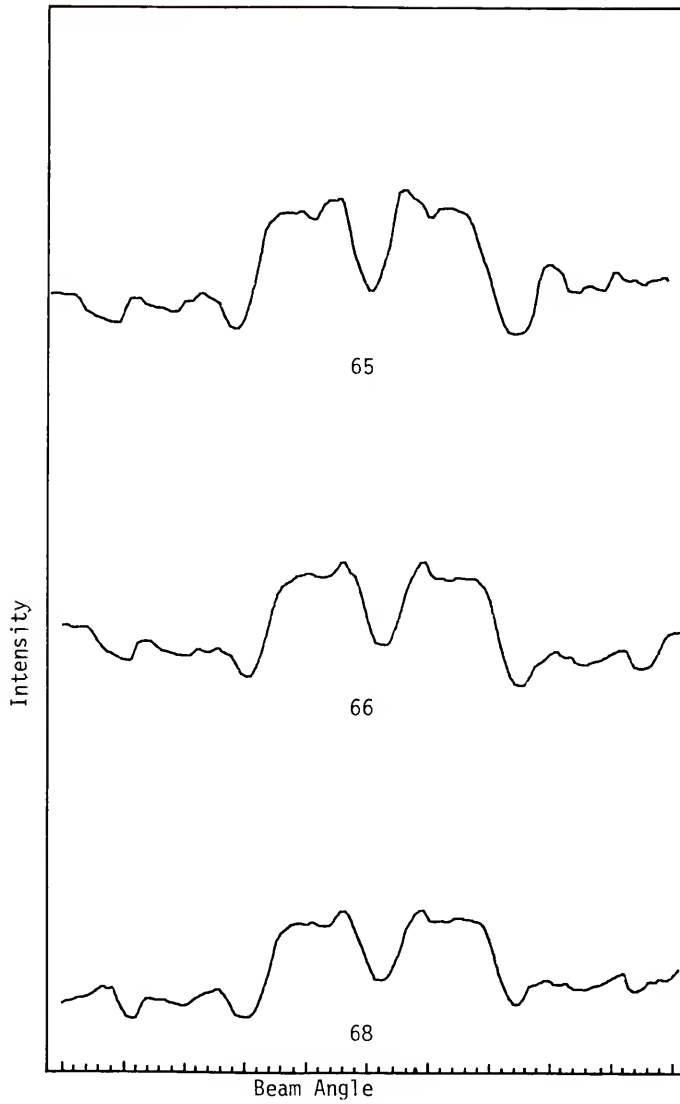


Figure 5.33 Type B intensity profiles from Area I.

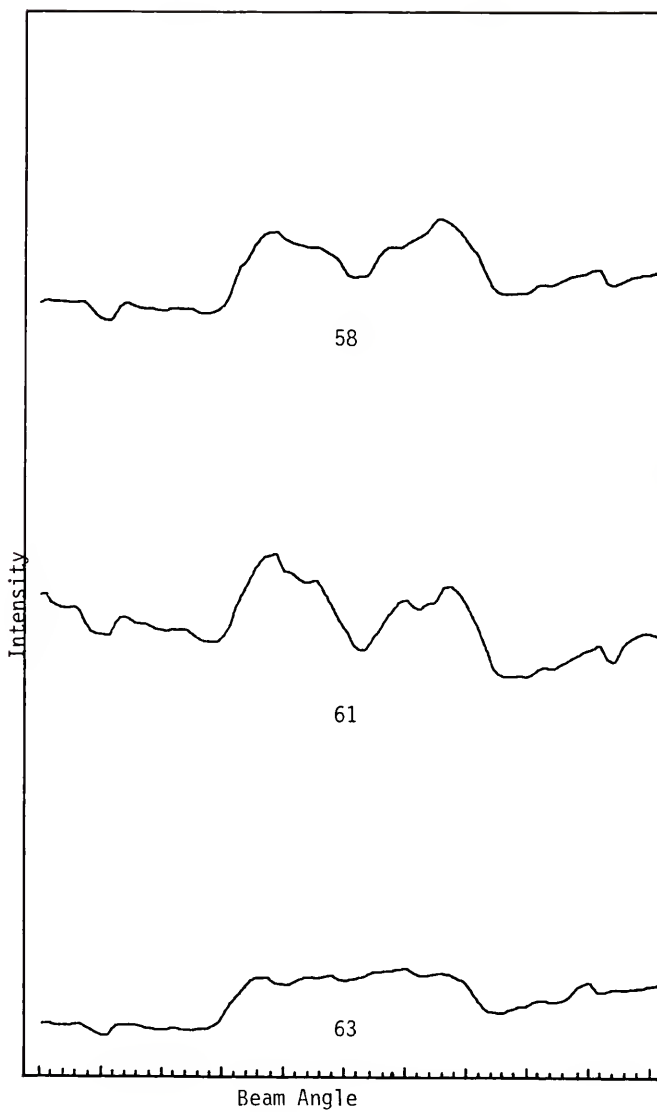


Figure 5.34 Type A intensity profiles from Area II.

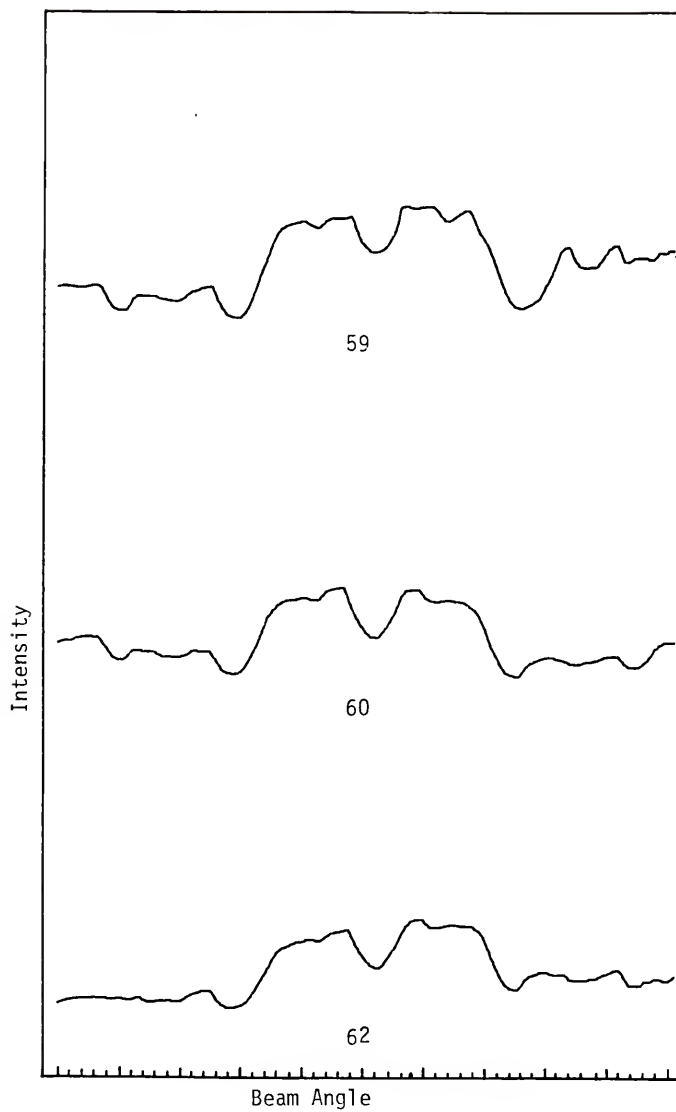


Figure 5.35 Type B intensity profiles from Area II.

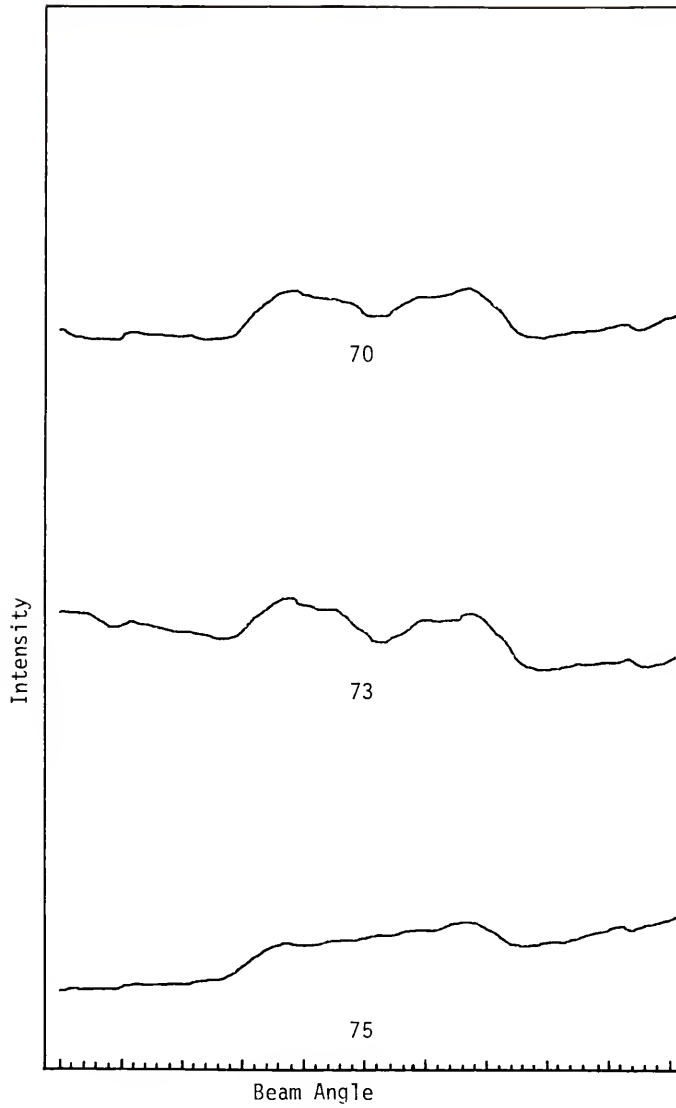


Figure 5.36 Type A intensity profiles from Area IIR.

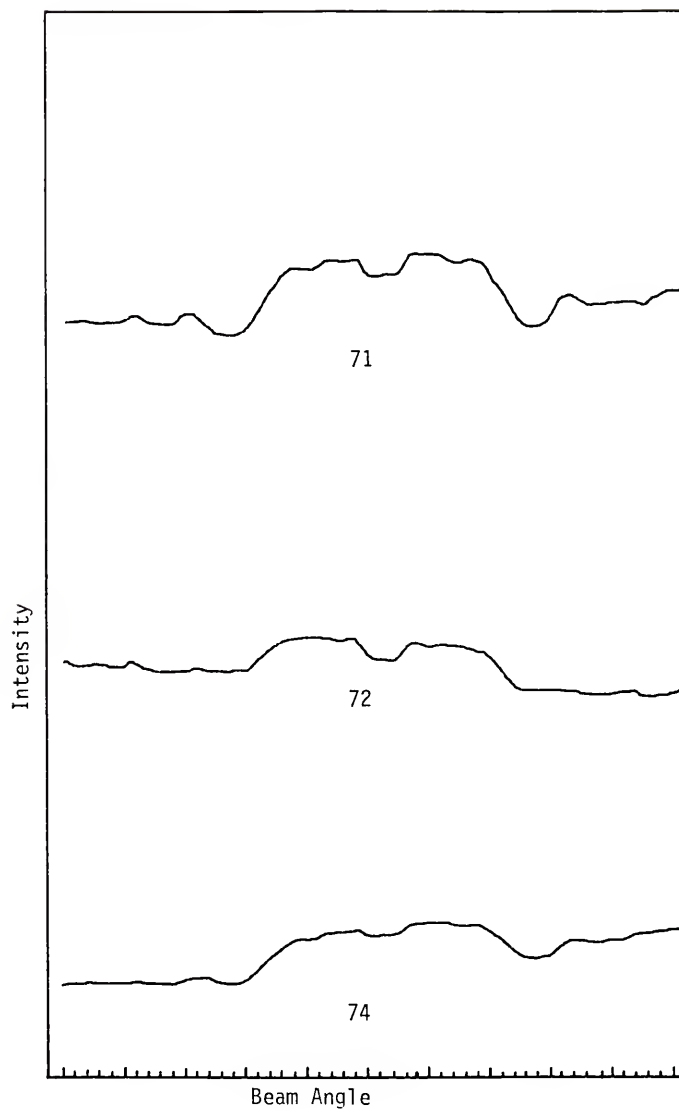


Figure 5.37 Type B intensity profiles from Area IIR.

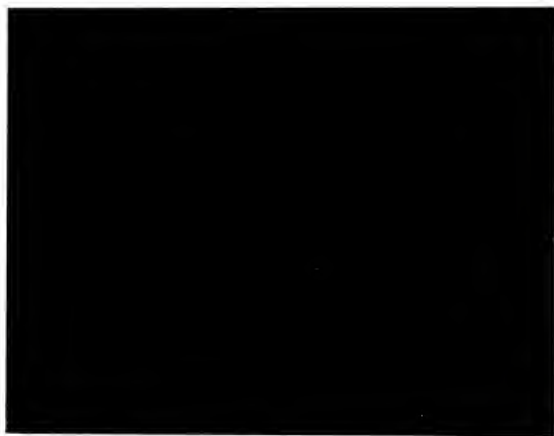


Figure 5.38 TEM micrograph and diffraction pattern from Area I.

Area III was highly bent, as shown from the curves in the bend contours in Figure 5.39. The bending is also apparent in the topographic SEM image in Figure 5.8(b). There are some dislocations present, although their magnitude cannot be assessed because the warped lattice produces a two-beam condition only over very narrow regions of the micrograph; dislocations outside the two-beam region would, in general, not be visible. No subgrain boundaries were visible.

Visibility of dislocations in a two-beam condition depends on which diffracting beam is used for imaging. If \vec{g} is the diffracting vector and \vec{b} the Burgers vector for a dislocation, the dislocation will be invisible (or at least nearly so) when $\vec{g} \cdot \vec{b} = 0$. Since \vec{b} is fixed for an individual dislocation, its value may be determined by changing \vec{g} (i.e., by tilting the sample) and observing whether the dislocation is visible or not.

If a field of dislocations all had the same Burgers vector, the entire field would disappear for an appropriate value of \vec{g} . This was the approach used to analyze area II. Once the area was located, the sample was tilted to a variety of two beam conditions and photographed. The analysis was complicated by the fact that the sample holder tilts eucentrically along only one axis, and tilt about the second axis is accompanied by a translation. This makes holding one area of the specimen under the beam difficult, and higher tilts change the edge profile and shorten distances enough to further complicate image interpretation.

In two separate investigations on area II no mass disappearance of dislocation images were observed. From this one may conclude that the dislocations are of mixed character. A typical image and diffraction pattern are shown in Figure 5.40. Even though the Burgers vector was not determined,



Figure 5.39 TEM micrograph from Area III.



Figure 5.40 TEM micrograph and diffraction pattern from Area II.

several things can be learned about the dislocations from these micrographs. The line directions have a definite orientation. The direction of this orientation may be determined by use of a rotation calibration between the image and diffraction pattern. Such a calibration is necessary because the lenses in the TEM have different currents in the image and diffraction modes, and thus each lens rotates the image a different amount. This calibration is performed with an orthorhombic crystal, MoO_3 , as described by Eddington (1975).

Figure 5.41 shows the image and diffraction pattern of the edge of the sample in the vicinity of areas II and IIR. The profile of the edge in Figure 5.41. may be seen in the upper left corner in Figures 5.8(a) and 5.9. The diffraction pattern in Figure 5.41 has been rotated the calibrated amount to correspond with the image. The sample was only translated, not rotated, between Figures 5.40 and 5.41. Thus, crystallographic directions are consistent in both micrographs.

In the TEM no evidence of specimen contamination was observed from the channeling previously performed in the SEM. Additional examination in the SEM in the topographic mode using backscattered and secondary electrons from imaging also revealed no contamination.

5.1.3 Discussion

Comparison of the six intensity profiles from the low dislocation area (area I), shown in Figure 5.32 and 5.33, reveals great similarity, as one would expect from an undistorted lattice. The type A planes have the {331} planes intersecting the {422} planes very near where the intensity profiles were being determined, as shown in Figure 5.1. The scan

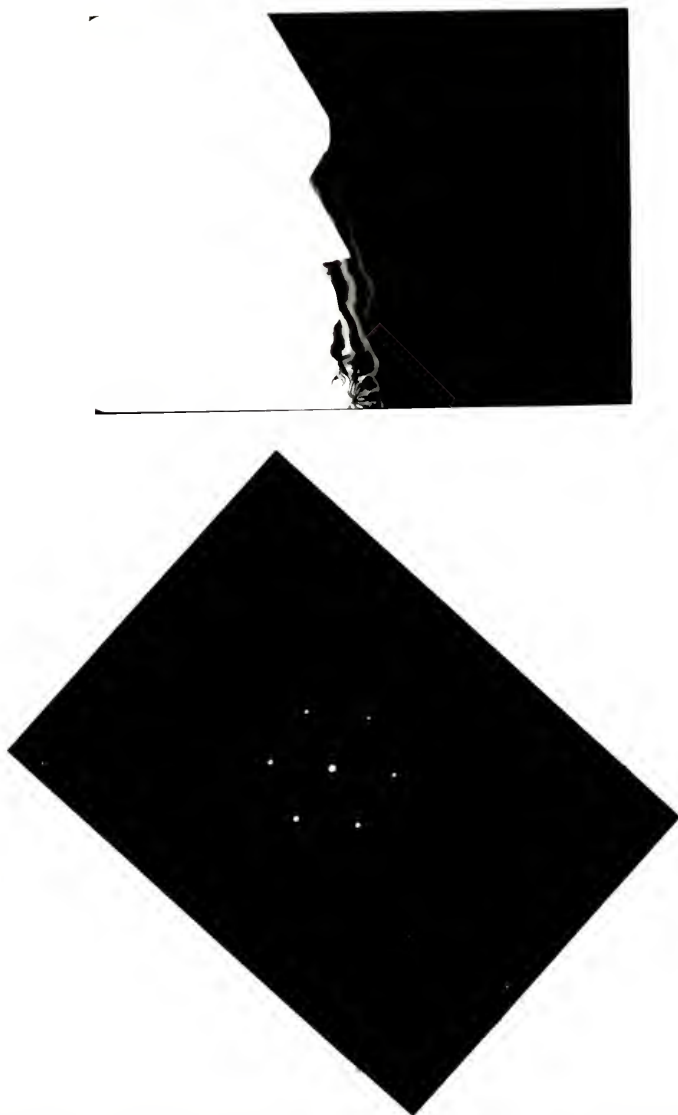


Figure 5.41 TEM micrograph and diffraction pattern for sample edge near area II. Diffraction pattern has been rotated to correspond to the image.

line was selected visually and small errors in placement alter the intersection with the $\{331\}$ lines enough that the intensity profile near the center of the $\{220\}$ peaks varies substantially. This is the difference between scans 64, 67 and 69. Type B planes, with the $\{331\}$ intersection, located further from the scan line used for the intensity profile, are not as sensitive to line position and show greater uniformity.

Looking now are areas II and IIR, the channeling patterns, Figures 5.16 and 5.26, the topographic SEM images, Figures 5.8(a) and 5.9, the TEM micrograph of the edge, Figure 5.41, and the TEM micrograph of the dislocations, Figure 5.40, may be compared to determine the line direction of the dislocations in relation to the channeling patterns. This is accomplished by using the profile of the edge as a reference point and remembering that: 1) the channeling patterns must be rotated 180° to correspond to the SEM topographic images, as explained in Chapter 2, and 2) the spots on the diffraction pattern correspond to points in reciprocal space in the zero order Laue zone, and the planes from which the spots originate are perpendicular to a line connecting the spots with the origin, i.e., the transmitted beam. The results of this analysis are shown in Figure 5.42.

Dislocations in silicon are mixed edge and screw, with the line direction and Burgers vector along the $\langle 110 \rangle$ directions 60° apart (Morin et al., 1979). Assuming the specimen has a (111) plane normal and the line direction to be $(01\bar{1})$, the Burgers vector may lie along the $[\bar{1}01]$ or $[1\bar{1}0]$ directions, as shown in Figure 5.43.

The Burgers vector of these dislocations can be broken down into two components, one edge with the Burgers vector perpendicular to the

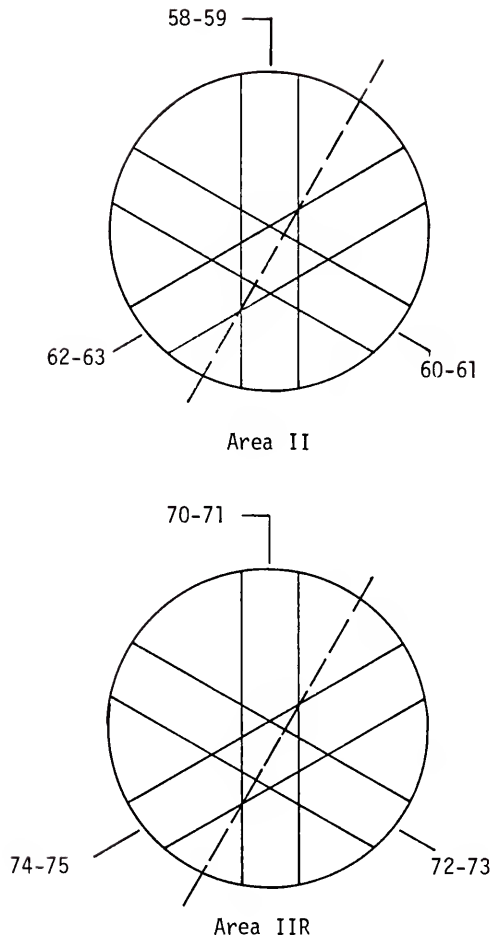


Figure 5.42 Analysis of line direction of TEMs on channeling patterns from area II and IIR. Line directions are dotted.

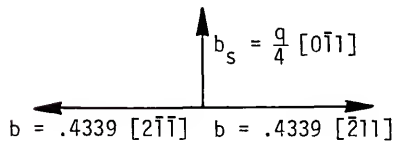
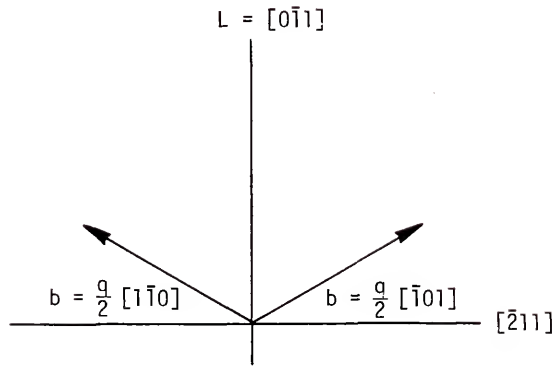


Figure 5.43 Dislocation analysis for Area II and IIR. L = line direction of dislocation.

line direction and the other screw with the Burgers vectors parallel to the line direction.

The peak broadening and loss of contrast in intensity profiles is the result of lattice distortions which cause changes in the Bragg angle. Looking at the Bragg equation

$$\lambda = 2d \sin \theta_B$$

Changes in the Bragg angle can occur from tensile or compressive strain induced changes in plane spacing (d) or from shear strain induced changes in the relative angles of planes that are initially perpendicular or nearly perpendicular to the beam. Shear strains serve to shift the value of θ_B locally without changing plane spacing.

Strain fields for both edge and screw dislocations are well known (e.g., Weertman and Weertman, 1964). Screw dislocations produce shear strain but no tensile strains on planes parallel to or orthogonal to the dislocation line. Edge dislocations produce a state of plane strain in planes orthogonal to the dislocation line.

For the dislocations of interest, i.e., in the (111) plane with a $[0\bar{1}1]$ line direction, and assuming a coordinate system of

$$X = [\bar{2}11]$$

$$Y = [111]$$

$$Z = [0\bar{1}1]$$

the only parameters that will displace θ_B are $\partial u/\partial y$ and $\partial w/\partial y$. These are angular displacements, and may be calculated from the equations of Weertman and Weertman (1964). The only strains affecting d-spacing will be ϵ_{xx} and ϵ_{zz} ; d changes in the y direction will be detected.

The equations for the displacements for a screw dislocation are:

$$\begin{aligned}u &= 0 \\v &= 0 \\w &= \frac{-b}{2\pi} \tan^{-1} \frac{y}{x}\end{aligned}$$

for an edge dislocation:

$$\begin{aligned}u &= \frac{-b}{2\pi} \left[\tan^{-1} \frac{y}{x} + \frac{\lambda+\mu}{\lambda+2\mu} \frac{xy}{x^2+y^2} \right] \\v &= \frac{-b}{2\pi} \left[-\frac{\mu}{2(\lambda+2\mu)} \log \frac{x^2+y^2}{C} + \frac{\lambda+\mu}{\lambda+2\mu} \frac{y^2}{x^2+y^2} \right] \\w &= 0\end{aligned}$$

where u,v,w = displacements in the x, y and z directions

C = arbitrary constant

μ, λ = Lamé constants.

From these displacements, parameters affecting d and θ_B can be calculated. They are summarized in Table 5.4.

Quantitative results are difficult to obtain, because the level of strain required to produce changes to the channeling pattern is unknown. Quantitative studies by others have proved only partially successful (Davidson and Booker, 1971). Some generalizations are possible, however. Referring to Figures 5.42 and 5.43, the screw component of the dislocations will be greatest on the (022) plane, profiles 60 and 64 for area II

TABLE 5.4
 SUMMARY OF PARAMETERS AFFECTING θ_B DUE TO DISLOCATIONS

Parameter Affecting Line on ECP	Dislocation Type	
	Edge	Screw
$\frac{\partial}{\alpha} \frac{2u}{2x} = \epsilon_{xx}$	finite	0
$\frac{\alpha}{\partial} \frac{2w}{2z} = \epsilon_{zz}$	0	0
$\frac{\alpha}{\partial} \frac{2u}{2y}$	finite	0
$\frac{\alpha}{\partial} \frac{2w}{2y}$	0	finite

and profiles 72 and 73 from area IIR. The effects of the edge dislocation will be seen equally on the remaining $\{220\}$ planes, the $(\bar{2}02)$ and $(2\bar{2}0)$. They would be maximum on the $(\bar{4}22)$ plane and should be zero on the $(0\bar{2}2)$ plane. (Perpendicular and parallel to the line direction, respectively.)

Looking at the intensity profiles from Figures 5.34 and 5.35 in the type A planes, scan 61 shows more contrast than 58 or 63. In the type B planes, there was less difference. In both cases, lines 62 and 63 had the least contrast. This would suggest other dislocations with different Burgers vectors were present as well.

The intensity profiles from area IIR all had lower intensity than the profiles from area II. This is due to increased numbers of dislocations, since if it were a contamination build-up it would have been greatest at the exact superposition of the channeled area. This further confirms the earlier observation that contamination build-up is not causing contrast loss.

The relative intensities of scans from area IIR are the same as area II. Scan 73 has higher contrast than scan 70 or 75 in the type A scans. Scans 71, 72 and 74 do not show the same differences; scans 74 and 75 had the least contrast.

In both areas II and IIR, the type A planes showed more sensitivity to strain, i.e., more loss in contrast than type B scans. This is possibly due to the presence of two more lines (the $\{331\}$ planes) in the vicinity of the scans, whose loss of contrast would increase the total loss of contrast in the intensity profile.

In examining the channeling patterns from areas II and IIR, it is obvious that the beam has wandered slightly across the sample surface while the pattern was recorded, i.e., the dynamic correction was not perfect. This imperfection is also noticeable as dark areas around the edges where the beam has moved to an area of the sample thin enough that the maximum intensity is less than the D.C. value subtracted from the signal before amplification. Dark areas do not indicate that the beam has wandered off the edge of the hole, which is located some distance away. Thus, some of the variation in contrast in the intensity profiles may be due to a slightly different area of the sample being channeled while each of the intensity profiles was being gathered. Such movement has been proposed by Spencer et al. (1974). Any movement of the beam was undoubtedly enhanced by the electronic scan rotation necessary to record intensity profiles. Activation of the scan rotation system while a grid was being used for dynamic correction, as described in Chapter 2, showed an adverse effect on the dynamic correction.

Unfortunately, the path followed by the dynamically corrected beam is not easily determined. Studies by Booker and Stickler (1972) and Joy and Baker (1973) were for lenses without dynamic correction.

The depth from which channeling contrast arises is approximately 1000 Å at 25-35 kV. At 15 kV it is undoubtedly less, and is also substantially less than the sample thickness. Although the TEM micrographs reveal the dislocations, it is not possible in a cursory analysis to determine which end of the dislocation line is on the top surface, and thus affects channeling patterns, and to determine which are on the bottom surface. In dislocations that are nearly parallel to the foil

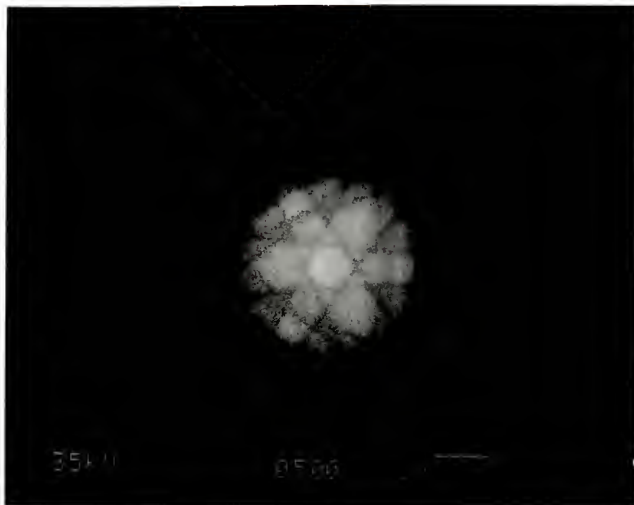
surface, any fraction of the dislocation may be near the upper surface. It is conceivable that any area that has a high dislocation concentration may produce minimal effects on the electron channeling pattern if the dislocations were near the bottom surface of the foil.

Area III contains a highly bent foil with a large amount of elastic strain in the lattice. This was apparently a result of a non-equilibrium resulting from removal of dislocations of predominantly one sign during the thinning process. The cracks visible in Figure 5.8(b) did not appear until several days after the sample was thinned, which is why it does not appear in Figure 5.7(a). The bending of planes in the channeling pattern corresponds to large amounts of elastic strain with relatively few dislocations, as evidenced by the bent Kikuchi lines in Figure 5.39. This is a second source of the line bending attributed to subgrain formation by Spencer et al. (1974) and Joy and Newberry (1971).

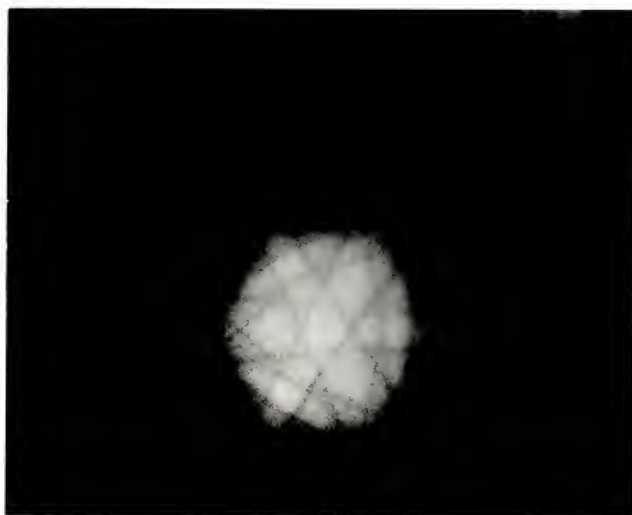
Although the intensity profiles are very broad, they have relatively high contrast compared with the profiles from areas II and IIR. This is because the lattice is less randomly distorted than in the case for large numbers of dislocations.

5.2 Elastically Strained Samples

Fine structure from the (111) pole at 35 kV for strain-free and 2% compressive strain are shown in Figure 5.44. Although these two patterns appear identical, differences exist that can be seen if they are superimposed, as shown in Figure 5.45 for three of the {735} lines. This compares with the theoretical calculation of Chapter 3.



(a)



(b)

Figure 5.44 Fine structure around the (111) pole at (a) 10% and (b) 2% compressive strain.

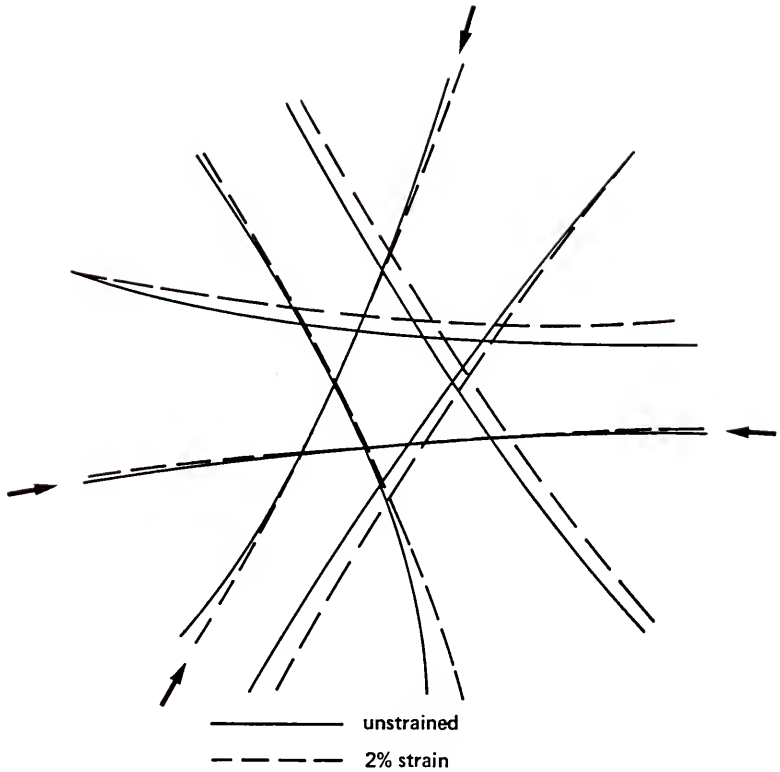


Figure 5.45 Superposition of enlargements of the fine structures from Figure 5.44. Arrows indicate lines arbitrarily made coincident. Movement of lines away from center indicates tensile strain.

The fact that the lines shift to points farther from the center indicates a tensile strain rather than compressive. This was due to bending by the sample upon application of the compressive displacement. The ratio of length to thickness on these samples was 39, well above the ratio required to eliminate bending (~ 10). This bending also made strain levels impossible to calculate.

Elastic strain is a long-range, uniform change in the the periodicity of the lattice, while plastic strain is characterized by the presence of dislocations, which cause short-range, non-uniform strains in the lattice. Here, long range means over the diameter of the channeled area, i.e., $\sim 10 \mu\text{m}$, while short range means producing measureable electron diffraction from lattice distortions, typically $\sim 200 \text{ \AA}$ (as measured in a TEM). Both kinds of strain could exist in the same sample. For example, a silicon sample plastically deformed at high temperature could be cooled and subjected to elastic strain. This elastic strain could be measured if the fine structure is still visible. Figure 5.46 shows the fine structure of a thick area of the sample used for plastic deformation studies, shown in Figure 5.7, containing an unknown concentration of dislocations. The fine structure is still visible, but at reduced contrast due to the more random lattice spacing caused by the dislocations. Obviously, there will be a point where the dislocations eliminate the fine structure, as reported by Schulson et al. (1969).

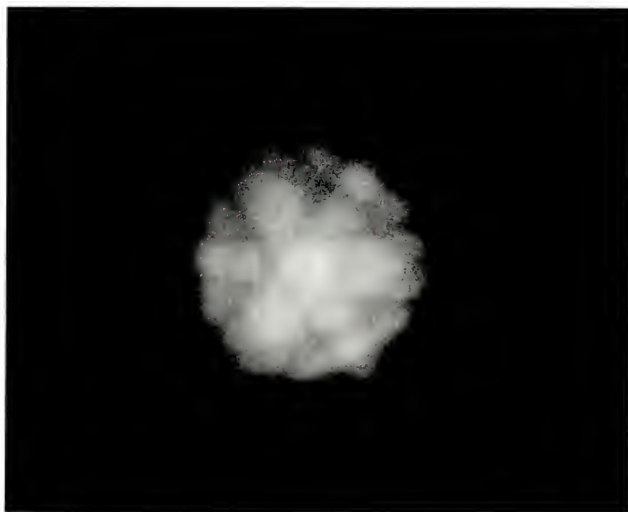


Figure 5.46 Fine structure near the (111) pole from silicon sample containing dislocations at 35 kV.

5.3 Summary

Areas of a thin, plastically deformed silicon specimen that produced visible changes to electron channeling patterns were identified, along with an area that had essentially the same channeling pattern as a dislocation-free silicon sample. Intensity profiles were obtained where possible, in the same location on both sides of the (111) pole for each of the three {220} planes. The areas were also examined by transmission electron microscopy for type and density of dislocations.

The control area had few dislocations. A second, highly bent area of the sample had relatively low dislocation density but these were apparently all of the same sign. The Kikuchi lines and the channeling pattern were very distorted due to lattice plane bending. A third area contained mixed dislocations with a common line direction. This area resulted in contrast loss in the ECP but no plane bending. The lack of bending was due to the mixed nature of the dislocations.

Plastic strain measurements in compression on a thin silicon sample resulted in shifting of the fine lines near the (111) pole, but the direction of the shift indicated a tensile load rather than compressive. This was due to sample bending. Measurement of the amount of elastic strain present by crosshead displacement was not possible.

CHAPTER 6
CONCLUSIONS AND RECOMMENDATIONS
FOR FURTHER STUDY

6.1 Conclusions

Initially, this research was undertaken to learn more of the details of the effect of plastic strain on electron channeling patterns, and specifically to see if the Burgers vector had an effect on intensity profiles from planes of the same type. Several other phenomena were discovered along the way relating to the origin of some of the fine lines on the electron channeling pattern, those near the pole centers, and the measurement of elastic strain.

A. In the understanding of the geometry of electron channeling patterns, the following points were learned:

- 1) Fine structure exists at the center of low index poles, e.g., the poles of the {100} and {111} planes. These lines appear only singly, as opposed to most other lines on an electron channeling pattern, which occur in pairs. The origin of these lines is the first order Laue zone in the reciprocal lattice-Ewald sphere construction used for electron and x-ray diffraction, with the additional criteria that lines appearing in the fine structure must have $|\alpha - \theta_B| < 1.5^\circ$ (depending on the energy of the electron beam) where α is the angle the plane makes with the pole and θ_B is the Bragg angle.

- 2) The circle centered on the (111) pole represents the intersection of the first order Laue zone and the Ewald sphere.
- 3) Other lines arise from the first order Laue zone that are located well away from the (111) pole, e.g., at 15 kV, the {331} lines appear. These lines can be distinguished from the lines arising from the zero order Laue zone by their symmetry. Reciprocal lattice points in the zero order zone have six-fold symmetry, while reciprocal lattice points in the first order zone are three-fold symmetric. Why some lines appear and others do not is unknown, but is surely related to the contrast forming mechanism. Lines that do appear can be indexed by using the Ewald sphere-reciprocal lattice construction.
- 4) Lines originating from the first order zone shift appreciably with changes in accelerating potential compared with the small changes in band widths which occur in lines originating from the zero order zone. For points lying near the pole centers, this is displayed as a shift in the lines forming the fine structure.

B. Elastic strain, i.e., long-range uniform changes in the lattice symmetry, also cause measureable changes in the fine structure around the pole centers. This was demonstrated experimentally for the (111) pole at 35 kV for tensile strain resulting from bending. The following points were demonstrated on the measurement of elastic strain:

- 1) Shifts in the fine structure can be predicted analytically by calculating shifts of the points in the reciprocal lattice, assuming values for Poisson's ratio are known.

- 2) The sensitivity of the shifts with beam energy is low, with a slight increase in line shifts being observed at lower beam energies. Lower beam energies also have the advantage that fewer lines appear in the fine structure, thus simplifying analysis.
- 3) Other lines in the electron channeling pattern that arise from the first order Laue zone that are located further from the pole centers should also shift with elastic strain. The magnitude of these shifts was calculated for the {331} planes at 15 kV but have not been experimentally measured as yet.
- 4) Fine structure can be detected in crystals containing dislocations. Thus, elastic strain can be measured in samples previously plastically strained, as long as the dislocation concentration is not high enough to eliminate the fine structure entirely.

C. For the measurement of plastic strain, i.e., the non-uniform short range changes in lattice periodicity caused by the presence of dislocations by the shape of intensity profiles, the following observations were made.

- 1) Intensity profiles must be made in the same location for comparisons; band width and contrast vary substantially with position along the band formed by a single plane.
- 2) In a channeling pattern from a (111) crystal at 15 kV, points from {220} bands equally distant but on opposite sides of the (111) pole can be shown not to be crystallographically equivalent. Intensity profiles on opposite sides of the (111) pole show different sensitivities to lattice strains arising from

dislocations, with half of the {220} band with the {331} planes intersecting further from the center, being slightly less sensitive than the half of the {220} band with the {331} planes intersecting nearer the center.

- 3) In a field of dislocations with a predominant, but not entirely uniform line direction, small differences in intensity profiles could be seen that might be related to the Burgers vector, assuming a mixed 60° dislocation in silicon.
- 4) Areas of a sample that have relatively low concentrations of dislocations, probably of the same sign, produce a severe lattice bending locally without subgrain formation, that is reflected by severely distorted bands in the channeling pattern. These distorted bands still have relatively high contrast.

When dislocations of the same sign occur over large areas within samples, lattice bending occurs, which in turn causes bending of bands in the channeling (and Kikuchi) patterns. This occurs at dislocation densities below the level at which strains from the dislocations would cause differences in contrast from the same type of planes in different orientations. Areas that show contrast loss in planes of the same type have mixed dislocations of the type that keep the sample flat but also tend to eliminate the directional nature of the strains. Thus, Burgers vector effects on channeling patterns will only be apparent when large areas of the surface of bulk samples have dislocations of the same sign where the remaining sample volume is great enough to keep the sample undistorted. Alternatively, if a smaller channeling beam were used, a smaller array of dislocations would be needed, and the strains tending to bend the lattice would be lower.

6.2 Recommendations for Further Study

Additional work on the effects of dislocations would be easier if GaAs or InAs were used as samples, since they also have a diamond cubic structure but a much higher backscattering coefficient due to their higher atomic weight. An interesting experiment would be to create an array of screw dislocations of the same sign, since their strain would affect channeling patterns in a single direction.

For determination of the effects of Burgers vector on channeling contrast, an interesting experiment would be a parallel array of screw dislocations, since they would not bend the foil and should produce strain that would affect the channeling patterns in only one direction.

The effects of elastic strain on electron channeling patterns could be investigated more thoroughly by use of in situ deformations such as four point bending, diametric compression and biaxial stresses. Slightly more complex geometries, such as a flat plate containing a hole loaded in tension or compression might prove interesting.

The phenomenon of fine lines away from the central pole need to be investigated further. The physics of the non-existence of some lines that are allowed by the structure factor, viz, the {351} lines for the (111) pole is unknown. The circle formed by the intersection of the Ewald sphere and the first order Laue zone appears in the (111) pole in silicon, but not on the (100) or (110) pole, although its existence for the (100) pole has been reported by Vicario et al. (1971).

Finally, the geometry of the fine structure near higher order poles needs to be determined. This would allow measurements of elastic strain

in a polycrystalline sample with randomly oriented grains, assuming that fine structure lines exist throughout the stereographic triangle.

REFERENCES

- Booker, G. R. (1971); Proc. 4th Ann. SEM Symp. (IIT Research Institute, Chicago), 465.
- Booker, G. R., Shaw, A. M. B., Whelan, M. J., and Hirsch, P. B. (1967); Phil Mag. 16, 1185.
- Booker, G. R. and Stickler, R. (1972); Proc. 5th Ann. SEM Symp. (IIT Research Institute, Chicago), 225.
- Brunner, M., Kohl, J. H. and Niedrig, H. (1978); Optik, 49, 477.
- Coates, D. G. (1967); Phil. Mag., 16, 1179.
- Coates, D. G. (1968); Phys. Stat. Sol., 27, K11.
- Coates, D. G. (1969); Proc. 2nd Ann. SEM Symp. (IIT Research Institute, Chicago), 27.
- Cullity, D. B. (1978); Elements of X-Ray Diffraction, 2nd Edition (Addison-Wesley, Reading, Mass.).
- Davidson, D. L. (1974); Scan. Elec. Micro./1974, Part IV (IIT Research Institute, Chicago), 927.
- Davidson, D. L. (1976); J. Phys. E.: Sci. Inst., 9, 341.
- Davidson, D. L. (1977); Scanning Electron Microscopy 1977/Vol. I (IIT Research Institute, Chicago), 431.
- Davidson, D. L. (1980); Scanning Elec. Micro./1980 (IIT Research Institute Chicago), in press.
- Davidson, S. M. and Booker, G. R. (1970); Proc. 7th Intl. Cong. on Elec. Micro. (Grenoble: IFSEM), 1, 235.
- Davidson, S. M. and Booker, G. R. (1971); Proc. 25th Ann. EMAG (London Institute of Physics) 298.
- Eddington, J. W. (1975); Practical Electron Microscopy in Materials Science, Vol. 2 (Philips, Eindhoven, Amsterdam).
- Farrow, R. C. and Joy, D. C. (1981); Scan. Elec. Micro./1981 (SEM, Inc., AMF O'Hare, Chicago), 135.
- Gregory, N. P., Richards, K. W. and Booker, G. R. (1977); Inst. Phys. Conf. Ser., 36, 315.

Hirsch, P. B., Howie, A., Nicholson, R. B., Pashley, D. W. and Whelan, M. J. (1977); Electron Microscopy of Thin Crystals (Kreiger Publishing Company, Hunnington, New York).

Hirsch, P. B., Howie, A. and Whelan, M. J. (1962); Phil. Mag., 7, 2095.

Hirsch, P. B. and Humphries, C. J. (1970a); Proc. 3rd. Ann. SEM Symp. (IIT Research Institute, Chicago), 449.

Hirsch, P. B. and Humphries, C. J. (1970b); Proc. 7th Intl. Cong. on Elec. Micro., (Grenoble, IFSEM), 1, 229.

Holt, D. B., Gavrilovic, J., and Jones, M. P. (1968); J. Mat. Sci., 3, 553.

Howie, A., Linington, P. F., and Tomlinson, P. N. (1971); Phil. Mag., 23, 1559.

JEOL (1971); Manual for JSM-35C Selected Area Diffraction Components, No. IEP35-SDC (JEOL, Letd., Tokyo, Japan).

Joy, D. C. (1974); Quantitative Scanning Electron Microscopy (Academic Press, London), 131.

Joy, D. C., Booker, G. R., Fearon, E. O. and Bevis, M. (1971); Proc. 4th Ann. SEM Symp. (IIT Research Institute, Chicago), 497.

Joy, D. C. and Booker, G. R. (1973); Proc. 6th Ann. SEM Symp. (IIT Research Institute, Chicago), 137.

Joy, D. C. and Maruszewski, C. M. (1975); J. Mat. Sci., 10, 178.

Joy, D. C. and Newberry, D. E. (1971); Proc. 4th Ann. SEM Symp. (IIT Research Institute, Chicago), 113.

Joy, D. C. and Newberry, D. E. (1972); J. Mat. Sci., 7, 714.

Joy, D. C., Newberry, D. E. and Hazzledine, P. M. (1972); Proc. 5th Ann. SEM Symp. (IIT Research Institute, Chicago), 97.

Lane, W. C., Pense, D. E. and Yew, N. C. (1974); Electron Channeling in the SEM (ETEC Corp. Applications Note, ETEC Corp., Hayward, California).

Morin, P. Pitival, M., Besnard, D. and Fontaine, G. (1979); Phil. Mag., A40, 511.

Morin, P. and Vicario E. (1976); J. Phys. E: Sci. Inst., 9, 345.

Newberry, D. E. and Yakowitz, H. (1975), Practical Scanning Electron Microscopy, J. Goldstein and H. Yakowitz, ed. (Plenum Press, New York), 149.

Payne, S. M. and Ralph, B. (1980); *Inst. Phys. Conf. Ser. No. 52*, 17.

Runyan, W. R. (1965); Silicon Semiconductor Technology (McGraw-Hill, New York), 221.

Russell, Phillip (1981); Personal communication.

Schulson, E. M. (1969); *J. Phys. E: Sci. Inst.*, 2, 361.

Schulson, E. M. (1971a); *Phys. Stat. Sol.(b)*, 46, 95.

Schulson, E. M. (1971b); Proc. 4th Ann. SEM Symp. (IIT Research Institute Chicago), 489.

Schulson, E. M. and Van Essen, C. G. (1969); *J. Phys. E: Sci. Inst.*, 2, 247.

Schulson, E. M., Van Essen, C. G. and Joy, D. C. (1969); Proc. 2nd Ann. SEM Symp. (IIT Research Institute, Chicago), 45.

Shaw, A. M. B., Booker, G. R. and Coates, D. G. (1969); *J. Sci. Inst.*, 2, 243.

Spencer, J. P., Booker, G. R., Humphries, G. J. and Joy, D. C. (1974); Scan. Elec. Micro./1974 (IIT Research Institute, Chicago), 919.

Spencer, J. P. and Humphries, C. J. (1980); *Phil. Mag.*, 42, 433.

Spencer, J. P., Humphries, C. J. and Hirsch, P. B. (1972); *Phil. Mag.* 26, 193.

Stickler, R. and Booker, G. R. (1972); Electron Microscopy and the Structure of Materials, G. Thomas, ed. (University of California Press, Berkeley, California), 301.

Stickler, R., Hughes, C. W. and Booker, G. R. (1971); Proc. 4th Ann. SEM Symp. (IIT Research Institute, Chicago), 473.

Van Essen, C. G. (1970); Proc. 7th Intl. Cong. on Electron Microscopy (Grenoble, IFSEM), 1, 237.

Van Essen, C. G. and Verhoeven, J. D. (1974); *J. Phys. E: Sci. Inst.*, 1, 768.

Van Essen, C. G., Schulson, E. M. and Donaghay, R. H. (1970); *Nature*, 225, 847.

Van Essen, C. G., Schulson, E. M. and Donaghay, R. H. (1971); *J. Mat. Sci.*, 6, 213.

Vicario, E. and Pitival, M. (1969); C. R. Acad. Sc. Paris, 269, 287.

Vicario, E., Pitival, M. and Fontaine, G. (1970a); C. R. Acad. Sc. Paris, 270, 1402.

Vicario, E., Pitival, M. and Fontaine, G. (1971); Acta. Cryst., A27, 1.

Vicario, E., Pitival, M. and Usan, R. (1970b); J. Phys. E: Sci. Inst., 3, 323.

Weertman, J. and Weertman, J. R. (1964); Elementary Dislocation Theory (Macmillan, New York), 32.

Wolf, E. D., Braunstein, M. and Braunstein, A. I. (1969); Appl. Phys. Let., 15, 389.

Zackowitz, W. and Pantell, R. H. (1981); J. Appl. Phys., 52, 2799.

BIOGRAPHICAL SKETCH

Michael Charles Madden was born March 1, 1946, in Mendota, Illinois. After moving to Florida he attended the University of Florida and received a Bachelor of Science in Engineering Sciences in 1968. Upon the elimination of graduate school draft deferments due to the Vietnam war, he worked briefly for Ford Motor Company, then for Pratt and Whitney Aircraft. When the war ended in 1972, he returned to the University of Florida and received a Master of Science in materials science under Dr. Larry Hench. From 1974 to 1979 he worked for the Program of Distinction in Biomedical Engineering at the University. In 1979 he returned to graduate school in materials science to pursue a Doctor of Philosophy degree.

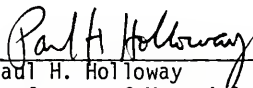
Michael Madden is currently employed by Sandia Laboratories in Albuquerque, New Mexico.

I certify that I have read this study and that in my opinion it conforms to acceptable standards of scholarly presentation and is fully adequate, in scope and quality, as a dissertation for the degree of Doctor of Philosophy.



John J. Hren, Chairman
Professor of Materials Science
and Engineering

I certify that I have read this study and that in my opinion it conforms to acceptable standards of scholarly presentation and is fully adequate, in scope and quality, as a dissertation for the degree of Doctor of Philosophy.



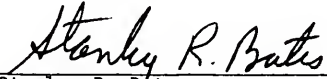
Paul H. Holloway
Professor of Materials Science
and Engineering

I certify that I have read this study and that in my opinion it conforms to acceptable standards of scholarly presentation and is fully adequate, in scope and quality, as a dissertation for the degree of Doctor of Philosophy.



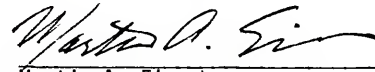
Robert W. Gould
Professor of Materials Science
and Engineering

I certify that I have read this study and that in my opinion it conforms to acceptable standards of scholarly presentation and is fully adequate, in scope and quality, as a dissertation for the degree of Doctor of Philosophy.



Stanley R. Bates
Associate Engineering of Materials
Science and Engineering

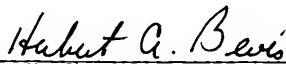
I certify that I have read this study and that in my opinion it conforms to acceptable standards of scholarly presentation and is fully adequate, in scope and quality, as a dissertation for the degree of Doctor of Philosophy.



Martin A. Eisenberg
Professor of Engineering Sciences.

This dissertation was submitted to the Graduate Faculty of the College of Engineering and to the Graduate Council, and was accepted as partial fulfillment of the requirements for the degree of Doctor of Philosophy.

May, 1982



Wayne H. Chen
Dean, College of Engineering

Francis G. Stehli
Dean of the Graduate School

